



Pattern formation
by the Min system of *Escherichia coli*

Dissertation
zur Erlangung des Grades
des Doktors der Naturwissenschaften
der Naturwissenschaftlich-Technischen Fakultät II
-Physik und Mechatronik-
der Universität des Saarlandes

von

Elisabeth Fischer-Friedrich

Saarbrücken
2008

Tag des Kolloquiums: 15.05.2009

Dekanin/Dekan: Prof. Christoph Becher

Mitglieder des
Prüfungsausschusses: Prof. Karin Jacobs, Prof. Karsten Kruse,
Dr. Björn Huke, Prof. Ludger Santen,

Abstract

Min proteins are a class of proteins that is widely conserved among bacteria. In the rod-shaped bacterium *Escherichia coli*, Min proteins form spatiotemporal patterns which are characterized by concentration maxima that oscillate from one cell pole to the other.

In this thesis, we use theoretical and experimental tools to characterize the Min system. We consider two mean field models of the Min system that emphasize different aspects of Min protein interactions inducing a dynamic instability. The first model assumes that MinD proteins feel mutual interactions in the membrane-bound state leading to an aggregating current that results in the formation of concentration maxima. In the second model, MinD and MinE bind to the membrane in a self-enhanced manner thereby generating a dynamic instability in the system. We study solutions of the dynamical systems and compare them with the patterns observed in living *E. coli* and *in vitro*. Both models are able to generate patterns similar to those observed in wild type *E. coli*. Oscillations in filamentous cells and the stochastic switching in very short cells are better described by the first model. *In vitro* patterning of the Min system is more aptly captured by the second description.

Using fluorescence correlation spectroscopy *in vivo*, we obtain characteristic time constants of the Min system. We experimentally study pattern formation of the Min system in short *E. coli* and find stochastic switching of Min proteins instead of oscillations.

Zusammenfassung

Min-Proteine sind ein Teil des bakteriellen Zytoskeletts. Im stäbchenförmigen Bakterium *Escherichia coli* bilden Min-Proteine raumzeitliche Muster.

In dieser Doktorarbeit benutzen wir sowohl theoretische als auch experimentelle Methoden, um das Min-System zu charakterisieren.

Im theoretischen Teil der Arbeit betrachten wir zwei verschiedene, grobkörnige Modelle des Min-Systems, die exemplarisch verschiedene Annahmen über die Erzeugung der dynamischen Instabilität machen. Das erste Modell geht davon aus, dass MinD-Proteine im membran-gebundenen Zustand miteinander wechselwirken, so dass ein aggregierender Strom entsteht, der zu einer Bildung von Konzentrationsmaxima führt. Das zweite Modell nimmt an, dass MinD und MinE selbstverstärkend an die Membran binden und so eine dynamische Instabilität im System erzeugen. Lösungen der zugehörigen dynamischen Systeme werden untersucht und mit den Mustern des Min-Systems in *E.coli* und *in vitro* verglichen.

Durch Anwenden von Fluoreszenz-Korrelations-Spektroskopie auf Min-Proteine *in vivo* konnten wir charakteristische Zeitskalen des Min-Systems bestimmen.

Zusätzlich zeigen wir experimentell, dass in sehr kurzen *E. coli* Min-Konzentrationsmaxima stochastisch zwischen den Zellpolen hin- und herwechseln.

Acknowledgments

First and foremost, I would like to thank Karsten Kruse for the biophysical expertise, the time and the kindness with which he supervised my work. He encouraged me to do both, theory and experimental studies, and assisted me in both fields with his broad knowledge and interest.

I am grateful to Frank Jülicher who accepted me into his group and gave me the opportunity to write my thesis in a stimulating and vivid environment. Especially, I would like to thank him that I could take part in his PhD student seminar.

I enjoyed very much the collaboration with Martin Loose working in the group of Prof. Schwille at the Biotec. His biochemical capabilities made it possible to test conjectures on the Min system directly in reality and his *in vitro* experiments once and for all showed that Min patterns can indeed be generated by self-organization. I am very glad that he was not scared by our physicists jargon.

The struggle for theoretical understanding of pattern formation in the Min system was shared by Giovanni Meacci, Romain Nguyen and Nenad Pavin. I thank them for good team work and interesting hints and questions. Especially, I would like to thank Giovanni Meacci for passing his knowledge in culturing bacteria over to me.

I am obliged to Ernesto Nicola and Benjamin Lindner for answering many questions regarding bifurcations, amplitude equations, stochastic processes and noise.

I greatly acknowledge the help of Regine Hartmann during my experimental work. She made it possible that I could work in the lab showing a true greenhorn how things have to be handled. I appreciated very much her help and her instructions. Also, I thank Jonathan Howard that he let me work in his lab at the MPI CBG. Furthermore, I am grateful to the team of the light microscope facility at the MPI CBG who kindly gave me my first lessons in fluorescence microscopy.

I am obliged to Joe Lutkenhaus and William Margolin for the generous donation of bacterial strains which I have been working with during my PhD project.

I would like to thank Stefan Diez for taking the time to apply TIRF to *E. coli* cells in order to check for MinD helices.

I am grateful to Nadine Baldes, Francine Jurecka, Ulrike Keil and Christina Matthes for keeping track of administrative things and bureaucratic necessities. They were always friendly and helpful. I also thank Ilona Augustz for helping us to find a kindergarten place for our little daughter Hannah.

I would like to thank my fellow students Christian Simm, Tilo Schwalger, Konstantin Doubrovinski, Stefan Günther, Thomas Bittig, Reza Farhadi Far, Kai Dierkes, Lars Wolff, Diana Clausnitzer, Jonas Ranft and the rest of the biological physics group at the MPI PKS for good discussions on science and things beyond as well as for a good company.

I am grateful to Hubert Scherrer-Paulus, Lars Bartosch, Thomas Müller, Marcus

Herz, Helmut Deggelmann and Torsten Goerke for keeping our computers alive and well-behaved. It saved a lot of valuable time that I did not have to worry that much about computer problems myself.

A very big thank-you also goes to Benjamin Friedrich for much encouragement and support as well as valuable scientific hints.

My PhD thesis was funded and supported by

- the Max Planck society, and
- the German National Academic Foundation.

This is gratefully acknowledged.

Contents

1	Introduction	1
1.1	Why bacteria are fascinating	1
1.2	Self-organization in nature	2
1.3	Outline of the thesis	4
2	The Min system in the bacterium <i>Escherichia coli</i>	7
2.1	What are Min oscillations?	8
2.2	Reaction kinetics of Min proteins	9
2.3	Understanding Min oscillations	12
2.3.1	Previous theoretical work on Min oscillations	12
2.3.2	A theoretical description of Min oscillations - the aggregation current (AC) model	15
2.3.3	Another theoretical description using cooperative attachment (CA)	16
3	Surface waves of Min proteins predicted by the aggregation current (AC) model	19
3.1	Circumferential modes of Min oscillations	20
3.1.1	<i>In vivo</i> study: Min proteins break rotational symmetry in <i>Escherichia coli</i>	24
3.2	Surface waves in a flat, open geometry	27
3.3	Pattern formation in the open system: derivation of the amplitude equations for the AC model	32
3.3.1	Discussion of stability regimes	39
3.3.2	Patterns in two space dimensions	39
4	<i>In vitro</i> patterns of Min-proteins on a planar membrane	43
4.1	Min proteins organize into surface waves <i>in vitro</i>	43
4.1.1	Estimation of <i>in vitro</i> diffusion constants of MinD and MinE	47
4.2	Modeling <i>in vitro</i> dynamics of Min proteins	51
4.2.1	Numerical methods and parameter choice	53
4.3	Solutions of the derived CA model in cell geometries	57
4.3.1	Wild type cells	57
4.3.2	Thick cells	57
4.3.3	Filamentous cells	61

5	Mobility of Min proteins in <i>Escherichia coli</i> measured by fluorescence correlation spectroscopy	63
5.1	Materials and Methods	64
5.1.1	Strains	64
5.1.2	Optical setup	64
5.1.3	Theoretical autocorrelation curves	64
5.2	Data analysis	66
5.3	Measurement results and discussion	68
6	Min oscillations and cell growth	77
6.1	Min pattern in short “newborn” <i>E. coli</i> cells	77
6.1.1	Materials and Methods	78
6.1.2	Results	79
6.2	Min oscillations in filamentous “overaged” cells	87
7	Conclusions and Outlook	89
7.1	Summary of results	89
7.2	Outlook on future work	91
A	The case of large diffusion constants in the aggregation current model	93
B	Calculation of the linear spreading velocity	95
C	Derivation of amplitude equations	97
D	Particle-based version of the aggregation current model	105
E	Glossary	107
	Bibliography	109

Chapter 1

Introduction

1.1 Why bacteria are fascinating

They are essentially everywhere and we tend to dislike them. Each cough or sniff reminds us of their presence in our body and environment. Bacteria constitute a large fraction of the world's biomass [1]. Their habitats literally range from the highest mountain to the deepest sea which is due to their robustness and adaptability. In our body, bacterial cells are more numerous than the actual human cells which contain our genome. Their presence can make us suffer from diseases like cholera, anthrax and the bubonic plague. However, we also benefit from them in many ways. For instance, the bacterial flora in the gut enhances the immune system, increases the yield of nutrient uptake and regulates fat storage [2]. Bacteria form an own biological kingdom which comprises a huge number of species. Most of these have not yet been characterized by scientists. They are extremely diverse and occur in a variety of different shapes, with various cellular compositions, metabolic pathways and behavioral strategies. In contrast to eukaryotes, bacteria do not have a cell nucleus or other membrane-enclosed cell organelles. Their DNA is dispersed freely in the cytoplasm [3]. A rigid cell wall makes them resist osmotic pressure [3]. Only some years ago, bacteria were seen as unspectacular sacs of enzymes. Scientific results of the past few years revised this view and showed that bacterial cells contain cell-skeletal structures just as eukaryotes. Their cytoskeleton helps to maintain the cell shape, to perform cell division and to transport material within the cell [4]. The bacterial cytoskeleton is made up of proteins which polymerize to filaments with lengths in the micrometer range. Some of these proteins are evolutionary related to the components of the eukaryotic cytoskeleton, actin, tubulin and intermediate filament proteins. Other cytoskeletal proteins in bacteria have no counterpart in the eukaryotic world [4].

- One example of a cytoskeletal protein highly conserved in bacteria is the tubulin homolog FtsZ. It polymerizes in the presence of the chemical fuel GTP and forms the essential scaffold of the Z-ring which constricts cells during cell division [4].
- The actin homolog MreB is also found in many bacterial species. It assembles to dynamic helical polymers beneath the membrane and extends throughout the cell. MreB plays a role for the maintenance of the cell shape by guiding the synthesis of new cell wall material [4].
- In the bacterium *Caulobacter crescentus*, the protein Crescentin has been identified to contribute to the typical crescent shape of this bacterium. It is a homolog of proteins which build up the intermediate filaments in eukaryotes.

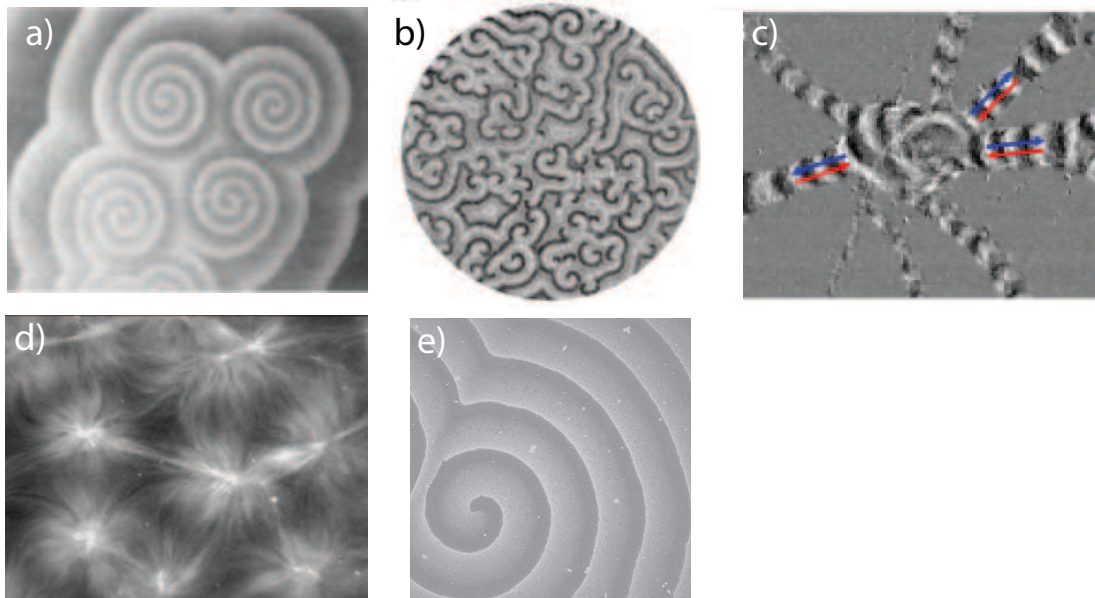


Figure 1.1: Patterns formed by self-organization. a) Patterns of the Belousov-Zhabotinsky reaction in a petri dish, taken from [5] with permission. b,c) The amoeba *Dictyostelium discoideum* during the process of chemotactic cell aggregation. In response to cAMP signaling, cells move and slightly elongate changing their light scattering properties. Thereby, cAMP waves can be made visible by dark field microscopy [6]. Images are taken from [6] with permission. b) cAMP waves in a spread of amoebae cells during an early stage of cell aggregation. c) In a later stage, amoebae mounds have formed and cells from the surrounding move towards the core. cAMP waves travel outwards. Red arrows indicate the direction of cell movement, whereas blue arrows indicate the direction of cAMP wave propagation. d) Self-organized asters of microtubules and kinesin motors in a dark field micrograph, taken from [7] with permission. e) Spiral wave of fluorescently labeled MinE. The self-organized Min protein structures form *in vitro* on a supported lipid bilayer, immersed in a buffer with MinD, MinE and ATP.

- The protein MinD and related proteins form a fourth family of highly conserved proteins in bacteria and play a key role in subcellular organization. They take part in the selection of the division site of the bacterium. In this thesis, we aim to understand how the spatiotemporal patterns are formed which are produced by the Min proteins in *E. coli*.

1.2 Self-organization in nature

How does it come about that a huge container of proteins and other molecules suddenly forms structures as elaborate as the mitotic spindle or the contractile ring of cell division¹? The evolution of biological processes has kept biologists busy for centuries and also attracted the attention of physicists in the last decades. Much is known about the proteins involved in cellular processes and about their interactions. However, when reading a biology text book one often gets the idea

¹See the glossary for explanation of mitotic spindle and contractile ring.

that there is an invisible hand which drives ingredients of a cell at the right moment to the right place in order to accomplish a cellular process. The origin of the forces which drive molecules to a certain position during the life cycle of a cell is often not obvious. An illustrating example is the observation that a rod-shaped *E. coli* cell divides in the middle and aggregates its division machinery there. The question arises how the cell actually knows where its middle is and how this is communicated to the particles involved in division. The answer is not yet entirely known but there is strong evidence that it is related to a self-organizing process in the *E. coli* cell, namely the oscillation of Min proteins. The emerging pattern of Min proteins highlights the cell middle as much as a swinging pendulum highlights its resting point. Self-organization is a process by which patterns can emerge in systems with many particles of a few different sorts. The patterns which emerge are determined by the dynamical parameters of the system and by the geometry of the container in which the particles are confined. The length scale of the pattern is by orders of magnitude larger than the size of the involved particles. It is usually on the micrometer scale if the particles are molecules within a cell. Pattern formation by self-organization comes about by local interactions between particles and spatial coupling, e.g. by diffusion. Local interactions of particles typically emerge from chemical reactions, particle attraction or particle repulsion.

Self-organization seems to contradict the laws of thermodynamics as emerging spatial order decreases the entropy in the system. Indeed, thermodynamics states that the free energy of a system in contact with a heat bath has to be minimal. The Boltzmann principle assigns an extremely small probability to low entropy states of a system at room temperature or higher temperatures. Thus, spatial order would essentially never occur in such a system in thermal equilibrium. The solution to this apparent paradox is that thermodynamics does not apply to self-organizing systems since these are not in thermal equilibrium. Self-organization can only be maintained if the system is kept away from thermal equilibrium by constant energy consumption which is often accomplished by the hydrolyzation of the chemical fuel ATP in biological systems. Patterns emerging from self-organization are thus also termed dissipative structures since they rely on the continuous dissipation of energy. Nicolis and Prigogine describe the maintenance of dissipative structures in the following way [8]: “An appropriate illustration would be a town that can only survive as long as it is a center of inflow of food, fuel, and other commodities and sends out products and wastes.”

The most famous example of pattern formation by self-organization is presumably the Belousov-Zhabotinsky reaction. This class of chemical reactions results in chemical oscillations which can also give rise to dynamical spatial structures, typically rings and spirals, see Figure 1.1a. The reaction was discovered by the chemist Boris Belousov in the 1950s. A pioneering theoretical work on pattern formation in biology was published in 1952 by Alan Turing [9]. Turing focused on the mathematical description of self-organization in systems motivated from embryogenesis. Later, the chemist Ilya Prigogine studied self-organization in dissipative systems and applied nonequilibrium thermodynamics and the theory of dynamical systems to explain them [8]. He gained the Nobel price for chemistry in 1977 as approval of his work. Today, self-organization is known as a pattern-forming mechanism in biology, chemistry and physics. It embraces a wide field of theoretical and experimental research. A review of pattern formation in nonequi-

librium systems can be found in [10].

In biology, self-organization occurs on the cellular and subcellular level. In the following, we will give some examples.

Pattern formation on the cellular level

cAMP waves. The amoeba of the species *Dictyostelium discoideum* live as unicellular organisms in the soil. Upon shortage of nutrients, cells show social behavior and aggregate to a multicellular structure, the so-called slug. The slug migrates as a whole in response to environmental signals. In case of further lack of food, it ripens to a fruiting body containing spores. The aggregation of single cells works by chemotaxis which is mediated by the signaling molecule cAMP. By the interplay of cell migration, adaptation and induced cAMP release of cells, beautiful cAMP wave patterns form in the cell aggregate. An example, taken from [6] is presented in Figure 1.1b,c. Indeed, Dictyostelids form patterns in two ways: First, the cells release cAMP in a concerted manner such that patterns in the cAMP concentration form all over the cell spread. Secondly, the amoebae form patterns of the cell density by condensing into a multicellular structure.

Pattern formation on the subcellular level

Microtubule asters. The microtubule asters which form as part of the mitotic/meiotic spindle during cell division can emerge from self-organization. Aster formation could be reconstituted *in vitro* [7]. From a mixture of tubulin, motor proteins and ATP, microtubule asters and vortices form spontaneously, see Figure 1.1d. Computer simulations reproduced these structures [7,11].

Min waves. The Min proteins MinD and MinE oscillate from pole to pole in the rod-shaped *E. coli* cell. Pattern formation of MinD, MinE and ATP can also be found *in vitro* on a supported lipid bilayer immersed in a buffer [12], see Figure 1.1e. A simple theoretical description yields similar structures as observed *in vitro* and reproduces at the same time oscillations in a one-dimensional cell geometry [12].

1.3 Outline of the thesis

In this thesis, we study pattern formation in the Min system of the bacterium *Escherichia coli* theoretically and experimentally. Especially, we will consider the aspect of self-organization as a mechanism which can generate the structures observed in the Min system.

The following chapter gives background information on the bacterium *Escherichia coli* and experimental results on Min proteins. Also, it gives an overview of the theoretical descriptions of the Min system which have been suggested in the literature.

In the third chapter, we discuss a mean field description of the Min system. It assumes that MinD proteins feel mutual interactions in the membrane-bound state thus inducing an aggregating current of MinD on the membrane. Earlier studies in one space dimension had demonstrated that this approach can reproduce Min oscillations in the cell [13]. To learn more about the dynamical system and to make predictions for the real Min system, we now examine the dynamics in different geometries. Numerical and theoretical analyses predict the occurrence of

surface waves in geometries that differ from the wild type cell tube. We especially discuss the case of cells with enlarged radii and the case of Min patterning on a flat surface.

The fourth chapter starts with a summary of Min pattern formation *in vitro* [12]. In the respective experiments, MinD and MinE form patterns on a flat membrane surface in the presence of ATP. We discuss the implications of the experiments for existing theoretical descriptions of Min oscillations in the cell and suggest a computational mean field model which qualitatively reproduces the protein structures found experimentally.

In the fifth chapter, we present measurements on fluorescent MinD and MinE proteins in living *E. coli* cells by fluorescence correlation spectroscopy *in vivo*. An analysis of the data allows to extract characteristic time scales of the Min system *in vivo*. Two of these are associated to MinD and MinE mobility in the cytoplasm of the cell.

The sixth chapter is dedicated to Min oscillations in the context of cell growth. We report experimental results where *E. coli* cells, expressing GFP-MinD, were recorded over time spans on the order of the cells' life cycles. We have found that in short "newborn" cells, which are around $2\mu\text{m}$ in length, Min concentration maxima switch far less regular between the cell poles than in *E. coli* cells prior to division. We have analysed data of a large number of short cells and find that Min switching gets more regular when the cell lengthens. Furthermore, we have observed the process of Min pattern change in cells growing filamentous, i.e. larger than typical *wild type cells*.

Chapter 2

The Min system in the bacterium

Escherichia coli

The bacterium *Escherichia coli*

Escherichia coli is a rod-shaped bacterium living for instance in the intestine of humans and other endothermal animals, see Figure 2.1. The cell length ranges for wild type cells from 1.5–4 μm depending on the chosen strain. The cell diameter is about 1 μm . They are gram-negative bacteria, that is they have an inner and an outer cell membrane. In between these membranes, there is a rigid layer of peptidoglycan, which is a polymer made of sugars and amino acids. This layer gives the cell a fixed shape and counteracts the osmotic pressure, which could otherwise make the cell burst [3].

Many *E. coli* strains are flagellated. Their flagella have a peritrichous arrangement, i.e. they point in different directions. These motile strains are able to perform chemotaxis by switching between a run and a tumble mode of motion. In the tumble mode the cell reorients randomly its swimming direction. In the run mode it performs straight swimming. To follow the direction of chemical gradients it adapts the length of run and tumble modes according to the temporal change of chemoattractant concentrations [3,14].

As all other prokaryotes, *E. coli* contains no nucleus or other cell compartments such as mitochondria or an endoplasmic reticulum usually found in eukaryotes. The cell contains one chromosome, dispersed in the cytoplasm, and in addition several plasmids. The bacterium divides by binary fission forming a septum in the middle of the bacterium. In nutrient-rich medium at a temperature of 37°C, division can take place every 20 minutes. Before the cell divides, the chromosome is duplicated and segregates to either half of the cell. Two mechanisms help the cell to locate its division machinery in the cell middle. Nucleoid occlusion impedes septum formation over the DNA [15,16] and the Min system keeps septum formation away from the cell poles [17]. If the Min system is not functional the septum can form at the cell poles leading to mini-cells void of DNA.

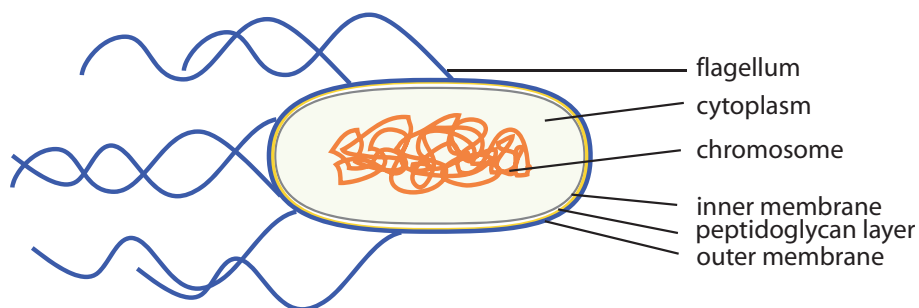


Figure 2.1: Sketch of *Escherichia coli* cell

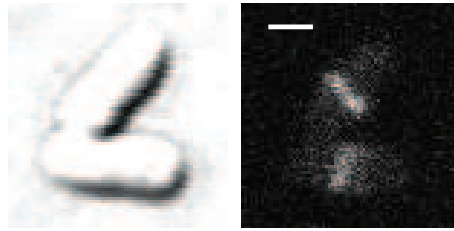


Figure 2.2: The Z-ring in two *Escherichia coli* cells of the strain EC448. The left image shows the cells in a DIC-micrograph. The image on the right shows the fluorescently labeled protein FtsZ constituting the Z-ring. It is located in the cell middle and attached to the inner side of the bacterial membrane. The location of the Z-ring determines the future division site of the bacterium. The positioning of the Z-ring is guided by the Min system and nucleoid occlusion. The scale bar is $1\mu\text{m}$ long.

2.1 What are Min oscillations?

Min proteins are a class of proteins that is widely conserved among bacteria. They are involved in locating the cell division machinery of the bacterium to the cell middle. In *E. coli*, there are three Min proteins, MinC, MinD and MinE. They have been found to form spatiotemporal patterns in the *E. coli* cell — the so-called Min oscillations [4]. Although Min proteins occur in many bacterial species and even cell organelles, such as chloroplasts and mitochondria, they are not found to perform oscillations in all occurrences. For instance, in the bacterium *Bacillus subtilis*, MinE is missing and MinD and MinC are statically distributed at the poles [4].

Min proteins are encoded in one operon on the single chromosome of the bacterial cell and thus form a functional unit in the cell metabolism. They were found to chemically interact with each other and to locate to the cytoplasmic membrane of the bacterium in a dynamic and spatially heterogeneous manner. The cytoskeletal structure constituted by Min proteins is called the Min system. The Min system plays an important role in inhibiting cell division at the cell poles. The division site is determined by the formation of the Z-ring [18], which is a ring-shaped polymer network formed by the protein FtsZ, see Figure 2.2. MinC depolymerizes FtsZ filaments [19] and sweeps off FtsZ polymers at the cell poles during Min oscillations.

How does the dynamic redistribution of Min proteins look like? The standing wave of MinD in an *E. coli* cell is illustrated in Figure 2.3. MinD accumulates at the inner side of the bacterial membrane in one cell half. After a characteristic residence time, this concentration maximum resolves and switches to the opposite cell half [20]. At the same time, MinE forms a ring on the membrane at the rear of the MinD-maximum close to the cell middle [21]. A lower concentration of MinE is also present directly at the pole where MinD is aggregated. When the MinD-maximum starts to switch to the opposite cell side, the MinE-ring moves towards the cell pole, disappears, and rebuilds at the rear of the new MinD maximum at the opposite side of the cell [22]. The distribution of MinC follows the dynamics of MinD and oscillates from pole to pole [19,23]. The oscillation periods differ from cell to cell and range from about 40 to 120 seconds. In mutant

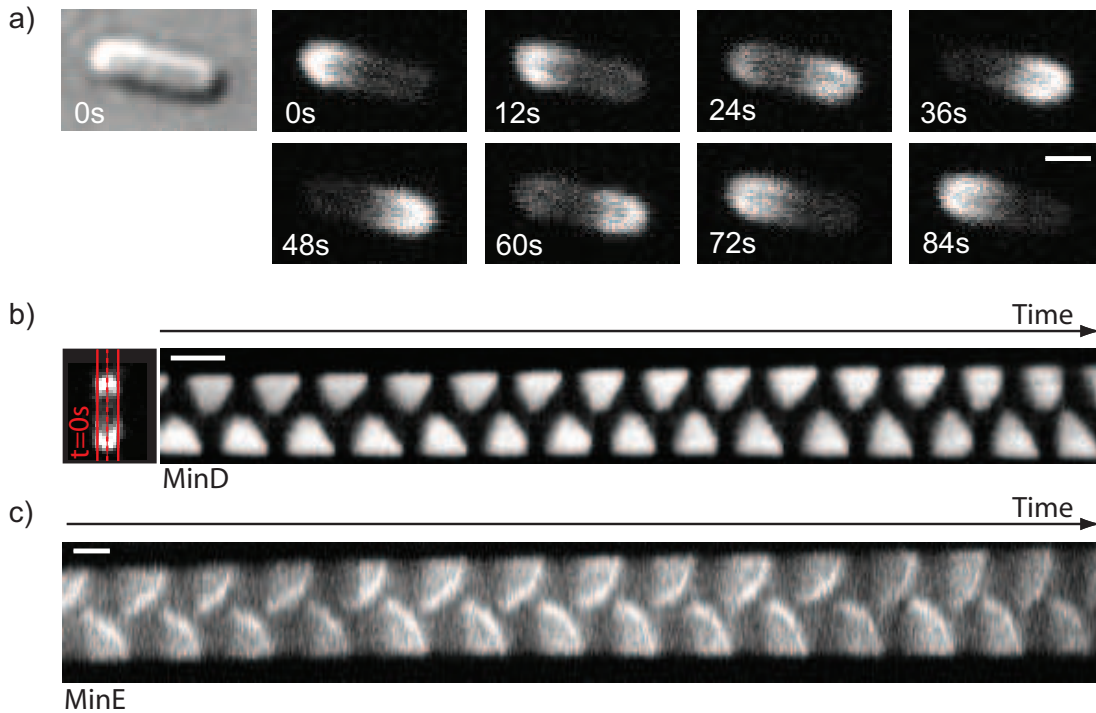


Figure 2.3: Oscillation of MinD (a and b) and MinE (c) in *Escherichia coli* cells. a) Time series of a cell with fluorescently labeled MinD. The leftmost image shows the cell in a DIC-micrograph. The remaining images show fluorescently labeled GFP-MinD in the cell for ascending times. MinD maxima locate to one cell pole and switch to the opposite pole after a characteristic residence time. The scale bar is $1\mu\text{m}$ long. b) Kymograph of fluorescently labeled MinD in an *E. coli* cell with initial cell length of $3.8\mu\text{m}$ covering a time interval of 17min. The leftmost image shows the cell at time= 0s and indicates how the kymograph was produced. The fluorescence was recorded along the red line and averaged over the line width. The kymograph then shows the time evolution of light intensity along this line. c) Kymograph of fluorescently labeled MinE in an *E. coli* cell with initial cell length of $4.8\mu\text{m}$ covering a time interval of 28min. The kymograph was produced in the same way as in b). The scale bars show 1min.

strains with filamentous cells, which exceed the length of a typical wild type cell, the oscillation pattern of the Min proteins changes [20], see Figure 2.4. In this case, the standing wave of Min proteins gains wave nodes. This suggests that the Min system has an intrinsic wavelength like a dynamical system which oscillates beyond a Hopf bifurcation with finite wavelength.

2.2 Reaction kinetics of Min proteins

The key players of the oscillation were identified to be MinD and MinE. Both proteins are needed to sustain the oscillations. MinC-depletion, however, does not stop the oscillations [20]. MinC binds to MinD on the membrane and follows the dynamics of MinD.

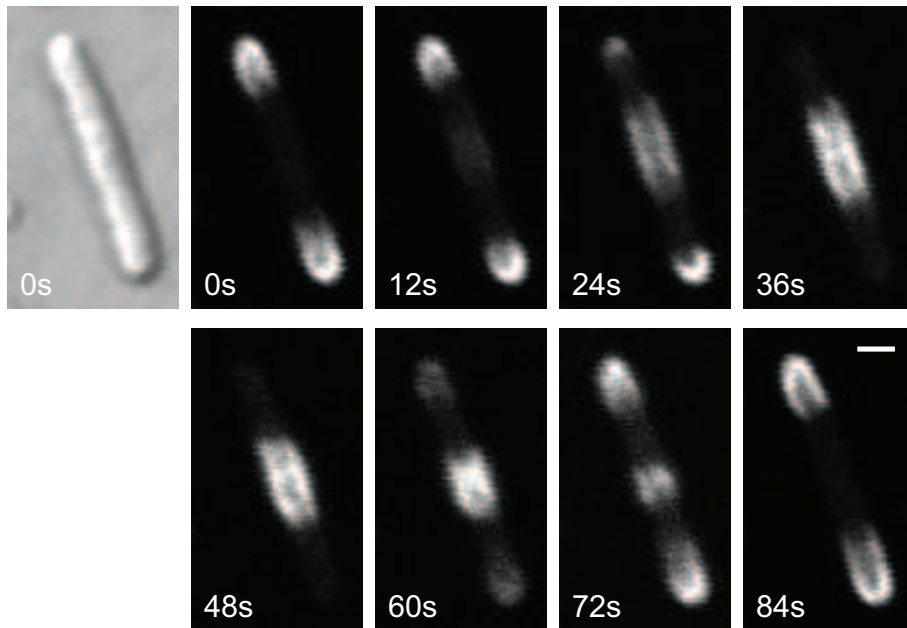


Figure 2.4: Oscillation of MinD in a filamentous *Escherichia coli* cell. The left-most image shows the cell in a DIC-micrograph. The remaining images show fluorescence micrographs of GFP-MinD. MinD maxima are first located at both cell poles and then switch to the cell middle and so forth. The scale bar is $1\mu\text{m}$ long.

In vitro experiments have shown that MinD is an ATPase and has a high binding affinity for the inner cytoplasmic membrane when ATP is present [24,25]. For high concentrations, MinD was found to polymerize on phospholipid vesicles pulling out membrane tubes [24]. MinD in the presence of ATP γ S, which is a non-hydrolyzable analog of ATP, does bind to the membrane, but does not form aggregates. This indicates that binding and aggregation of MinD on the membrane is a two-step process. Also, an analysis [26] including a yeast two hybrid system² revealed that most of the interaction between MinD is lost, if either the prey or the bait MinD is not capable to bind to the membrane. This supports the conjecture that the MinD-MinD interaction is stronger in the membrane-bound state.

The presence of cooperative effects during attachment of MinD to phospholipid membrane is indicated by *in vitro* experiments which show that MinD binding deviates from Langmuir isotherms [27] and can be described by a Hill function with a Hill coefficient of 2 [28].

MinE is recruited to the membrane by MinD and promotes there the ATPase activity of MinD. After ATP-hydrolysis, MinD falls off the membrane and goes back into the cytoplasm (see Figure 2.5a). These *in vitro* results are consistent with *in vivo* findings in bacterial cells. If cells are void of MinD, then MinE is spread homogeneously in the cytoplasm. In contrast, MinE-depleted cells have MinD homogeneously spread on the cytoplasmic membrane [20].

Specific mutations of the topological specificity domain in MinE have been shown to result in a loss of the MinE ring although Min oscillations were still present [29].

²See the glossary for ‘yeast two hybrid system’.

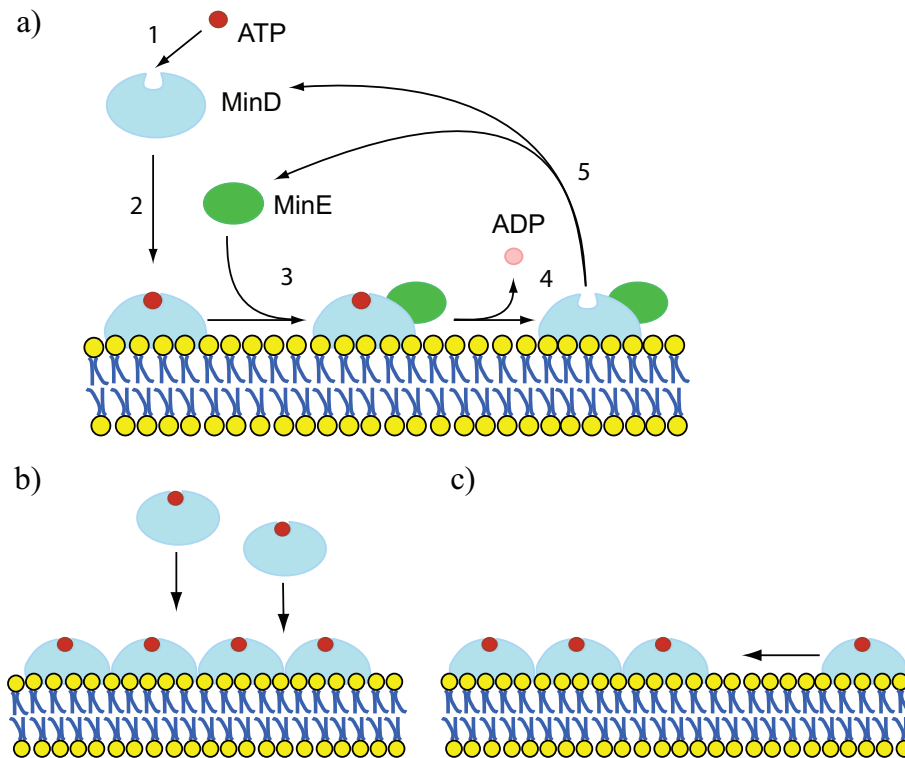


Figure 2.5: a) Binding and unbinding cycle of MinD and MinE in the *E. coli* cell. Cytoplasmic MinD binds ATP (1) and attaches to the membrane (2). Bound MinD recruits MinE to the membrane (3) which catalyzes hydrolyzation of ATP. ADP is released into the cytoplasm (4) and MinD and MinE fall off from the membrane (5). b) and c), different conceivable aggregation mechanisms of bound MinD. b) MinD attaches preferably where MinD is already bound. c) MinD attaches unbiased and moves then in the bound state due to mutual interactions.

In these cells, MinD maxima grew beyond their normal arrest point at the cell middle and minicelling occurred at low rates. These experiments suggest that the MinE ring is not necessary for Min patterning in the cells.

Furthermore, Shih and colleagues [30] have reported helical Min structures forming a substructure of the protein aggregates at the cell pole on the inner bacterial membrane. The authors suggest that concentration maxima of MinC, MinD and MinE are formed by helical Min protein polymers. They conjecture that the MinE ring is formed by a helical MinE polymer which grows beyond the MinD helix located at the cell pole. The meaning of these helix structures for the generation of Min oscillations remains however obscure. Even the existence of these structures for different strains and growth conditions than those reported in [30] is not fully evident.

Experimental results have shown that protein synthesis and degradation do not play a major role for Min oscillations [20].

2.3 Understanding Min oscillations

The dynamic relocation of Min proteins cannot be naively concluded from local biochemical interactions of the molecules [31] since the patterns are on the scale of microns whereas the molecules are only few nanometers in size. Pattern formation in the Min system is a collective effect and needs many molecules interacting in the cell geometry. This fact indicates that the Min system is self-organizing: The homogeneous state of protein distributions in the cell is dynamically instable, i.e. small inhomogeneities created by fluctuations are amplified. After a certain transient evolution, the system ends up in a characteristic spatiotemporal pattern dependent on the geometry of the cell.

Pattern formation in the Min system resembles that of a dynamical system operating close to a Hopf-bifurcation with finite wavelength. This is because protein distributions oscillate similarly to a standing wave with characteristic frequency and wavelength.

2.3.1 Previous theoretical work on Min oscillations

Several computational descriptions of the Min system have been presented in the past. All of them were able to generate oscillations, which resembled those observed in wild-type cells. All models share the following basic assumptions: MinD and MinE interact with each other and with the membrane. MinD can attach to the membrane. Membrane-bound MinD in turn can then bind MinE from the cytoplasm. MinE bound to MinD promotes detachment of MinD from the membrane. Particles in the cytoplasm are subject to diffusion. All models conserve particle numbers of MinD and MinE apart from the model presented in [32].

Beyond these basic components, the models differ in many respects. They can be distinguished according to different criteria.

Some models are deterministic and use a mean field description, others are particle-based.

Deterministic models describe protein distributions by concentrations depending on space and time coordinates. The time evolution of the system is completely determined by these concentrations, and stochastic effects are not directly incorporated. Deterministic descriptions have been presented in [12,13,32–37].

Particle-based models were described in [38–41]. In these models, the time evolution of a number of discrete Min proteins is simulated. State changes of the proteins and translocation by diffusion are decided using random number generators.

Furthermore, the proposed models can be divided into two classes according to the mechanism by which the dynamic instability of the modeling dynamical system is generated.

Aggregation current. The works by Kruse [34] as well as Meacci and Kruse [13] use a description in which an aggregation current of membrane-bound MinD leads to a build up of concentration maxima and thus a destabilization of the homogeneous state (see Figure 2.5c). This kind of models will be referred to as aggregation current (AC) models. Here, binding of Min proteins is not considered to be cooperative.

Cooperative attachment. All other publications suggest that a certain kind of cooperativity in binding of MinD or MinE to the membrane leads to the instability (see Figure 2.5b). That means, they assume that the binding rate of MinD (MinE) is enhanced by MinD (MinE) which is already bound to the membrane. We will call this kind of models cooperative attachment (CA) models.

In the following, we will describe the models in greater detail.

- The description by Meinhardt and de Boer [32] includes cooperativity in binding of MinD and MinE to the membrane, i.e. the binding rates increase with the concentration of already bound MinD or MinE, respectively. Protein degradation and production are directly included in the dynamic equations. Experimentally, this had been shown to be of minor or no importance for the Min oscillations [20].
- The model of Howard and coworkers [42] assumes that cytoplasmic MinD recruits MinE to the membrane. In the bound state, MinE promotes the release of MinD into the cytoplasm. Furthermore, new MinD-binding to the membrane is reduced by bound MinE. A stochastic version of this model is presented by Howard and Rutenberg in [43]. There, the authors report that fluctuations can be essential for certain parameter regimes at low particle numbers. Also, the role of noise on the location of the period-averaged MinD concentration along the cell long axis is discussed.
- In the description of Kruse [34], membrane-bound MinD attracts MinE to the membrane, which then catalyzes release of MinD into the cytoplasm. MinE detaches spontaneously. In the bound state, MinD is assumed to move due to mutual protein interactions. This is modeled by an aggregation current of MinD which creates MinD-concentration maxima.
- Huang and colleagues [35] suggest a system in which MinD binds cooperatively to the membrane, i.e. the binding rate increases with the concentration of bound MinD molecules. When MinE is bound to the membrane it is assumed to form a protein complex with MinD. This complex is released in one from the membrane with a certain rate. The equations take explicitly the ATP loading of MinD in the cytoplasm into account. The dynamic equations are explicitly given by

$$\begin{aligned}
\partial_t c_{D:ADP} &= -\sigma_D^{ADP \rightarrow ATP} c_{D:ADP} + \sigma_{de} c_{de} \delta(\mathcal{S}) && + D_D \Delta c_{D:ADP} \\
\partial_t c_{D:ATP} &= +\sigma_D^{ADP \rightarrow ATP} c_{D:ADP} - [\sigma_D + \sigma_{dD} (c_d + c_{de})] c_{D:ATP} \delta(\mathcal{S}) && + D_D \Delta c_{D:ATP} \\
\partial_t c_E &= -\sigma_E c_d c_E \delta(\mathcal{S}) + \sigma_{de} c_{de} \delta(\mathcal{S}) && + D_E \Delta c_E \\
\partial_t c_d &= -\sigma_E c_d c_E + [\sigma_D + \sigma_{dD} (c_d + c_{de})] c_{D:ATP} \\
\partial_t c_{de} &= +\sigma_E c_d c_E - \sigma_{de} c_{de}.
\end{aligned} \tag{2.1}$$

Here, $c_{D:ADP}$, $c_{D:ATP}$ and c_E are the concentrations of MinD-ADP, MinD-ATP and MinE molecules in the cytoplasm. Membrane-bound MinD is denoted by c_d and the concentration of the MinDE complexes on the membrane is symbolised by c_{de} . $\delta(\mathcal{S})$ denotes the delta function being unequal to zero only on the inner membrane surface of the cell. The parameters σ_{de} , σ_E , σ_D , σ_{dD} characterize the rates of MinDE detachment, MinE attachment, spontaneous and cooperative MinD attachment, respectively. The

exchange of ADP for ATP in MinD is described by the rate $\sigma_D^{ADP \rightarrow ATP}$. D_D and D_E are the constants of diffusion in the cytoplasm for MinD and MinE.

- The work by Meacci and Kruse [13] modifies the description in [34] by taking on the idea of MinDE complexes on the membrane. Since we will study this model extensively in this thesis, a more elaborate description will be given in the following section.
- A deterministic model motivated by the picture of polymerising and depolymerising protein filaments was presented by Drew *et al.* [36]. This one-dimensional description assumes that MinD polymers are nucleated at the pole and grow by recruiting cytoplasmic MinD. MinE can attach to MinD within the polymer either at internal MinD proteins or at the polymer end. If MinE attaches to the terminal MinD protein, the MinD polymer is capped, further growth is prohibited and depolymerisation is induced. MinE caps nucleate at the same time MinE polymers which grow towards the middle of the cell. The dynamic equations use concentration fields for Min polymers and monomers.

All stochastic simulations described in the following are derived from the deterministic model given in [35] whose dynamic equations are listed in (2.1).

- Pavin, Paljetak and Krstić [40] performed three-dimensional stochastic simulations. They assume that MinD forms two-stranded polymers in the membrane-bound state. MinE can attach to each MinD-molecule within the polymer and the resulting hydrolysis rate depends on the number of bonds the MinD molecule maintains within the polymer.
- Kerr *et al.* [38] show computations which clarify the effect of the number of proteins in the cell.
- Tostevin and Howard [39] presented 1D stochastic computations examining the dependence of the oscillation period on the MinD and MinE concentration and the cell length. Also, they study the segregation of Min proteins to the daughter cells during cell division.
- Fange and Elf [41] made a 3D stochastic analysis for various mutant types of *E. coli*. They found stochasticity to be important to reproduce Min dynamics in spherical cells and to reproduce the random MinD clusters in mutant cells which lack the lipid phosphatidylethanolamine (PE) in the cytoplasmic membrane.

In this thesis, we will consider two computational models based on different underlying assumptions on what aspect of Min protein interactions causes the instability in the Min system. Experimentally, this has not yet been clarified and both models are based on plausible scenarios. In the forthcoming sections, we will give an introduction to either of the computational models.

2.3.2 A theoretical description of Min oscillations - the aggregation current (AC) model

To generate an instability in a dynamical system that describes the Min system, two ways are readily at hand. One possibility is to include nonlinearities in the binding or unbinding terms that model the exchange of MinD and MinE with the membrane. This can give rise to the formation of concentration inhomogeneities. An alternative way is to include a current term for membrane-bound proteins which drives the formation of protein aggregations on the membrane.

There have been experimental findings which support the latter idea of Min proteins moving on the membrane due to mutual interactions. *In vitro* experiments, which involved a non-hydrolyzable ATP-analog, suggested a two-step mechanism for the formation of MinD helices [24]. According to this mechanism, MinD would first bind to the membrane and subsequently form clusters. Further support for MinD interactions in the membrane-bound state gave a yeast two-hybrid assay (see glossary), in which two populations of MinD interacted more strongly when both populations were on the membrane as compared to only one or neither of the populations being membrane-bound [26].

In the computational description which we present here, the distributions of MinD and MinE in the cytoplasm are described by the concentration fields c_D and c_E , that are defined in the interior of the cell. The distributions of MinD and MinDE complexes bound to the membrane are given by the fields c_d and c_{de} , that are defined on the two-dimensional boundary of the cell. In the following, the cell shape will be assumed to be a cylinder with two hemispherical caps at both ends. The interior of this shape is identified with the cytoplasmic domain. The dynamic equations for the densities capture the exchange of MinD and MinE between the cytoplasm and the membrane, diffusion, and the transport of membrane-bound MinD molecules, which are subject to mutually attractive interactions. The time change of the four concentration fields is explicitly given by

$$\partial_t c_D = -\omega_D(c_{\max} - c_d - c_{de})c_D\delta(\mathcal{S}) + \omega_{de}c_{de}\delta(\mathcal{S}) + D_D\Delta c_D \quad (2.2)$$

$$\partial_t c_E = +\omega_{de}c_{de}\delta(\mathcal{S}) - \omega_E c_d c_E \delta(\mathcal{S}) + D_E\Delta c_E \quad (2.3)$$

$$\partial_t c_d = +\omega_D(c_{\max} - c_d - c_{de})c_D - \omega_E c_d c_E - \nabla \cdot \mathbf{j}_d \quad (2.4)$$

$$\partial_t c_{de} = -\omega_{de}c_{de} + \omega_E c_d c_E. \quad (2.5)$$

Here, c_{\max} is the maximal density of MinD on the membrane and the parameters ω_D , ω_E , and ω_{de} determine the rates of MinD- and MinE-binding to the membrane and of MinDE-unbinding from the membrane. Binding is restricted to particles in the vicinity of the cytoplasmic membrane by $\delta(\mathcal{S})$, where \mathcal{S} is the (inner) surface of the model bacterium. The diffusion constants of cytoplasmic MinD and MinE are D_D and D_E , respectively. The operator ∇ in Eqs. (2.4) denotes the gradient operator on the surface \mathcal{S} , while Δ is the Laplace operator in three dimensions.

The two-dimensional current \mathbf{j}_d , which describes transport of MinD bound to the membrane, has the form of a Cahn-Hilliard current [44],

$$\mathbf{j}_d = -D_d \nabla c_d + c_d(c_{\max} - c_d - c_{de})[k_1 \nabla c_d + k_2 \nabla \Delta c_d + \bar{k}_1 \nabla c_{de} + \bar{k}_2 \nabla \Delta c_{de}]. \quad (2.6)$$

In this expression, Δ and ∇ are the Laplace operator and the gradient on the

surface \mathcal{S} , respectively. D_d is the diffusion constant of MinD on the membrane and the coefficients k_1 and $k_2 > 0$ are parameters characterizing the interactions between MinD molecules. If $k_1 > 0$ then this interaction is attractive. Possible modifications of MinD-MinD interactions due to the binding of MinE to MinD are taken into account by the parameters \bar{k}_1 and \bar{k}_2 . For simplicity, a possible MinDE current is neglected. Furthermore, the equations do not incorporate a possible MinD dimerization before binding to the membrane [45]. Adding corresponding terms does not significantly alter the dynamics generated by the model for the parameters used. This can be understood by noting that the large diffusion constants of cytoplasmic MinD and MinE, $D_D \approx 15\mu\text{m}^2/\text{s}$ and $D_E \approx 10\mu\text{m}^2/\text{s}$ [46] result in an almost uniform spatial distribution of cytoplasmic MinD for cells a few micrometers in size. To a large extent, the effect of MinD dimerization prior to binding to the membrane can thus be accounted for by an appropriate value of the parameter ω_D .

In the following, we will consider c_{max} , k_1 and k_2 to be phenomenological parameters. In principle, though, their values are related to microscopic parameters [13,47,48]. A simple guess for the maximal density of membrane-bound MinD is $c_{\text{max}} = 1/(\text{lateral size of a MinD molecule})$, which leads to $c_{\text{max}} \approx 10^4\mu\text{m}^{-2}$. However, there is evidence that MinD binds only to specific lipids in the membrane reducing this value [28]. We will use a value of $c_{\text{max}} = 500\mu\text{m}^{-2}$ to produce oscillations that are compatible with experimental data. Furthermore, k_1 and k_2 give a characteristic length scale $r = (k_2/k_1)^{1/2}$ which determines the scale of the pattern generated by this mechanism. It therefore differs from the bare interaction range of the MinD-MinD interaction which should be on the order of a few nanometers.

In the limiting case of homogeneous cytosolic concentrations, the equations for the cytosolic concentrations decouple from the system (2.2)-(2.5), see Appendix 7.2. The resulting set of ordinary differential equations for the cytosolic fields c_D, c_E exhibits a stationary stable state C_D, C_E to which the system evolves asymptotically in time [13]. In this limit, the dynamics of the membrane concentration fields reads

$$\partial_t c_d = \omega_D C_D (c_{\text{max}} - c_d - c_{de}) - \omega_E C_E c_d - \partial_x j_d \quad (2.7)$$

$$\partial_t c_{de} = -\omega_{de} c_{de} + \omega_E C_E c_d. \quad (2.8)$$

An analysis of the above computational model will be presented in Chapter 3.

2.3.3 Another theoretical description using cooperative attachment (CA)

In vitro experiments including MinD, MinE and ATP in buffer on top of a supported lipid bilayer have shown pattern formation on length scales much larger than in *Escherichia coli* cells [12]. Traveling waves of proteins formed with wave lengths of about $80\mu\text{m}$. Regions of planar waves mixed with spirals and double spirals (see [12] and Figure 4.1). It is probable that self-organization in this *in vitro* system is based on the same chemical processes as the pattern formation in the cell.

Despite of extensive search in the parameter space, the aggregation current model

of the preceding section did not exhibit stable planar traveling waves as pattern on a plane. Also, bleaching experiments applied to the Min patterns observed *in vitro* showed that bleached areas within a fluorescent wave band were fix and did not follow the movement of the wave, see Figures 4.4. This indicates that the waves were not the result of protein movement on the membrane but of iterative detachment and reattachment of proteins from the buffer³. For this reason, we looked for an alternative model which would be able to reproduce the *in vitro* results and the oscillations in the cell at the same time. From the *in vitro* observation that regions of high MinE density on the lipid membrane initiated detachment of MinD, we derived a theoretical description which assumes cooperative attachment (CA) of MinE, as was already suggested in [32]. According to this theoretical description, the time evolution of the concentrations is given by the dynamic equations

$$\partial_t c_D = +\omega_{de}c_{de} - c_D(\omega_D + \omega_{dD}c_d) + D_D\Delta c_D \quad (2.9)$$

$$\partial_t c_E = +\omega_{de}c_{de} - c_Ec_d(\omega_E + \omega_{eE}c_{de}^2) + D_E\Delta c_E \quad (2.10)$$

$$\partial_t c_d = -c_Ec_d(\omega_E + \omega_{eE}c_{de}^2) + c_D(\omega_D + \omega_{dD}c_d) + D_d\Delta c_d \quad (2.11)$$

$$\partial_t c_{de} = -\omega_{de}c_{de} + c_Ec_d(\omega_E + \omega_{eE}c_{de}^2) + D_{de}\Delta c_{de}. \quad (2.12)$$

All concentration fields in the above equations are surface concentrations with units of an inverse area and the dynamics is assumed to take place in a plane. This is a simplification from the experiment where naturally concentrations of MinD and MinE in the buffer are volume concentrations and may vary in the z-direction (see Chapter 4.1).

The system is a reaction diffusion system and the terms in the equation model detachment and attachment reactions, diffusive transport in the buffer solution and in the membrane-bound state. Diffusive transport of the proteins is captured by the last terms in either equation. The respective attachment/detachment dynamics is parametrized by $\omega_D, \omega_{dD}, \omega_E, \omega_{eE}$ and ω_{de} . The instability in the system is generated by the nonlinearities in the MinD attachment rate $c_D(\omega_D + \omega_{dD}c_d)$ and the MinE attachment rate $c_Ec_d(\omega_E + \omega_{eE}c_{de}^2)$. Both rates increase with the concentration of the reaction product giving rise to a self-amplification. The detachment rate of membrane-bound MinDE is given by $\omega_{de}c_{de}$.

We assume that the exchange of ADP for ATP in unbound MinD is so fast that we do not have to consider explicitly the concentrations of MinD bound to ADP. For each rate we used only the terms with the lowest order non-linearity that were sufficient to reproduce the phenomena observed experimentally. All the parameters are effective parameters and might account for multiple processes.

³Assuming an aggregation current on the membrane does not necessarily mean that a bleached area moves along with the wave band, see Figure 3.9.

Chapter 3

Surface waves of Min proteins predicted by the aggregation current model

We study the theoretical description of Min oscillations based on an aggregation current (AC) of membrane-bound MinD proteins which has been introduced in Section 2.3.2. This computational model, also termed AC model, is motivated by experimental observations. *In vitro* experiments which involve a non-hydrolyzable ATP-analog suggest a two-step mechanism for the formation of MinD aggregates [24]. According to this mechanism, MinD would first bind to the membrane and subsequently form clusters. Further support for MinD interactions in the membrane-bound state resulted from a yeast two-hybrid assay, in which two populations of MinD interacted more strongly when both populations were on the membrane as compared to only one of the populations being membrane-bound [26]. These observations indicate the existence of an aggregating protein movement on the membrane. In the AC model, this is incorporated as a current term which is of the Cahn-Hilliard form [47].

Meacci and colleagues [13] tested the AC model in a one-dimensional geometry assuming that Min protein distributions are rotationally symmetric along the circumference of the cell. They were able to reproduce pole to pole Min oscillations and the dynamic Min patterns in filamentous cells. To learn more about the dynamical system and to make predictions for the real Min system, we studied patterns produced by simulations in different geometries [37].

In model cells with an over-sized radius, we found chiral surface waves that propagate around the bacterial circumference. They are superimposed onto the pole-to-pole oscillations characteristic for the Min proteins in *E. coli*. These solutions have a definite handedness and coexist with a solution of reversed sense of rotation. We also found solutions breaking rotational symmetry in the cooperative attachment (CA) model suggested by Huang *et al.* [35,49]. However, these solutions resulted from coupling between a standing longitudinal and a standing circumferential wave and are consequently non-chiral. Likewise, the CA model suggested by us in [12] predicts circumferential modes in cells with enlarged radius, see Section 4.3.2.

We also analyzed the AC model in an open geometry which mimics an *in vitro* setting including a flat membrane supported by a solid substrate exposed to a buffer containing MinD, MinE, and ATP. Here, we found the formation of interesting patterns and surface waves of bound proteins. By calculating the linear spreading velocity of a perturbation front moving into a homogeneous unstable state, we were able to characterize the dependence of the wave velocity on the system parameters.

We conclude that waves on the cytoplasmic membrane are a genuine feature of the AC mechanism. Similar patterns have been found in surface chemical reactions

in presence of attractive interactions between the adsorbed particles [50,51].

3.1 Circumferential modes of Min oscillations

Using the assumption that protein distributions are homogeneous within a cross section of an *E. coli* cell perpendicular to its long axis, one-dimensional simulations are appropriate to analyse the solutions of the dynamical system. The obtained solutions reproduce wild-type oscillations of *E. coli* as well as the pattern change observed in filamentous cells, where the oscillation pattern gains wave nodes [13]. Considering a more realistic cell shape and relaxing the assumption of radial symmetry of protein distributions, we simulated the Equations (2.2)-(2.5) in a bacterial geometry approximated by a cylindrical domain with hemispherical caps at the cylinder ends, see Figure 3.1a. In this geometry, solutions similar to the 1D-simulations are expected for sufficiently small cell radius. However, cells whose circumference is on the order of the wavelength of the oscillations or bigger are suspected to exhibit circumferential modulations of the concentration.

Numerical integration⁴ in the bacterial geometry with total length L and radius R of the model cell yields the following results: If the parameter k_1 in the Cahn-Hilliard current is sufficiently small, the stationary spatially uniform distribution of Min proteins is stable against small perturbations. As soon as k_1 exceeds a critical value, depending on parameter values, either stationary or oscillating spatially heterogeneous solutions are found. A subset of these solutions are invariant with respect to rotations around the system's long axis. They confirm the results of the one-dimensional analysis [13]. In addition, we find solutions breaking rotational invariance when the cell radius is increased beyond the wild type radius of *E. coli*. A typical example is presented in Figure 3.1a, where snapshots of the total MinD-distribution, $c_d + c_{de}$, are presented for several points in time. Pole-to-pole oscillations are clearly visible⁵. Superimposed on these are traveling waves on the membrane surface that circle around the cell's long axis. The existence of chiral waves is independent of the system length, as long as the system displays oscillations along the long axis.

In Figure 3.1b, we show for different times the position of the maximum of the total MinD distribution, $c_d + c_{de}$, on the circumference of the cell for a fixed position on the cell's long axis. It reveals that the rotation velocity of the traveling wave is not constant. The time needed for one full turn is in general incommensurate with the period of the pole-to-pole oscillations. Also, these distributions break chiral symmetry. The handedness of the solution is determined spontaneously by the initial condition. A solution mirror-symmetric to the one presented here coexists for the same parameter values. The distribution of membrane-bound MinE, c_{de} , is similar to that of MinD, see Figure 3.2.

Figure 3.3a presents a phase diagram of the system as a function of the dimen-

⁴In the numerical integrations of the AC model, we assume that the cytoplasmic distributions are homogeneous in a cross-section perpendicular to the system's long axis. This is appropriate for the diffusion constants of $D_D \approx 15\mu\text{m}^2/\text{s}$ and $D_E \approx 10\mu\text{m}^2/\text{s}$ that have been measured in *E. coli* [46].

⁵There are also stationary solutions that break rotational symmetry. They correspond to protein blobs forming on the membrane.

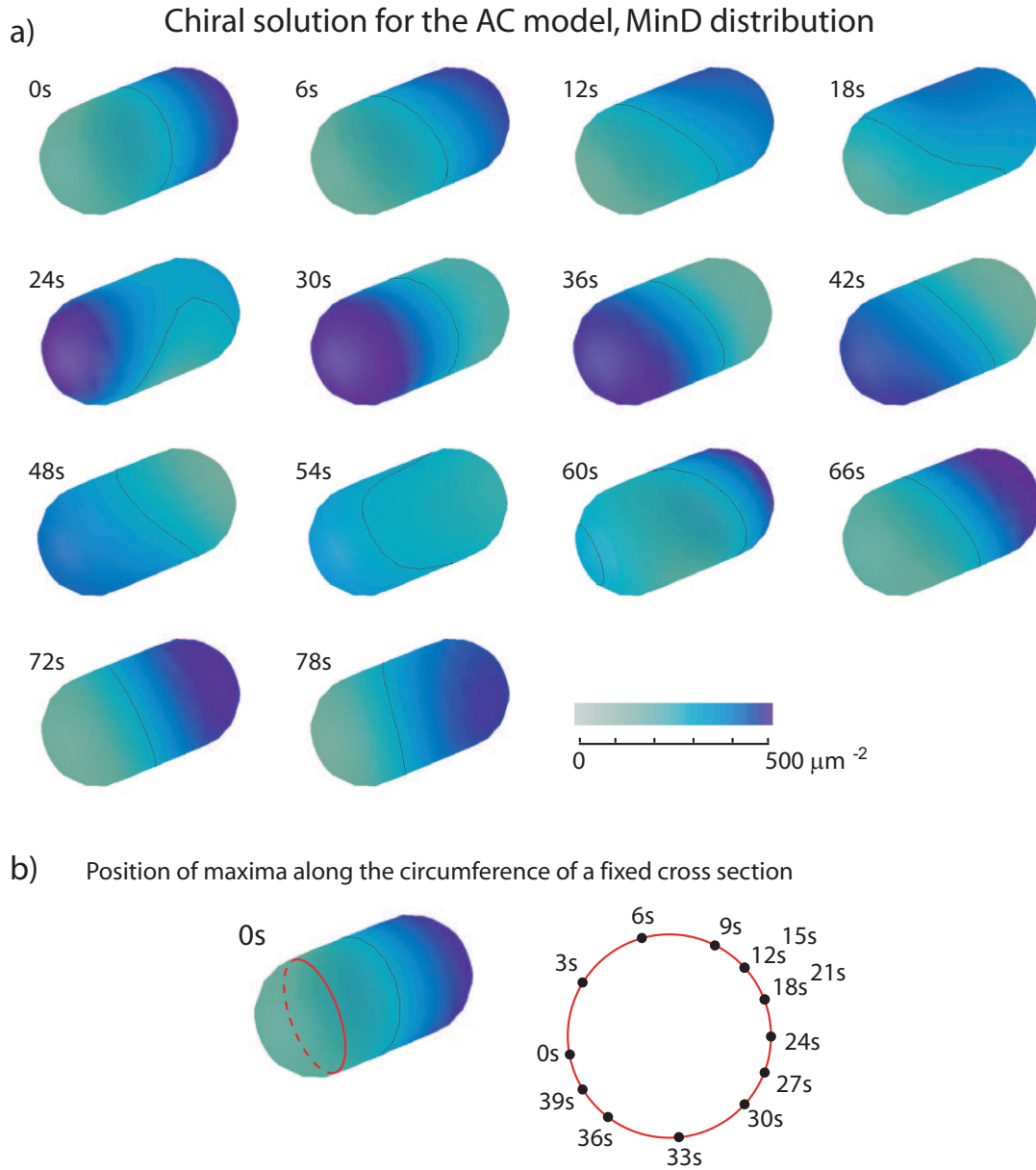


Figure 3.1: Chiral solution of the AC model defined by the dynamic equations (2.2)-(2.5). a) Concentration of membrane-bound MinD, $c_d + c_{de}$. The black line on the bacterium indicates an iso-concentration curve with $c_d + c_{de} = 300\mu\text{m}^{-2}$. In addition to the pole-to-pole oscillations, the distribution turns around the long axis. A solution with the opposite sense of rotation coexists with the one presented here. b) Location of the maximum MinD concentration on the red circle indicated on the left (distribution at $t = 0\text{s}$) for the solution presented in (a). The magnitude of this maximum of course changes in time. Parameters are $L = 3.2\mu\text{m}$, $R = 0.68\mu\text{m}$, $\mathcal{D} = 1300\mu\text{m}^{-3}$, $\mathcal{E} = 500\mu\text{m}^{-3}$, $\omega_D = 8.4 \times 10^{-5}\mu\text{m}^3/\text{s}$, $\omega_{de} = 0.04\text{s}^{-1}$, $\omega_E = 3.4 \times 10^{-4}\mu\text{m}^3/\text{s}$, $k_1 = 16.6 \cdot 10^{-6}\mu\text{m}^6/\text{s}$, $k_2 = 26.6 \cdot 10^{-7}\mu\text{m}^8/\text{s}$, $\bar{k}_1 = -k_1$, $\bar{k}_2 = 10^{-4}k_2$, $D_D = D_E = 15.4\mu\text{m}^2/\text{s}$, $D_d = 0.2\mu\text{m}^2/\text{s}$, $c_{\text{max}} = 500\mu\text{m}^{-2}$. \mathcal{D} and \mathcal{E} are the total numbers of MinD and MinE in the cell divided by the cell volume.

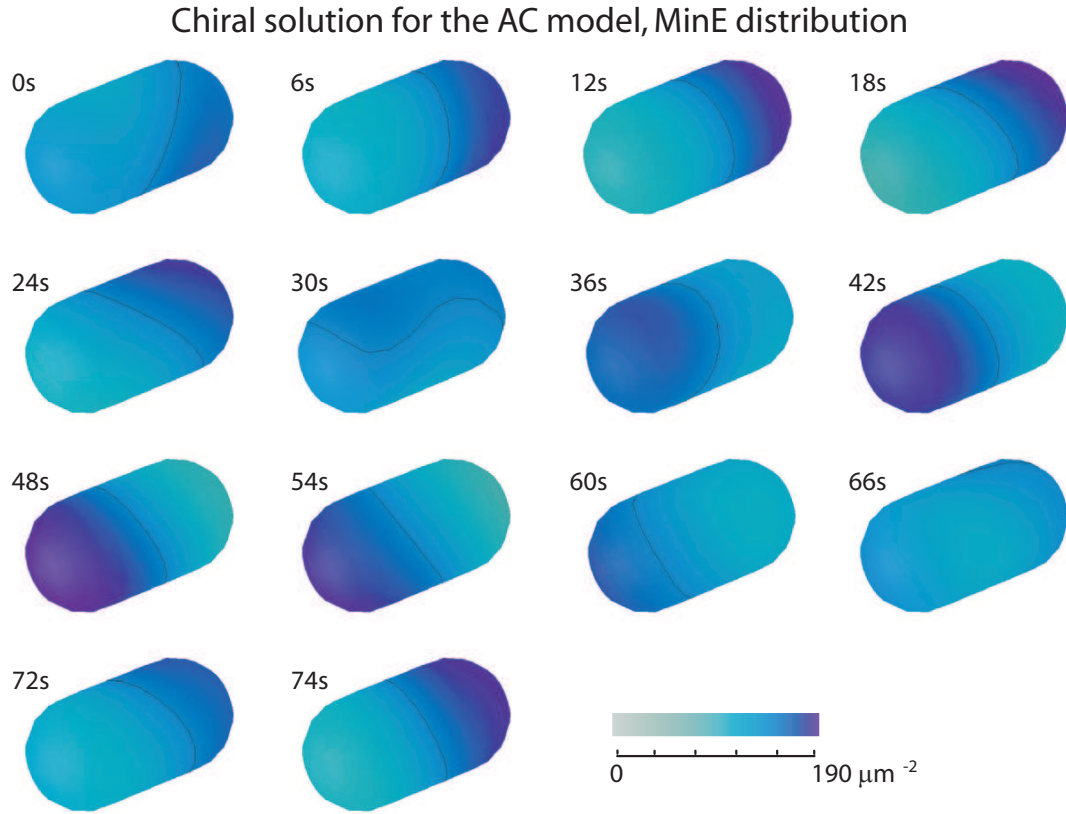


Figure 3.2: Distribution of MinE on the membrane corresponding to the solution presented in Figure 3.1. Here, the black line indicates an iso-concentration curve at $c_{de} = 150\mu\text{m}^{-2}$.

sionless interaction strength

$$K = c_{\max}^2 k_1^2 / (\omega_{de} k_2) \quad (3.1)$$

of the membrane-bound proteins and the dimensionless cell radius $\tilde{R} = R/r$, where r is the characteristic length defined above. We see that the homogenous protein distribution is stable as long as the interaction strength K is sufficiently small. Above a critical value, the distributions are heterogeneous. For the parameter values chosen for Figure 3.3, the distributions oscillate in time. These solutions are rotationally invariant for small radii \tilde{R} , but lose this invariance beyond a critical radius. The value of the critical radius depends on K . In addition, these solutions rotate around the bacterial long axis and spontaneously break chiral symmetry. Consequently, two solutions of different handedness and correspondingly of different senses of rotation coexist in this regime.

Linear stability analysis for a simplified geometry. In order to gain more insight into the phase diagram, we analyse the dynamic equations in the simpler geometry of a cylinder without hemispherical caps. At the cylinder ends, we choose reflecting boundary conditions. Furthermore, we assume the distributions c_D and c_E to be homogenous, which is a good approximation in view of the large cytoplasmic diffusion constants measured for MinD and MinE [46]. In that case, the dynamic equations for the cytoplasmic distributions (2.2) and

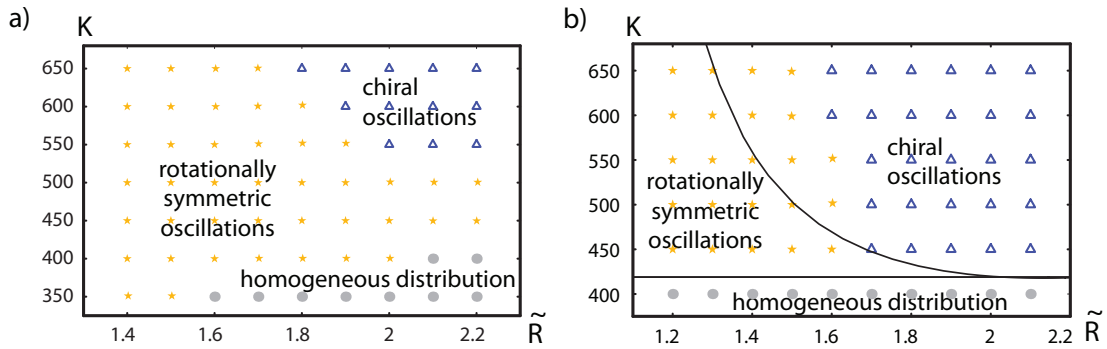


Figure 3.3: Phase diagrams. a) Numerically determined phase diagram for Eqs. (2.2)–(2.5) in a bacterial geometry as a function of the dimensionless radius $\tilde{R} = R/r$, where $r = \sqrt{k_2/k_1}$, and the dimensionless interaction strength $K = c_{\max}^2 k_1^2 / (\omega_{de} k_2)$. The distribution of Min proteins is either stationary and homogenous (grey dots) or oscillates, while being rotationally symmetric (yellow stars) or chiral (blue triangles). The oscillations of data point (2.1, 650) are shown in Figure 3.1, 3.2. b) Same as in (a) but in a cylindrical geometry. Black lines indicate boundaries of linear stability of lateral and circumferential modes and are good approximations for the phase boundaries, see text for further details. In (a) parameters are $(\omega_D c_{\max}) / (\omega_{de} r) = 2.6$, $(\omega_E c_{\max}) / (\omega_{de} r) = 10.5$, $D_D / (r^2 \omega_{de}) = D_E / (r^2 \omega_{de}) = 2400$, $D_d / (r^2 \omega_{de}) = 30$, $\bar{k}_1 = -k_1$, $\bar{k}_2 = 10^{-4} k_2$, $(\mathcal{D}r) / c_{\max} = 1.04$, $(\mathcal{E}r) / c_{\max} = 0.4$. The protein concentrations correspond to a MinD concentration of $900/\mu\text{m}$ and a MinE concentration of $350/\mu\text{m}$ in a cell of $3\mu\text{m}$ length and $1\mu\text{m}$ diameter. In (b) we chose $\omega_D C_D / \omega_{de} = 0.79$, $\omega_E C_E / \omega_{de} = 0.79$, where C_D and C_E are the constant cytoplasmic concentrations. The other parameters are as in (a). Note that in (b) cytoplasmic concentrations are kept constant for all simulations since they are fixed parameters of the system. However in (a), the total protein number was kept constant.

(2.3) decouple from the dynamic equations for the distributions of membrane-bound proteins (2.4) and (2.5), see [13]. The cytoplasmic concentrations evolve into a stationary state and we are left with the dynamics on the membrane. In spite of these simplifying assumptions, the corresponding phase diagram is qualitatively similar to the diagram obtained before, see Figure 3.3b. We now perform a linear stability analysis of the homogenous state. To this end, we decompose the distributions c_d and c_{de} in terms of the eigenfunctions $f_{n,m}(z, s, t) = \exp(\lambda_{n,m} t) \exp(ins/R) \cos(m\pi z/L)$, with $n, m = 0, 1, 2, \dots$, of the linearized time-evolution operator. Here, t is time, z with $0 \leq z \leq L$ the coordinate along the system's long axis and s the coordinate along the circumference. The parameters R and L denote the radius and the length of the cylinder coat, respectively. Finally, $\lambda_{n,m}$ is the growth exponent of the eigenfunction $f_{n,m}$. Note, that each $f_{n,m}$ respects the boundary conditions. The growth exponents $\lambda_{n,m}$ depend only on the absolute value k of the wave vector \mathbf{k} , which can take the discrete values $\mathbf{k}(n, m) = (n/R, m\pi/L)$. A typical dependence of the growth exponent's real and imaginary parts on k is illustrated in Figure 3.4a. If K is larger than a critical value, the real part of $\lambda(k)$ is positive in some interval. Examples of wave vector lattices for two different radii \tilde{R} together with the regions of $\lambda(k) > 0$ are presented in Figure 3.4b and c. As can be seen, different modes are unstable if the

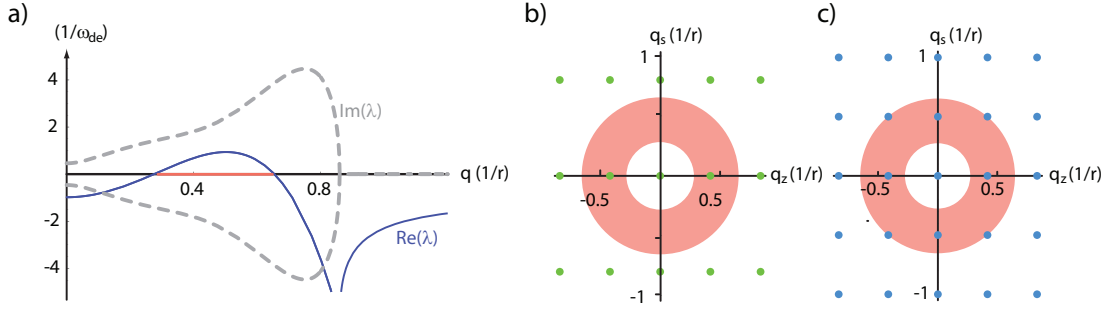


Figure 3.4: Growth exponents and wave vectors of Eqs. (2.2)-(2.5) in a cylindrical geometry and linearized with respect to the stationary homogenous distribution. a) The real and imaginary part of growth exponent λ as a function of the wave number k . The red line indicates the interval of unstable modes. Parameters are as in Figure 3.3b, with $K = c_{\max}^2 k_1^2 / (\omega_{de} k_2) = 500$ and $L = 7.5r$ ($r = (k_2/k_1)^{1/2}$). b, c) Grid of wave vectors corresponding to eigenmodes in the cylindrical geometry. The red annulus indicates regions of unstable wave vectors as obtained from the linear stability analysis. k_z : wave number of the lateral eigenmode, k_s : wave number of circumferential eigenmode. In (b) all circumferential modes are stable, in (c) there are unstable circumferential modes. Cylinder radii are $R = 1.25r$ (b) and $R = 2r$ (c).

system's radius is changed. In particular, for large radii, modes with $m \neq 0$ can get unstable indicating the presence of circumferential waves. Remarkably, for K close to its critical value, the boundary between oscillating states with and without rotational symmetry is well approximated by the stability boundary of modes with $m \neq 0$, see Figure 3.3b. The chiral waves thus result from coupling between the longitudinal ($n = 0, m \neq 0$) and circumferential modes ($n \neq 0, m = 0$).

Circumferential modes in CA models. Waves breaking rotational invariance can also be found in cooperative attachment (CA) models. We performed numerical calculations in the cell-like geometry using the dynamic equations proposed by Huang, Meir and Wingreen [49]. Similar to the model discussed above, distributions breaking rotational symmetry are found if a certain critical radius of the system is exceeded. Two solutions are presented in Figure 3.5. All solutions we observed result from a coupling between a standing longitudinal and a standing circumferential wave and are consequently non-chiral. For the CA model introduced in Section 2.3.3 and studied in Chapter 4.1, we find circumferential modes as standing and traveling waves.

3.1.1 *In vivo* study: Min proteins break rotational symmetry in *Escherichia coli*

We conjectured that the loss of rotational symmetry found in our numerical solutions is a mesoscopic effect of the MinD distribution in bacteria with an enlarged radius compared to wild-type *E.coli*. Our calculations show that circumferential modulations of the surface densities should become visible for bacterial circumferences which are of the same order as the wavelength of the longitudinal pattern. In order to test our hypothesis of the appearance of circumferential modes in

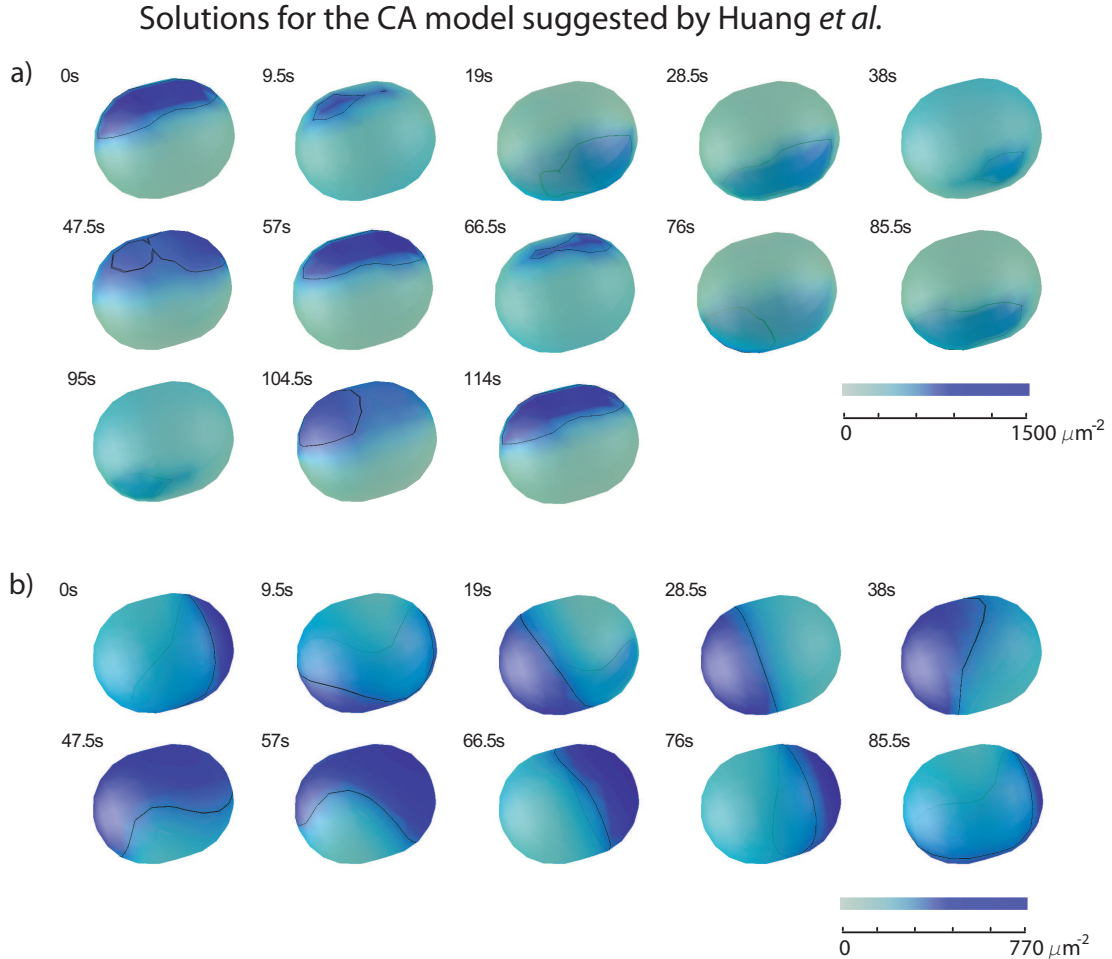


Figure 3.5: Solutions to the CA model suggested by Huang and colleagues [49] breaking rotational invariance. Shown are concentrations of membrane-bound MinD, $c_d + c_{de}$. Black lines indicate iso-concentration contours with $c_d + c_{de} = 740 \mu\text{m}^{-2}$ (a) and $c_d + c_{de} = 360 \mu\text{m}^{-2}$ (b). Superimposed onto the longitudinal pole-to-pole oscillations are standing waves along the circumference. In (a), where $c_{\max} = 2000 \mu\text{m}^{-2}$, the period of the longitudinal oscillation is twice that of the circumferential oscillation, in (b), where $c_{\max} = 1000 \mu\text{m}^{-2}$, they are equal. Other parameters are (same notation as in [49]) $\sigma_{de} = 0.4 \text{s}^{-1}$, $\sigma_D^{ADP \rightarrow ATP} = 1 \text{s}^{-1}$, $\sigma_D = 0.025 \mu\text{s}^{-1}$, $\sigma_{dD} = 0.0015 \mu\text{m}^3/\text{s}$, $\sigma_E = 0.3 \mu\text{m}^3/\text{s}$, $D_D = D_E = 2.5 \mu\text{m}^2/\text{s}$, $\mathcal{D} = 1300 \mu\text{m}^{-3}$, and $\mathcal{E} = 500 \mu\text{m}^{-3}$. The cell has a length of $2.5 \mu\text{m}$ and a radius of $1 \mu\text{m}$.

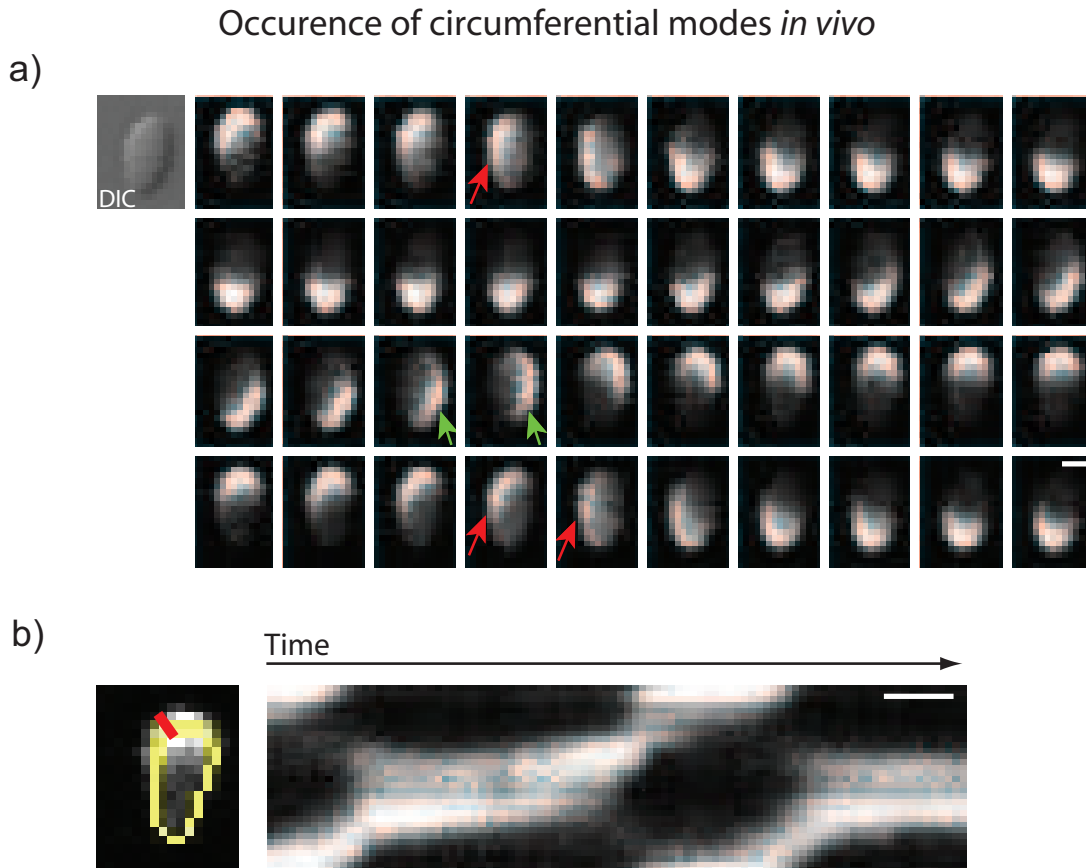


Figure 3.6: Min oscillations in an *E. coli* cell treated with the drug A22. Due to perturbation of the cytoskeleton, the cell enlarged in radius compared to a wild type cell. a) Time series of the distribution of GFP-MinD at time intervals of 6s. The red and the green arrow highlight frames where the fluorescence maximum is on the left or the right cell side, respectively. The scale bar shows $1\mu\text{m}$. b) Kymograph from a line scan along the circumference of the *E. coli* cell during the same time period as presented in a). The leftmost image shows the position of the line (yellow) along which the kymograph has been recorded. The red bar indicates the point where the beginning and the end of the line touch. It should be noted that fluorescence maxima appear in the kymograph at the left and the right border if the fluorescence maximum in the cell is at the top. The kymograph clearly shows the presence of diagonal stripes which indicates that the fluorescence rotates around the cell circumference for the chosen time window. The scale bar shows 30s.

cells with enlarged radius, we probed Min oscillations in *E. coli* cells which were treated with the drug A22 (S-(3,4-dichlorobenzyl)isothiourea). A22 was found to perturb the cytoskeletal structure MreB in bacteria [52,53] dissolving MreB helices which form at the inner side of the cytoplasmic membrane. MreB is involved in the deposition of new bacterial cell wall material [54,55]. In *E. coli*, MreB perturbation by A22 induces thickening of bacterial cells and a tendency towards spherical cell shapes.

In our experiments, we used *E. coli* cells from the strain JS964, containing the plasmid pAM238 which encodes MinE and GFP-MinD [19]. Cells were grown as described in Section 6.1.1 and, 2-3 hours before observation, $10\mu\text{g}/\text{ml}$ of A22 were added to the liquid culture. Recording MinD fluorescence over time, we found that Min oscillations in chubby cells indeed were no longer rotationally symmetric around the cell circumference. During switching of MinD from one cell pole to the other, the fluorescence intensity was frequently located to the left or the right cell half, see Figure 3.6. At times, Min oscillations looked like a rotation of the MinD maximum along the cell border (in a 2D projection) as it would be expected from simulation results as shown in Figure 3.5b and 4.11. Often, switching also occurred several times in series along the same cell side. In some instances, the MinD maximum did not show any preference for one cell side during switching. It is probable, that noise has an influence on the positioning of the MinD maximum during switching.

Of course it would be desirable to study the three-dimensional distribution of MinD in cells with an enlarged radius during switching of the fluorescence maximum. However the resolution of light microscopy with GFP is limited to about 200nm and the MinD distribution is dynamic during switching. Therefore, Z-stack recordings did not reveal new structural details of the rotationally asymmetric MinD distributions.

The experimental work by Shih, Le and Rothfield [30] reports helical polymer structures of membrane-bound MinD and MinE that also break rotational symmetry. Although the chiral waves share the same symmetry with the helical polymers, neither of the solutions presented here resembles this pattern. The observed structures can rather be expected as result of a particle-based model than of a coarse-grained description.

3.2 Surface waves in a flat, open geometry

We looked for an experimental situation that would allow to test the formation of surface waves of Min proteins in a controlled manner. Such a situation is given by an *in vitro* set up including a flat membrane immersed in a buffer solution that acts as a reservoir for MinD, MinE, and ATP. These considerations motivated the experiments presented in Section 4.1 and in [12]. We now discuss the dynamics of Min proteins in such a flat geometry according to the AC model. We choose two different initial conditions corresponding to different experimental settings. The first is more convenient from an experimental point of view, while the second allows for a better theoretical analysis.

First scenario. We start with a membrane to which no proteins are attached. Experimentally, this situation can be realized by initially preparing the buffer solution without ATP. In that case, MinD and therefore MinE do not bind to the

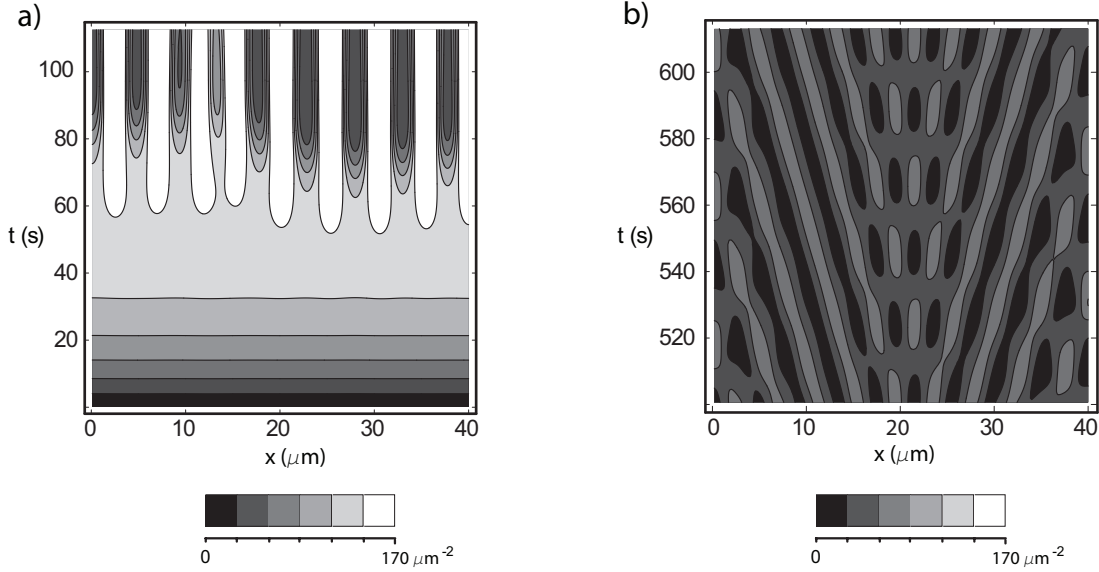


Figure 3.7: Time evolution of the MinD concentration in one space dimension integrating Eqs. (2.7) and (2.8). The initial condition was an essentially empty membrane with small fluctuations in the MinD concentration. The asymptotic state is either stationary (a) or oscillatory (b). In (b), the transient phase in the beginning is left out and only the asymptotic state is shown. Parameters are $\omega_{de} = 0.04\text{s}^{-1}$, $D_d = 0.2\mu\text{m}^2/\text{s}$, $\bar{k}_1 = \bar{k}_2 = 0$, $c_{\text{max}} = 477\mu\text{m}^{-2}$ with $\omega_D C_D = 0.014\text{s}^{-1}$, $\omega_E C_E = 0.024\text{s}^{-1}$, $k_1 = 11.2 \cdot 10^{-6}\mu\text{m}^6/\text{s}$, $k_2 = 18 \cdot 10^{-7}\mu\text{m}^8/\text{s}$ in (a) and $\omega_D C_D = 0.08\text{s}^{-1}$, $\omega_E C_E = 0.32\text{s}^{-1}$, $k_1 = 13.4 \cdot 10^{-5}\mu\text{m}^6/\text{s}$, $k_2 = 21.5 \cdot 10^{-6}\mu\text{m}^8/\text{s}$ in (b). At the boundaries the first and third spatial derivative of the concentrations vanish.

membrane [56]. At time $t = 0$, ATP is added and the Min proteins start to bind to the membrane, which is assumed to lie in the (x, y) -plane. We analyse this situation by solving the dynamic Eqs. (2.4) and (2.5) in the (x, y) -plane. As initial distribution, we use $c_d(x, y) = \epsilon c_{\text{max}} r(x, y)$ and $c_{de}(x, y) = 0$, where $\epsilon \ll 1$ and $r(x, y)$ is a field of random numbers between 0 and 1. This distribution is used to mimic an initially sparse irregular cover of the membrane by MinD. A homogenous initial distribution results in homogenous distributions for all time when evolved by Eqs. (2.4) and (2.5). For simplicity, we assume in the following that the solutions are invariant with respect to translations in the y -direction, leaving us with an essentially one-dimensional problem. The cytosolic concentrations are assumed to be fixed by the buffer, $c_D(x, t) = C_D$ and $c_E(x, t) = C_E$ for all x and t .

Asymptotically, the initial distribution evolved either into a homogenous or into a heterogeneous distribution. In the latter case, the distribution was either stationary or oscillatory. The case of a stationary solution is presented in Figure 3.7a, where a space-time plot of the MinD-concentration profile can be seen. As time increases, a spatially periodic pattern of high and low concentrations develops throughout the system. An oscillatory solution is shown in Figure 3.7b.

Second scenario. We start with a stationary homogenous distribution of MinD and MinD/MinE complexes to which we add a localized perturbation. The per-

turbations do not necessarily relax. Figure 3.8 shows cases where the perturbation grows and spreads. For the chosen parameter values, the propagating front leaves a striped (stationary or oscillatory) pattern in its wake. For an emerging stationary pattern, the propagation velocity v and the wavelength ℓ of the pattern as a function of the interaction strength k_1 is presented in the same figure.

Spreading velocity of localized perturbations. We have calculated the asymptotic linear spreading velocity of the perturbation propagating into the unstable state, see Ref. [57] for a review of this method. Essentially, the time evolution of the perturbation is analyzed by solving the dynamic equations that are linearized with respect to the unstable state. The asymptotic linear spreading velocity v^* is the average velocity of the level curve $x_\epsilon(t) = \max\{x | c_d(x, t) = C_d + \epsilon\}$ in the limit of large times⁶, where C_d is the concentration of the stationary state. The value of ϵ has to be chosen sufficiently small such that the propagating front is described well by the linearized dynamic equations. Details of our calculation are presented in Appendix B. We find, that the actual spreading velocity is well approximated by the linear spreading velocity v^* , see Figure 3.8d. Furthermore, our linear analysis gives a good approximation for the wavelength ℓ of the periodic pattern that is formed in the wake of the perturbation front, see Figure 3.8d. Generally, we find that the spreading velocity increases with the values of $K = c_{\max}^2 k_1^2 / (\omega_{de} k_2)$ and ω_{de} . On the contrary, the velocity decreases with an increasing diffusion constant D_d . Furthermore, the wavelength ℓ increases with K and decreases with the diffusion constant D_d .

Realization of displacement in emerging traveling waves. We have seen that the AC model can have traveling wave solutions in an open geometry in one space dimension. To understand how displacement of the concentration distribution is realized in this case, we simulated the result of a hypothetical photo-bleaching experiment for fluorescently labeled MinD which evolves according to the AC model dynamics. The simulation assumes a Gaussian bleaching profile with the center located close to a concentration maximum of the wave. The time evolution of the bleached well is shown in Figure 3.9 for two different choices of the parameters \bar{k}_1, \bar{k}_2 which characterize the interaction between MinD and MinDE. In Figure 3.9a, we show the concentration profile of MinD at subsequent times during bleaching for the case $\bar{k}_1 = \bar{k}_2 = 0$. The associated contour plot of MinD concentration is displayed below in Figure 3.9b. We see that in this case the bleached spot does not move but that a new concentration maximum builds up in front of the well by attachment of fluorescent proteins. This result is confirmed by the comparison of the effective current of the traveling wave vc_d , where v is the wave velocity and c_d is the MinD concentration, and the actual value of the MinD current \mathbf{j}_d in the dynamic equations (2.2)–(2.5), see Figure 3.9c. A substantial part of the wave displacement is achieved by iterative attachment and detachment of proteins and not by the membrane current \mathbf{j}_d . The analogous study has been performed for $\bar{k}_1 = -k_1, \bar{k}_2 = 10^{-4}k_2$. Here, we find that the bleached well smooths out fast but the dimmed MinD maximum moves then on with wave speed v , see Figure 3.9d,e. Thus the bleached region moves in space together with the wave. A comparison of the effective current of the traveling wave vc_d the MinD current \mathbf{j}_d shows that the wave displacement is mostly accomplished by the movement of MinD on the membrane given by \mathbf{j}_d .

⁶Note, that the velocity is the same if x_ϵ is defined with c_{de} instead of c_d .

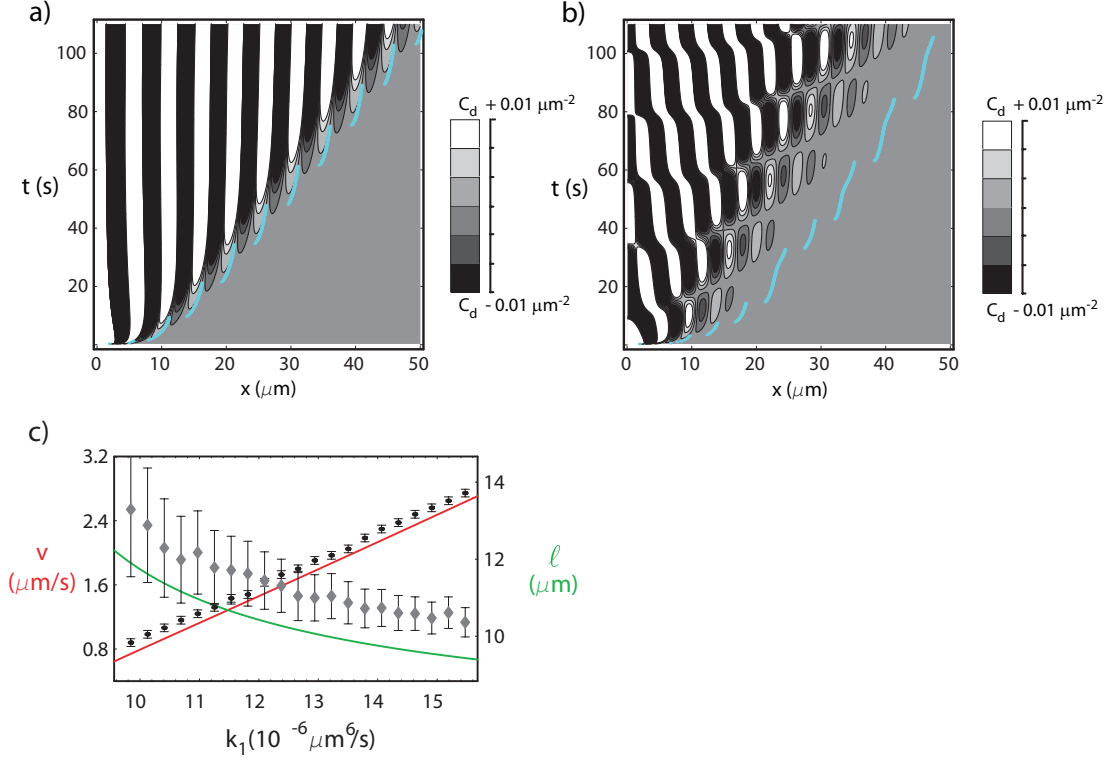


Figure 3.8: Analysis of front propagation after a small, localized perturbation. a, b) Time evolution of the concentration of bound MinD. Initial condition: homogenous distribution with localized perturbation in the interval $[0\mu\text{m}, 2\mu\text{m}]$ where the concentration was increased by 1%. The asymptotic state is either stationary (a) or oscillatory (b). Blue lines indicate the rightmost location with $c_d = (1 + 5 \times 10^{-4})C_d$, where $c_d = C_d$ is the concentration of membrane-bound MinD in the stationary state ($C_d = 143\mu\text{m}^{-2}$ (a) and $C_d = 37\mu\text{m}^{-2}$ (b)). c) Propagation speed and pattern wavelength as a function of k_1 . Numerically obtained data (black dots for speed, grey rhombi for wavelength, error bars indicate fitting errors) are compared to results from the linear analysis (red and green lines), see Sect. 3.2 and Appendix B. Deviations are due to approximations in our calculations and non-linear effects. The parameters are chosen for (a) as in Figure 3.7 (a), and for (b) as in Figure 3.7 (b) but with $k_1 = 10.7 \cdot 10^{-6} \mu\text{m}^6/\text{s}$, $k_2 = 17 \cdot 10^{-7} \mu\text{m}^8/\text{s}$ and $k_1 = 12.1 \cdot 10^{-5} \mu\text{m}^6/\text{s}$, $k_2 = 19.3 \cdot 10^{-6} \mu\text{m}^8/\text{s}$ for (a) and (b), respectively. The boundary conditions are such that the first and third spatial derivative of the concentrations vanish at $x = 0$ and $x = 80\mu\text{m}$.

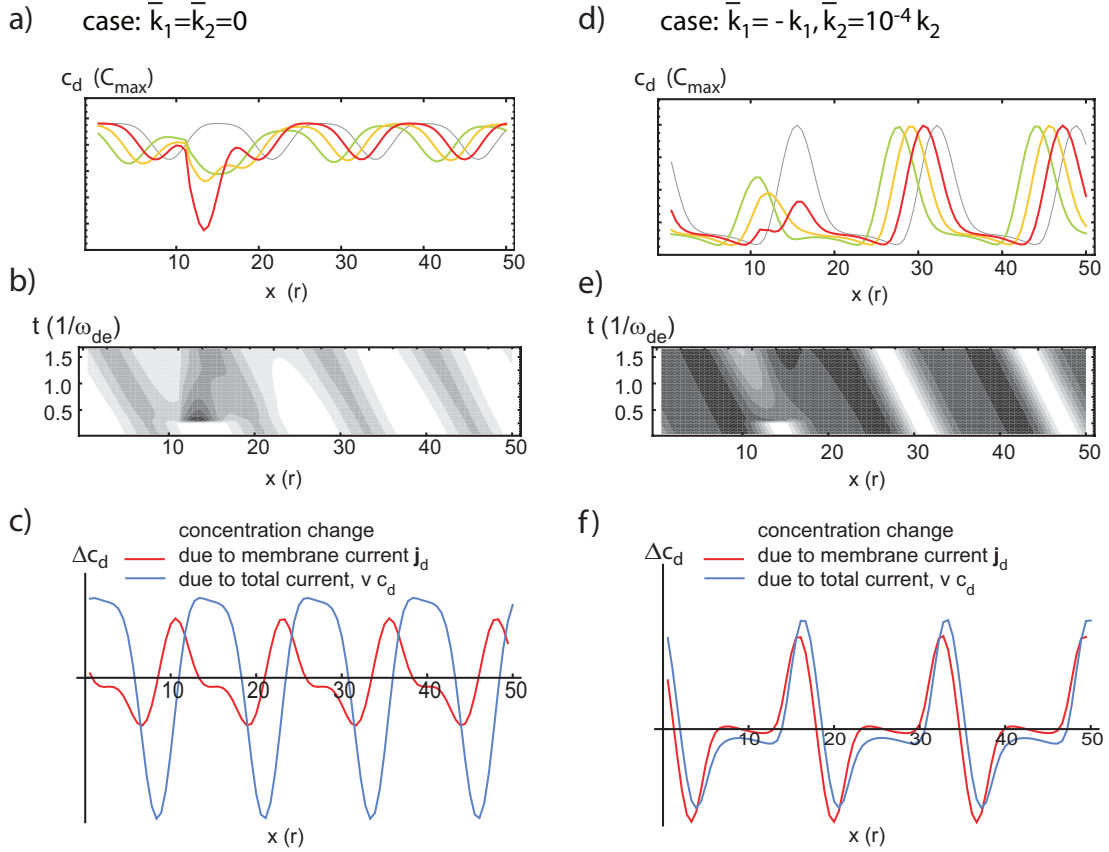


Figure 3.9: Analysis of displacement of MinD in a traveling wave which forms according to the AC model. a, b, c) and d, e, f) show results for the parameter choice $\bar{k}_1 = \bar{k}_2 = 0$ or $\bar{k}_1 = -k_1, \bar{k}_2 = 10^{-4}k_2$, respectively. a,d) Concentration profiles of MinD during bleaching for subsequent times. The time interval is $\Delta t = 0.5/\omega_{de}$. The grey curve shows the profile before bleaching, the red curve directly after bleaching. Subsequently, the yellow and then the green profile is taken. b,e) Associated contour plots to a) and d), respectively. c,f) Comparison of the effective current of the traveling wave $v c_d$, where v is the wave velocity and c_d is the MinD concentration, and the actual value of the MinD current on the membrane \mathbf{j}_d in the dynamic equations (2.2)–(2.5). The remaining parameters are chosen as $\omega_{DC_{\max}}/\omega_{de} = 1, \omega_{EC_{\max}}/\omega_{de} = 15, \mathcal{D}/c_{\max} = 0.45, \mathcal{E}/c_{\max} = 0.18$ for the left-hand side images and as $\omega_{DC_{\max}}/\omega_{de} = 20, \omega_{EC_{\max}}/\omega_{de} = 10, \mathcal{D}/c_{\max} = 1, \mathcal{E}/c_{\max} = 0.5$ for the right-hand side. r denotes the characteristic length scale $\sqrt{k_2/k_1}$. In both cases, we have $D_D/(r^2\omega_{de}) = D_E/(r^2\omega_{de}) = 2400, D_d/(r^2\omega_{de}) = 30$ and $K = 1.2K_c$ where K_c is the critical value for the current strength. This value is taken at the bifurcation.

3.3 Pattern formation in the open system: derivation of the amplitude equations for the AC model

Equations (2.7), (2.8) describe a dynamical system which is able to reproduce essential features of the observed Min oscillations. So far, solutions to this system have been mainly obtained by numerical integration. However, mere numeric integration must remain somewhat unsatisfactory since it only tells the properties of the system for a given parameter set. Although a full analytic solution of the partial differential equations is not feasible, we can still characterize the system's long time behavior in a certain range of parameters. Below a certain strength of the Cahn-Hilliard part of the current of MinD, the system has a homogeneous stationary solution, which is stable. Thus, heterogeneities in the system will smooth out over time. Exceeding a critical value of the current strength, the system undergoes a bifurcation and the stationary homogeneous state gets unstable. A linear stability analysis for deflections from the stationary state tells for which current strength the bifurcation occurs, and which Fourier mode becomes unstable first. Close to the bifurcation, the system shows a generic behavior and analytical tools such as the derivation of amplitude equations can give information about solutions. For simplicity, we will assume in the following that the system depends only on one space dimension. Additionally, we consider only the parameter range where oscillatory solutions occur beyond the bifurcation point.

General facts about amplitude equations for Hopf bifurcations at finite wavelength in 1D. For an oscillatory, spatially inhomogeneous bifurcation type (the eigenvalue of time evolution has a non-vanishing imaginary part, and the critical Fourier mode is not zero), the solutions of the linearized equations at the bifurcation point are

$$A_L \underline{v} e^{i(\omega_c t + k_c x)} + A_R \underline{v} e^{i(\omega_c t - k_c x)} + c.c.,$$

where k_c is the critical Fourier mode of the system, and $i\omega_c$ the critical frequency. The vector \underline{v} is the associated eigenvalue of the linear time evolution operator to the eigenvalue $i\omega_c$. A_L and A_R are the constant amplitudes for the two Fourier modes, which characterize left and right traveling wave contributions. Beyond the bifurcation, linear stability analysis is not sufficient anymore to characterize the behavior of the system, since it predicts exponential growth for the critical Fourier mode, which contradicts the assumption of this method that deflections from the stationary state are small. To get information about the behavior of the system slightly beyond the bifurcation point, there is another mathematical tool - the derivation of amplitude equations. Amplitude equations are most suitable for solutions in an open geometry, i.e. in an infinite system. They can provide information about the pattern which will form in the dynamical system in the weakly nonlinear regime. The idea of the method is to only slightly modify the solution of the linearized equations: The amplitudes of the different modes of the solution are assumed to vary with space and time, but on a longer time scale and a larger space scale than the solution of the linearized equations. This idea of scale separation in space and time permits a perturbation calculation using the defining equations of the system. In this approach, the space and time

derivatives, the bifurcation control parameter, and the solution are expanded in terms of an order parameter. This perturbation equation leads to a set of partial differential equations characterizing the time and space evolution of the amplitudes. For a more elaborate description of the derivation and features of amplitude equations see [10,58–60]. The amplitude equations have been found to be of a distinct shape for a given class of bifurcations. For the oscillatory, spatially inhomogeneous bifurcation type, one obtains in general

$$\begin{aligned}\partial_t A_L + s_0 \partial_x A_L &= \varepsilon A_L + (1 + ic_1) \partial_x^2 A_L - (1 - ic_3) |A_L|^2 A_L - g_1 (1 - ic_2) |A_R|^2 A_L \\ \partial_t A_R - s_0 \partial_x A_R &= \varepsilon A_R + (1 + ic_1) \partial_x^2 A_R - (1 - ic_3) |A_R|^2 A_R - g_1 (1 - ic_2) |A_L|^2 A_R.\end{aligned}\tag{3.2}$$

These equations are called generalized complex Ginzburg-Landau equation. The parameters $\varepsilon, g_1, s_0, c_1, c_2, c_3$ of the equations depend on the parameters of the original equations. The parameter s_0 is the group velocity, i.e. it is the derivative of the imaginary part of the time evolution eigenvalue at $k = k_c$, $\left. \frac{\partial \omega(k)}{\partial k} \right|_{k=k_c}$. If only a single wave is inherent in the system, i.e. either A_L or A_R vanish, the group velocity term can be eliminated by switching to a reference frame moving with velocity s_0 .

The Complex Ginzburg-Landau equation permits a number of simple solutions [10]. A traveling wave solution is

$$A_L = a \exp(-i\Omega t + \phi), \quad A_R = 0,\tag{3.3}$$

with $a^2 = \varepsilon, \Omega = -c_3 \varepsilon$, which is a left-traveling wave. Of course, there is a right-traveling wave analogue. Also, there are standing wave solutions

$$A_L = A_R = a \exp(-i\Omega t + \phi),\tag{3.4}$$

with $a^2 = \varepsilon / (1 + g_1), \Omega = -\varepsilon (c_3 + c_2 g_1) / (1 + g_1)$. The traveling wave solutions turns out to be stable if $g_1 > 1$. In this regime the standing wave solution is unstable. For $-1 < g_1 < 1$, the situation is reversed, i.e. the traveling wave solutions are unstable whereas the standing waves are stable. For $g_1 < -1$ neither of the solutions is stable and no saturation occurs. For an unbounded system (or for a system with periodic boundary conditions), g_1 can thus give a hint on whether traveling or standing waves are chosen within the system in the long time limit. An analysis of amplitude equations for two-dimensional space tells about the stability of a structure against perturbations.

Derivation of amplitude equations for the AC model. Below, we derive the amplitude equations for the system defined by equations (2.7), (2.8) for one-dimensional space. Which pattern emerges (traveling or standing waves) is determined by the effective binding parameters $w_E C_E, w_D C_D$ of MinD and MinE. We are starting out with the equations (2.7),(2.8). There are nine parameters in these equations which are $w_E C_E, w_D C_D, \omega_{de}, c_{\max}, k_1, k_2, \bar{k}_1, \bar{k}_2$ and D_d . Rescaling time, space and concentrations as $t \rightarrow t \omega_{de}, x \rightarrow x \sqrt{k_1/k_2}, c_{d/de} \rightarrow c_{d/de}/c_{\max}$,

we obtain the equations

$$\begin{aligned}\partial_t c_d &= \frac{w_D C_D}{\omega_{de}}(1 - c_d - c_{de}) - \frac{w_E C_E}{\omega_{de}}c_d + \frac{D_d k_1}{\omega_{de} k_2} \partial_x^2 c_d \\ &\quad - \frac{c_{\max}^2 k_1^2}{\omega_{de} k_2} \partial_x c_d (1 - c_d - c_{de}) (\partial_x c_d + \partial_x^3 c_d + \frac{\bar{k}_1}{k_1} \partial_x c_{de} + \frac{\bar{k}_2}{k_2} \partial_x^3 c_{de}) \\ \partial_t c_{de} &= -c_{de} + \frac{w_E C_E}{\omega_{de}} c_d.\end{aligned}\quad (3.5)$$

Thus, we obtain six dimensionless parameters $\tilde{\omega}_D = w_D C_D / \omega_{de}$, $\tilde{\omega}_E = w_E C_E / \omega_{de}$, $K = c_{\max}^2 k_1^2 / (\omega_{de} k_2)$, $\tilde{D}_d = D_d k_1 / (k_2 \omega_{de})$ and $\delta = \bar{k}_1 / k_1$, $\zeta = \bar{k}_2 k_1 / (k_2 \bar{k}_1)$. To avoid a notation too ornately, we will omit the tilde in the newly defined parameters. The equations then read

$$\begin{aligned}\partial_t c_d &= w_D(1 - c_d - c_{de}) - w_E c_d + D_d \partial_x^2 c_d \\ &\quad - K \partial_x c_d (1 - c_d - c_{de}) (\partial_x c_d + \partial_x^3 c_d + \delta (\partial_x c_{de} + \zeta \partial_x^3 c_{de})) \\ \partial_t c_{de} &= -c_{de} + w_E c_d.\end{aligned}\quad (3.6)$$

The homogeneous, stationary state of this system is

$$c_d^o = w_D / (w_D w_E + w_E + w_D), \quad c_{de}^o = w_E w_D / (w_D w_E + w_E + w_D).$$

Further analysis greatly simplifies if one assumes that $\bar{k}_1 = \bar{k}_2 = 0$, i.e. $\delta = 0$ and $\delta \zeta = 0$. Thus, we will present this special case first and then comment on the general case.

The case $\bar{k}_1 = \bar{k}_2 = 0$ (no interaction of MinD and MinDE on the membrane)

For a deflection $\mathbf{X} = (X_d, X_{de})$ from the homogeneous solution (c_d^o, c_{de}^o) , the following equation holds

$$\begin{aligned}\partial_t \begin{pmatrix} X_d \\ X_{de} \end{pmatrix} &= \begin{pmatrix} -(w_D + w_E) & -w_D \\ w_E & -1 \end{pmatrix} \begin{pmatrix} X_d \\ X_{de} \end{pmatrix} + \begin{pmatrix} 1 \\ 0 \end{pmatrix} D_d \partial_x^2 X_d \\ &\quad - \begin{pmatrix} 1 \\ 0 \end{pmatrix} K \partial_x (c_d^o + X_d) (1 - c_d^o - c_{de}^o - X_d - X_{de}) (\partial_x X_d + \partial_x^3 X_d) \\ &= \mathbf{M} \begin{pmatrix} X_d \\ X_{de} \end{pmatrix} \\ &\quad + \begin{pmatrix} 1 \\ 0 \end{pmatrix} (D \partial_x^2 X_d - K' \partial_x \mathcal{F}(X_d, X_{de}) (\partial_x X_d + \partial_x^3 X_d)),\end{aligned}\quad (3.7)$$

where $\mathcal{F} = 1 + \alpha X_d + \beta X_{de} - \gamma X_d (X_d + X_{de})$, $K' = K c_d^o (1 - c_d^o - c_{de}^o)$, and

$$\begin{aligned}\alpha &= (1 - 2c_d^o - c_{de}^o) / c_d^o (1 - c_d^o - c_{de}^o) \\ \beta &= -1 / (1 - c_d^o - c_{de}^o) \\ \gamma &= 1 / c_d^o (1 - c_d^o - c_{de}^o).\end{aligned}$$

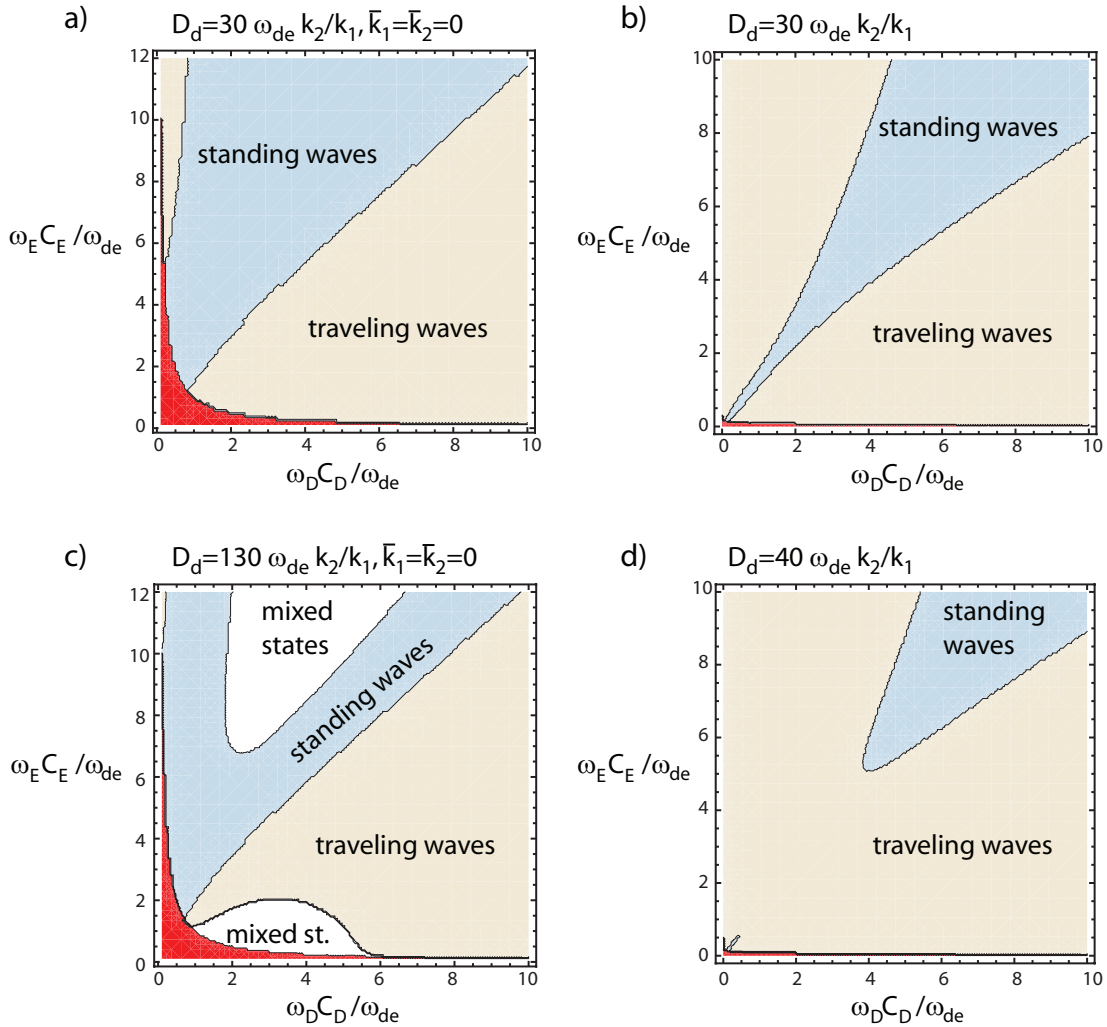


Figure 3.10: Stability regimes of traveling and standing waves for the dynamical system given by (3.5) for one space dimension in the weakly nonlinear regime. This system corresponds to the AC model of Min oscillations in the limit of large cytoplasmic diffusion. The blue areas symbolise $g_1 > 1$, the beige areas stand for $-1 < g_1 < 1$ and the white regions indicate $g_1 < -1$. The red parameter regions belong to non-oscillatory bifurcation behavior. a) The case of $\bar{k}_1 = \bar{k}_2 = 0$ with $D_d = 30 \cdot \omega_{de} k_2/k_1$. b) The case of $\bar{k}_1 = -k_1, \bar{k}_2 = 10^{-4} k_2$ with $D_d = 30 \cdot \omega_{de} k_2/k_1$. c) The case of $\bar{k}_1 = \bar{k}_2 = 0$ with $D_d = 130 \cdot \omega_{de} k_2/k_1$. d) The case of $\bar{k}_1 = -k_1, \bar{k}_2 = 10^{-4} k_2$ with $D_d = 40 \cdot \omega_{de} k_2/k_1$.

\mathbf{M} is the matrix containing the reaction rates. Derivation of the amplitude equations involves now expansions

$$\begin{aligned}\mathbf{X} &= \epsilon \mathbf{X}_1 + \epsilon^2 \mathbf{X}_2 + \epsilon^3 \mathbf{X}_3 + \dots, \\ \partial_x &= \partial_{x_0} + \epsilon \partial_{x_1} + \epsilon^2 \partial_{x_2} + \epsilon^3 \partial_{x_3} + \dots, \\ \partial_t &= \partial_{t_0} + \epsilon \partial_{t_1} + \epsilon^2 \partial_{t_2} + \epsilon^3 \partial_{t_3} + \dots, \\ K' &= K'_c + \epsilon K'_1 + \epsilon^2 K'_2 + \dots\end{aligned}\quad (3.8)$$

The variable ϵ denotes here the order parameter of the perturbation calculation. K' is also expanded since it is the control parameter of the bifurcation.

First order equation. Plugging these expansions into Equation (3.7), the terms to first order in ϵ give the relation

$$\begin{aligned}\partial_{t_0} \mathbf{X}_1 &= \mathbf{M} \mathbf{X}_1 + \begin{pmatrix} 1 \\ 0 \end{pmatrix} D_d \partial_{x_0}^2 X_{d,1} - \begin{pmatrix} 1 \\ 0 \end{pmatrix} K'_c (\partial_{x_0}^2 X_{d,1} + \partial_{x_0}^4 X_{d,1}) \\ &=: \mathcal{L} \mathbf{X}_1,\end{aligned}$$

where \mathcal{L} denotes the linear operator acting on \mathbf{X}_1 on the r.h.s. in the top line. Switching to Fourier space, we obtain

$$\begin{aligned}\partial_{t_0} \tilde{\mathbf{X}}_1 &= \mathbf{M} \tilde{\mathbf{X}}_1 - \begin{pmatrix} 1 \\ 0 \end{pmatrix} D_d k^2 \tilde{X}_{d,1} + \begin{pmatrix} 1 \\ 0 \end{pmatrix} K'_c (k^2 \tilde{X}_{d,1} - k^4 \tilde{X}_{d,1}) \\ &= \begin{pmatrix} (-w_D - w_E - D_d k^2 - K'_c (k^4 - k^2)) & -w_D \\ w_E & -1 \end{pmatrix} \tilde{\mathbf{X}}_1,\end{aligned}$$

where $\tilde{\mathbf{X}}_1$ is the Fourier transform of \mathbf{X}_1 . As eigenvalues of the time evolution operator, we obtain

$$\begin{aligned}\lambda_{1/2} &= -\frac{(1 + w_D + w_E + k^2 D_d + K'_c (k^4 - k^2))}{2} \\ &\quad \pm \sqrt{\frac{(w_D + w_E + k^2 D_d + K'_c (k^4 - k^2) - 1)^2}{4} - w_D w_E}.\end{aligned}$$

At the bifurcation point, i.e. for $K' = K'_c$, the real part of $\lambda_{1/2}$ is maximal at the critical wave vector k_c with the maximum being equal to zero. Assuming that the root term will be imaginary, the maximality requirement reads $(D_d - K'_c) + 2K'_c k_c^2 = 0$. Thus

$$k_c = \sqrt{\frac{1}{2} \left(1 - \frac{D_d}{K'_c}\right)} \quad (3.9)$$

is the critical Fourier mode. Inserting k_c into the eigenvalue equation, we get as condition of vanishing real part of the eigenvalue

$$0 = (1 + w_D + w_E + k_c^2 (D_d - K'_c))/2,$$

and therefore

$$K'_c = (D_d + 2(1 + w_D + w_E)) \pm \sqrt{(D_d + 2(1 + w_D + w_E))^2 - D_d^2}. \quad (3.10)$$

The sign in front of the root term has to be + since otherwise k_c becomes imaginary. For ω_c , the imaginary part of $\lambda_1(k_c)|_{K'=K'_c}$, we obtain

$$\omega_c = \sqrt{w_D w_E - 1}. \quad (3.11)$$

Hence, the condition that the system switches to an oscillatory state beyond the bifurcation means in this case that $w_D w_E$ has to be greater than 1. If this condition is not met, the type of bifurcation changes and the above calculation of the critical point is not valid anymore.

The matrix of the linear operator \mathcal{L} in Fourier space takes the following form for $k = k_c$

$$\begin{pmatrix} 1 & -w_D \\ w_E & -1 \end{pmatrix}.$$

The eigenvalues of this operator are $\pm i\omega_c$. Recall that the eigenvalues of all other wave vectors have a negative real part. The eigenvector associated to the eigenvalue $i\omega_c$ is

$$\underline{v} = (1 + i\omega_c, w_E). \quad (3.12)$$

The null space of the adjoint to $i\omega_c - \mathcal{L}$, i.e. $-i\omega_c - \mathcal{L}^T$, is spanned by the vector $\underline{w} = (-(1 - i\omega_c), w_D)$. Thus, the vector \underline{w} spans the orthogonal complement of the image of the operator $(i\omega_c - \mathcal{L})$. We will denote the components of the vectors \underline{v} and \underline{w} as (v_d, v_{de}) and (w_d, w_{de}) .

The solution of the linear equation gives the following ansatz for \mathbf{X}_1

$$\mathbf{X}_1 = A_L \underline{v} e^{i(\omega_c t_0 + k_c x_0)} + A_R \underline{w} e^{i(\omega_c t_0 - k_c x_0)} + c.c.,$$

where A_L, A_R depend on higher order time and space variables.

The equations of second and third order in the perturbation parameter ϵ put further constraints on the values of A_L and A_R . The derivation of these equations, and the extraction of their solvability conditions is contained in Appendix C.1. As amplitude equation for A_L , one gets in the end

$$\begin{aligned} \partial_t A_L &= -\frac{1}{2} \left(1 - \frac{i}{\omega_c}\right) \Delta K' (k_c^4 - k_c^2) A_L + 2 \left(1 - \frac{i}{\omega_c}\right) K'_c k_c^2 \partial_x^2 A_L \\ &\quad + \frac{1}{2i\omega_c} (a_{LL} + b_{LL} + c_{LL}) A_L |A_L|^2 \\ &\quad + \frac{1}{2i\omega_c} (a_{RL} + b_{RL} + c_{RL}) A_L |A_R|^2, \end{aligned} \quad (3.13)$$

where $\Delta K' = K' - K'_c$. The coefficients $a_{LL}, a_{RL}, b_{LL}, b_{RL}, c_{LL}, c_{RL}$ are

$$\begin{aligned} a_{LL} &= 4k_c^4 (1 - 5k_c^2 + 4k_c^4) K_c'^2 v_d |\alpha v_d + \beta v_{de}|^2 U_{2,2,d}, \\ a_{RL} &= 4k_c^4 (1 - 5k_c^2 + 4k_c^4) K_c'^2 (\alpha v_d + \beta v_{de}) U_{0,2,d} (v_d (2\alpha v_d^* + \beta v_{de}^*) + \beta v_{de} v_d^*), \\ b_{LL} &= -2k_c^4 (-1 + k_c^2)^2 K_c'^2 v_d (\alpha v_d + \beta v_{de}) (\alpha U_{2,2,d} + \beta U_{2,2,de}) v_d^*, \\ b_{RL} &= -2k_c^4 (-1 + k_c^2)^2 K_c'^2 v_d (\alpha U_{0,2,d} + \beta U_{0,2,de}) (\beta v_{de} v_d^* + v_d (2\alpha v_d^* + \beta v_{de}^*)), \\ c_{LL} &= \gamma k_c^2 (-1 + k_c^2) K_c' v_d^2 (v_d^* + v_{de}^*), \\ c_{RL} &= 2\gamma k_c^2 (-1 + k_c^2) K_c' v_d (v_d + v_{de}) v_d^*. \end{aligned}$$

The vectors $\mathbf{U}_{2,2}, \mathbf{U}_{0,2}$ are defined in (C.2). The equation for A_R is obtained by exchanging A_L, A_R in the above equation. Note that the group velocity vanishes. Rescaling of A_L, A_R , time and space yields equations of the form of (3.2). The mode coupling coefficient g_1 of the associated Ginzburg Landau equation is given by

$$g_1 = \frac{\text{Im}(a_{RL} + b_{RL} + c_{RL})}{\text{Im}(a_{LL} + b_{LL} + c_{LL})}. \quad (3.14)$$

For fixed membrane diffusion D_d , the rates w_D, w_E tune the value of g_1 . For values of g_1 greater than 1, traveling waves are expected as asymptotic pattern in the system, whereas standing waves will be preferred for the regime of $-1 < g_1 < 1$. The stability regimes in dependence of these parameters is indicated in Figure 3.10a and b. The prediction of the stability regimes by the value of g_1 nicely agrees with results of simulations.

The general case

For the more general case of non-vanishing parameters \bar{k}_1, \bar{k}_2 , the calculation of the amplitude equation is more involved, especially since the group velocity s_0 of the amplitudes is not zero. Therefore, we will restrict the calculation here to the parameter g_1 of the amplitude equations, which conducts the stability of traveling and standing waves in the open system. Like in the preceding section, we start out from Equations (3.6). For the deflections from the homogeneous state, we get the following relation

$$\begin{aligned} \partial_t \begin{pmatrix} X_d \\ X_{de} \end{pmatrix} &= \mathbf{M} \begin{pmatrix} X_d \\ X_{de} \end{pmatrix} + \begin{pmatrix} 1 \\ 0 \end{pmatrix} D \partial_x^2 X_d \\ &\quad - \begin{pmatrix} 1 \\ 0 \end{pmatrix} K' \partial_x \mathcal{F}(X_d, X_{de}) (\partial_x X_d + \partial_x^3 X_d + \delta (\partial_x X_{de} + \zeta \partial_x^3 X_{de})) \end{aligned} \quad (3.15)$$

with parameters as in the preceding sections.

The first order equation is thus

$$\begin{aligned} \partial_{t_0} \mathbf{X}_1 &= \mathbf{M} \mathbf{X}_1 + \begin{pmatrix} 1 \\ 0 \end{pmatrix} [D_d \partial_{x_0}^2 X_{d,1} - K'_c (\partial_{x_0}^2 X_{d,1} + \partial_{x_0}^4 X_{d,1} + \delta (\partial_{x_0}^2 X_{de} + \zeta \partial_{x_0}^4 X_{de}))] \\ &=: \mathcal{L} \mathbf{X}_1. \end{aligned}$$

In Fourier space, the linear operator \mathcal{L} reads

$$\partial_{t_0} \mathbf{X}_1 = \begin{pmatrix} -w_D - w_E - D_d k_c^2 - K'_c (k_c^4 - k_c^2) & -w_D - K'_c \delta (\zeta k_c^4 - k_c^2) \\ w_E & -1 \end{pmatrix} \mathbf{X}_1.$$

As in the case of $\bar{k}_1 = \bar{k}_2 = 0$, we assume that the root term in the expression for the eigenvalues is imaginary at the bifurcation. Thus, we obtain the same value for K'_c and k_c . The critical frequency ω_c is now

$$\omega_c = \sqrt{w_D w_E + K'_c \delta (\zeta k_c^4 - k_c^2) w_E - 1}. \quad (3.16)$$

The eigenvector associated to $i\omega_c$ is $\underline{v} = (1 + i\omega_c, w_E)$. The Null space of the

adjoint operator to $i\omega_c - \mathcal{L}$ is again spanned by the vector $\underline{w} = (-(1 - i\omega_c), w_D)$. The group velocity of the system is given by

$$s_0 = K'_c \frac{k_c}{\omega_c} \delta(\zeta 2k_c^2 - 1) w_E. \quad (3.17)$$

For the value of g_1 , again, equation (3.14) holds substituting for the coefficients $a_{LL}, a_{RL}, b_{LL}, b_{RL}, c_{LL}, c_{RL}$ now the terms given in Equations (C.9). A detailed derivation of s_1 and g_1 is given in Appendix C.2. The value of g_1 in dependence of the effective membrane-binding rates w_D, w_E of the proteins MinD and MinE is shown in Figure 3.10b. Numerical simulations confirm the obtained results.

3.3.1 Discussion of stability regimes

In the preceding section, we derived a general expression for the mode coupling coefficient g_1 of the Ginzburg Landau equation associated to the dynamic system (3.5) which corresponds to the AC model of Min oscillations in the case of large cytoplasmic diffusion. The coefficient g_1 determines the stability regimes of traveling and standing waves in one space dimension close to the bifurcation.

To discuss the stability regimes in dependence of the effective attachment rates $\tilde{\omega}_D = \omega_D C_D / \omega_{de}$ and $\tilde{\omega}_E = \omega_E C_E / \omega_{de}$, we consider fixed membrane diffusion and two cases of fixed \bar{k}_1, \bar{k}_2 .

For the choice $D_d = 30 \cdot \omega_{de} k_2 / k_1$ and either $\bar{k}_1 = \bar{k}_2 = 0$ or $\bar{k}_1 = -k_1, \bar{k}_2 = 10^{-4} k_2$, there are two stability regimes favoring traveling or standing waves of the concentration fields, see Figure 3.10a and b. This result suggests that according to the AC model it should be possible to switch between the two stability regimes by varying separately the concentrations of MinD and MinE in the system, thereby moving in the parameter plane of the parameters $\tilde{\omega}_D$ and $\tilde{\omega}_E$. Of course, also a direct change of the parameters ω_D and ω_E , e.g. by mutations of the proteins or alteration of the lipid composition, could change the effective binding rates and thus the stability regime.

The choice of the membrane diffusion constant D_d also has an influence on the favored pattern. For $\bar{k}_1 = -k_1, \bar{k}_2 = 10^{-4} k_2$, an increase of D_d leads to a reduction of the standing wave tongue, compare Figure 3.10b and d. For $\bar{k}_1 = \bar{k}_2 = 0$ and $\bar{k}_1 = -k_1, \bar{k}_2 = 10^{-4} k_2$, a strong increase of D_d to $100 \cdot \omega_{de} k_2 / k_1$ and more adds a regime where g_1 is smaller than -1 , i.e. neither standing nor traveling waves are stable but mixed states will emerge. For $\bar{k}_1 = \bar{k}_2 = 0$, these regimes become quite extensive, see Figure 3.10c.

Note that the predictions obtained from the amplitude equations are only valid for systems which are sufficiently large to neglect boundary effects. Therefore, the results are rather applicable to extended geometries as used in *in vitro* experiments than to the patterns found in confined cell-like geometries.

3.3.2 Patterns in two space dimensions

We wanted to test whether the AC model produces stable planar traveling wave (SPTW) patterns in two space dimensions. This is of interest as it is the predominant pattern produced by Min proteins *in vitro*, see Section 4.1. Apparently, SPTW patterns are not expected in two space dimensions for parameter regimes

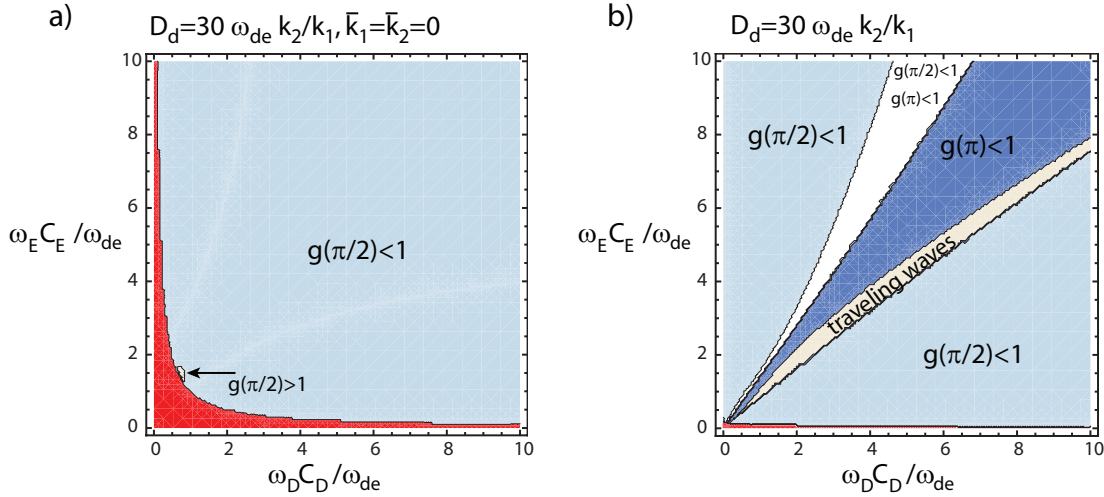


Figure 3.11: Phase diagrams indicating the stability of planar traveling waves for the dynamical system given by (3.5) in two space dimensions in the weakly nonlinear regime. This system corresponds to the AC model of Min oscillations in the limit of large cytoplasmic diffusion. a) The case of $\bar{k}_1 = \bar{k}_2 = 0$ with $D_d = 30 \omega_{de} k_2/k_1$. The blue area indicates the region where the coupling coefficient $g(\pi/2)$ is smaller than one. Therefore, planar traveling waves are unstable against perturbations including traveling waves propagating in a space direction enclosing an angle of 90° with the original propagation direction. The tiny beige area shows the region in which $g(\pi/2) > 1$. b) The case of $\bar{k}_1 = -k_1, \bar{k}_2 = 10^{-4} k_2$ with $D_d = 30 \omega_{de} k_2/k_1$. The blue, the light blue and the white area indicate regions where $g(\pi/2)$ or $g(\pi)$ or both are smaller than one. Thus, planar traveling waves are unstable against perturbations including traveling waves propagating in a space direction at an angle of 90° or/and 180° . The beige area shows the region in which $g(\pi/2) > 1$ and $g(\pi) > 1$. Red parameter regions belong to non-oscillatory bifurcation behavior.

where traveling waves are unstable in one space dimension. However, parameter regimes with stable traveling waves in one space dimension do not need to remain stable in two space dimension: Amplitudes of modes with wave vectors which point in different space directions (with common modulus k_c) can couple and amplify. Lets assume that our solution is of the form

$$A_L \underline{v} e^{i(\omega_c t + \mathbf{k}_1 \mathbf{r})} + B_L \underline{v} e^{i(\omega_c t + \mathbf{k}_2 \mathbf{r})} + c.c.,$$

where \mathbf{k}_1 and \mathbf{k}_2 have the common modulus k_c and that $\mathbf{k}_1 \cdot \mathbf{k}_2 = \cos(\theta)$. That means, we have planar traveling waves in two space directions which enclose the arbitrary angle θ . If we leave out spatial variations of the amplitudes, the dynamic equation of A_L defined in 3.2 is replaced by the equation

$$\partial_t A_L = \varepsilon A_L - (1 - ic_3) |A_L|^2 A_L + g(\theta) (1 - ic(\theta)) |B_L|^2 A_L,$$

with an analogous equation defining $\partial_t B_L$. The value of the coupling coefficient $g(\theta)$ determines if planar traveling wave solutions with for instance $A_L \neq 0, B_L = 0$ are stable against perturbations with $B_L \neq 0$ [10]. This is the case,

if $g(\theta) > 1$ for all $\theta \in [0, 2\pi]$. We have calculated the coupling coefficient $g(\theta)$ for different parameter values of the AC model in the same way as we derived the coupling coefficient g_1 in the preceding section. The results are summarized in Figure 3.11. We find that SPTW patterns in two space dimensions are not generic for the parameter regimes which we considered.

Chapter 4

In vitro patterns of Min-proteins on a planar membrane

The Min system is a strong candidate for a self-organizing system in cell biology. Several computational models were suggested to explain the Min system, see Section 2.3.1. Most of them reproduce the oscillations in the cell without additional spatial markers that guide the Min proteins. Oscillations form spontaneously from a homogeneous protein distribution by the amplification of fluctuations in the system. The self-organization of Min proteins however need not be restricted to the cell geometry. Computational models of the Min system predict pattern formation also in *in vitro* situations on flat membranes, see Section 3.2.

4.1 Min proteins organize into surface waves *in vitro*

In vitro experiments⁷ have been carried out by our collaborator Martin Loose [12]: A supported lipid bilayer was immersed in a buffer containing fluorescently labeled MinD (Bodipy-FL), MinE (Alexa647) and ATP. After a transient phase of about one hour, a protein pattern formed and persisted for several hours (see Figure 4.1). Spatially periodic bands of proteins formed, separated by concentration troughs devoid of proteins. These bands formed regions of ordered wave trains, spirals and double spirals (see Figure 4.2). The protein bands moved with constant velocity of about $0.7\mu\text{m/s}$ dependent on the MinE concentration in the system. A characteristic concentration profile of proteins along the propagation direction (see Figure 4.3) could be observed: From the leading part of the band, the MinD concentration increased, reached the maximum behind the middle and fell off again. The MinE concentration monotonously grew towards the rear of the band, reached its maximum there and then dropped sharply to zero. The maximum of the MinE concentration followed behind the maximum of the MinD concentration forming a sharp line at the trailing edge of the protein band. This arrangement is similar to the situation in the cell where the MinE ring forms at the rim of the MinD maximum and travels towards the pole when the MinD maximum dissolves. Thus, *in vitro* as well as *in vivo*, MinE maxima eat up MinD maxima in a pac-man like manner. The MinE concentration in the system influenced the wavelength of the pattern as well as the speed of the waves. Increasing the concentration from 0.5 to $5\mu\text{M}$ the average propagation velocity increased as indicated in Figure 4.7a. The wavelength decreased as shown in Figure 4.7b. Below a MinE concentration of $0.2\mu\text{M}$ waves formed erratically but the system did not evolve to a well-defined state. For MinD concentrations higher than $1.25\mu\text{M}$ and MinE concentrations lower than $2\mu\text{M}$, stationary patterns of proteins formed

⁷For further experimental details, see [12] and the supporting online material.

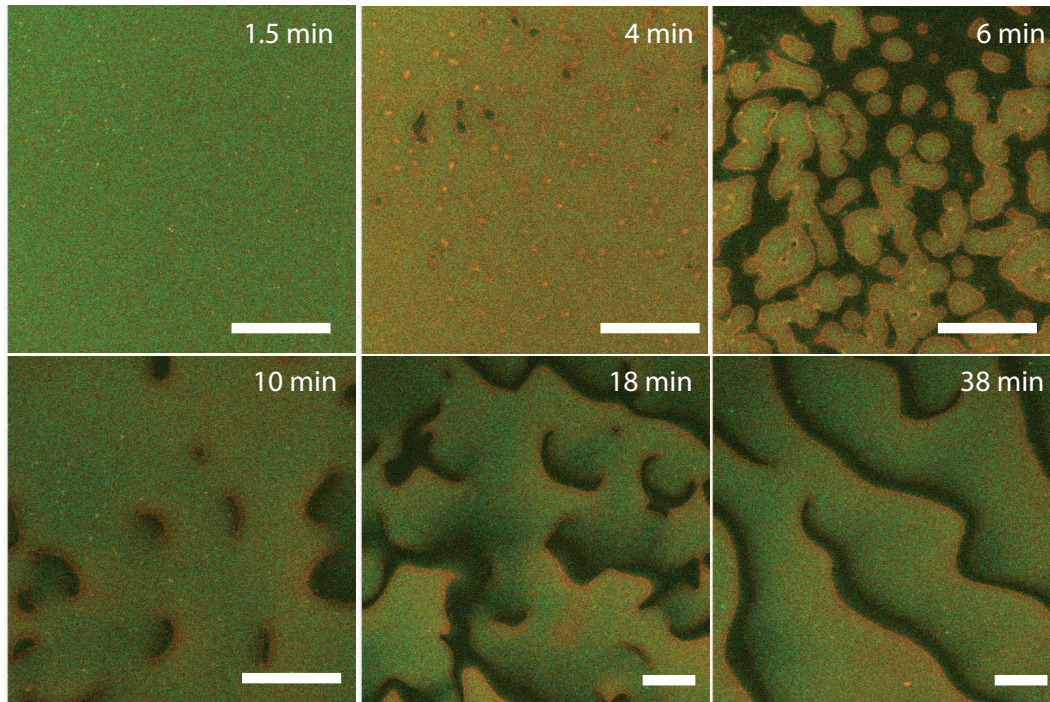
Initiation of Min patterns *in vitro*

Figure 4.1: Initiation of pattern formation. Starting from a homogeneous MinD distribution, addition of MinE initiates the formation of inhomogeneities and leads eventually to ordered structures. The frames show fluorescence images as snapshots of the system after 1.5, 4, 6, 10, 18 and 38 minutes. MinD ($1\mu\text{M}$), green channel, MinE ($1.5\mu\text{M}$), red channel. Scale bar, $50\mu\text{m}$.

with filamentous MinD structures surrounded by a thin line of MinE (see [12]). The presence of ATP proved to be essential for the pattern formation in the system. In the absence of ATP, MinD did not attach to the membrane and wave formation could not be observed. Adding the nonhydrolyzable ATP analogue adenosine 5'-O-(3-thiotriphosphate) (ATP γ S), MinD attached to the membrane forming a homogeneous protein layer. MinE was recruited to the membrane by MinD, but pattern formation did not occur. Thus energy dissipation by hydrolyzation of ATP is crucial for the formation of surface waves. To test the mobility of Min proteins in the membrane bound state, fluorescence photobleaching experiments were performed. A bleached area of MinE or MinD remained at its original position on the membrane, while the wave was propagating, see Fig. 4.4. This indicates that the waves were not the result of protein translocation on the membrane but of iterative detachment and reattachment of proteins from the buffer.

Several features of the *in vitro* structures of the Min system are strongly reminiscent of the Min oscillations *in vivo*: MinD was distributed homogeneously on the membrane in the absence of MinE, whereas dynamic patterns could be observed only in the presence of MinE. MinE was found predominantly localized at the trailing edge of a moving MinD band [21,22]. We characterized the velocity and wavelength of the surface waves as a function of MinE concentration and conclude

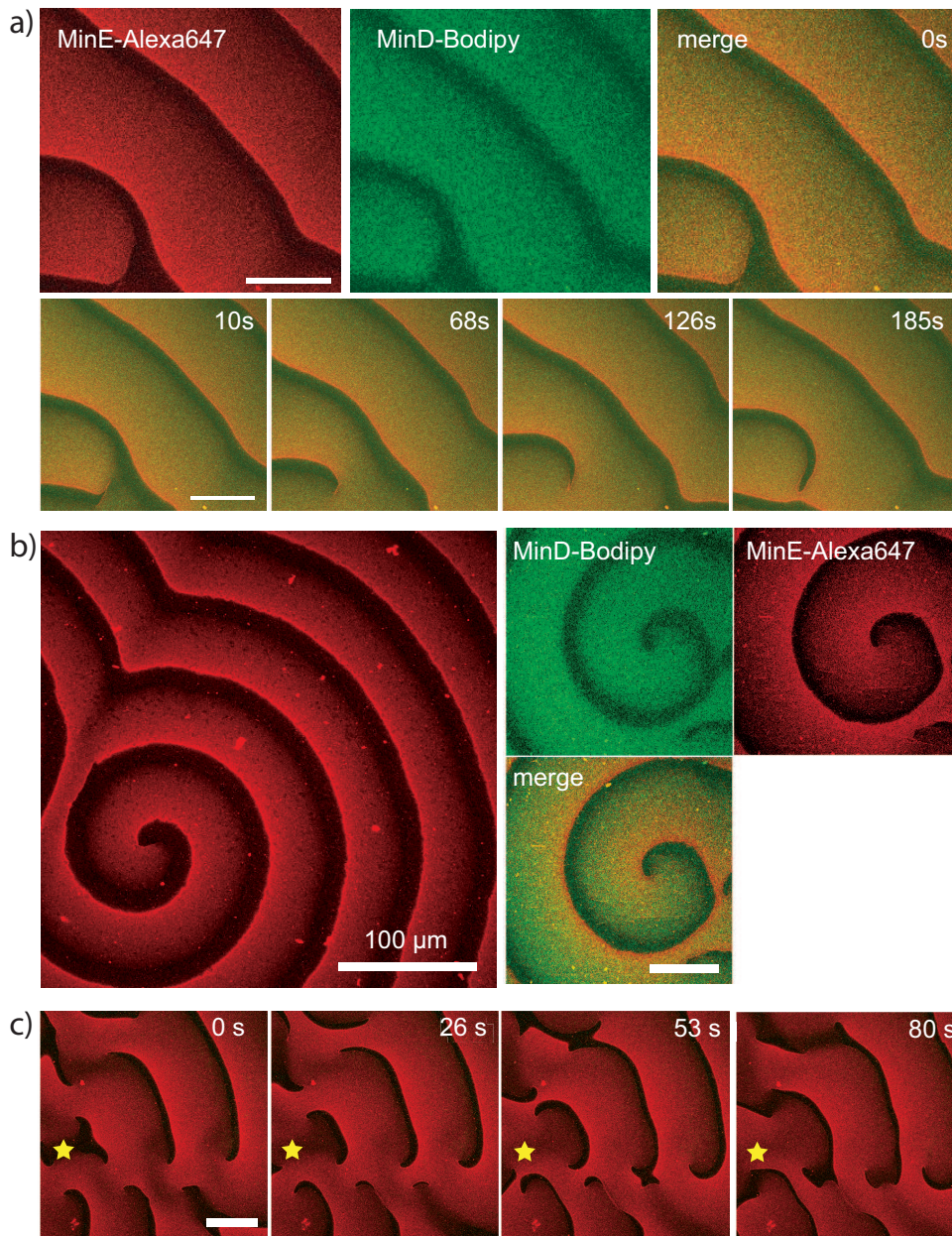
Pattern formation by Min proteins *in vitro*

Figure 4.2: Patterns formed by Min proteins attached to a supported lipid bilayer *in vitro*. a) Confocal images of self-organized proteins waves, MinD ($1\mu\text{M}$) doped with 20% Bodipy-labeled MinD (green), MinE ($1\mu\text{M}$) doped with 10% Alexa647-labeled MinE (red). The lower frame row shows the progression of traveling waves towards the upper right corner. b) Rotating spiral patterns formed by Min proteins. In the left frame only labeled MinE is shown in red (MinD, $1\mu\text{M}$; MinE, $1\mu\text{M}$). c) Double spirals formed by Min proteins. Only labeled MinE is shown (MinD, $1\mu\text{M}$; MinE, $0.5\mu\text{M}$). The star labels the center of the double spiral. All scale bars show $50\mu\text{m}$ if not differently indicated.

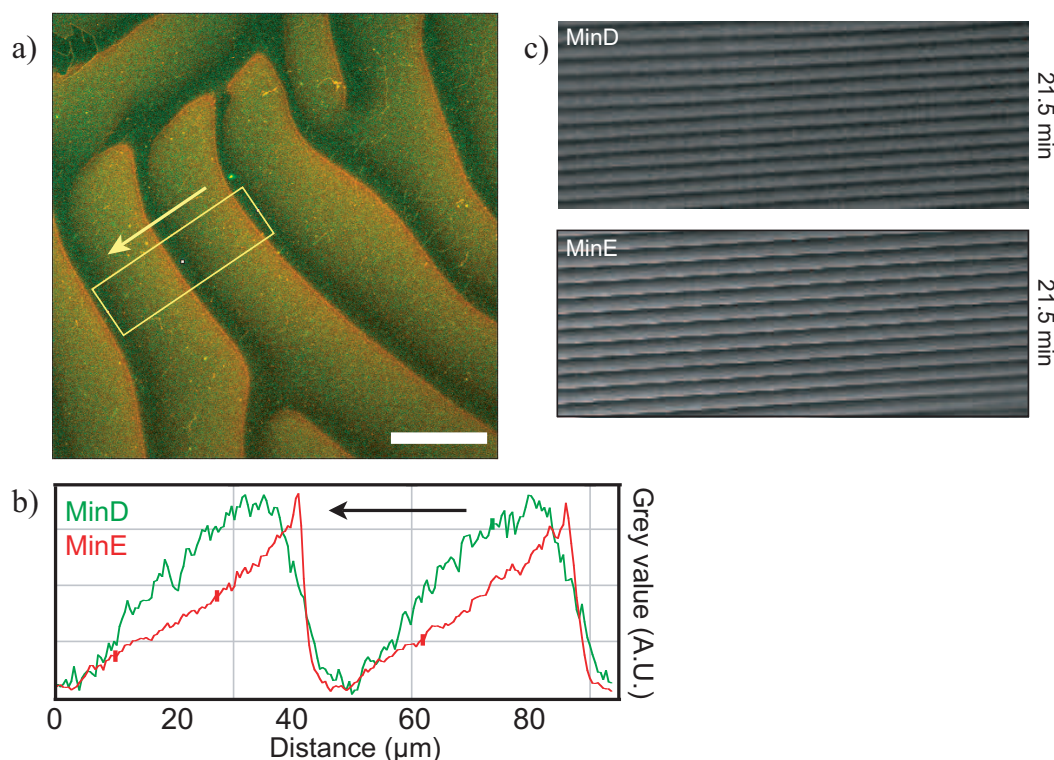


Figure 4.3: Concentration profile of Min protein waves and kymograph along a line parallel to direction of wave movement. a) Confocal image of Min protein waves on the lipid membrane. MinD ($1\mu\text{M}$), green channel; MinE ($1.5\mu\text{M}$), red channel. Scale bar, $50\mu\text{m}$. b) Intensity profile plots along the line indicated in a). The concentration was averaged over the width of the line. The arrows in a) and b) display the direction of wave propagation. c) Kymographs for MinD and MinE along the line indicated in a). The time proceeds from top to bottom. The occurrence of straight stripes in the kymographs evinces that the waves progress with constant velocity.

that the frequency of the oscillations increases with an increasing MinE/MinD ratio as *in vivo* [22]. An explanation for the different length scales of the patterns observed *in vitro* and *in vivo* is given by the theoretical description introduced in the following section 4.2; When lower values for the diffusion constants of the membrane-bound proteins were used in our model, we could also reproduce the Min oscillations observed in the cell (Figure 4.10). One possible reason for lower diffusion constants *in vivo* could be molecular crowding in the cytoplasmic membrane of *E. coli*. Thus, the mechanism generating the surface waves *in vitro* may also drive the Min oscillations *in vivo*.

These experiments have shown that complex biological behavior can emerge from a limited number of components, namely, two proteins, a membrane, and ATP. They strongly indicate that self-organization of proteins is used as a pattern forming mechanism in nature.

4.1.1 Estimation of *in vitro* diffusion constants of MinD and MinE

Diffusion constants of both proteins (D_d, D_{de}, D_D, D_E) for the *in vitro* situation were estimated from measurements performed by our collaborators Martin Loose and Jonas Ries. For the diffusion constants in the buffer, we obtained $D_D = 61.32 \pm 1.98 \mu\text{m}^2/\text{s}$ and $D_E = 58.71 \pm 2.85 \mu\text{m}^2/\text{s}$ (see [12], supporting online material) using standard tools of FCS measurement and analysis. By FRAP (fluorescence recovery after photobleaching), we measured $D_d = 0.94 \mu\text{m}^2/\text{s} \pm 50\%$ estimated error and $D_{de} = 0.19 \mu\text{m}^2/\text{s} \pm 50\%$ estimated error. These values are apparent diffusion constants and might also depend on the kinetics of protein attachment/detachment. Lower values for D_{de} compared to D_d could be accounted for with the formation of MinD/MinE complexes. For the analysis of the FRAP data, we derived a function dependent on the diffusion constant to fit the bleaching profile.

Analysis of FRAP data for MinD and MinE bound to the membrane.

In the following, we describe how values for the membrane diffusion of MinD are estimated. The same strategies have been applied to FRAP data on fluorescent MinE. For simplicity, we have assumed that only detachment/attachment processes of Min proteins and diffusion play a role in the recovery of the fluorescence. The occurrence of directed currents on the membrane is improbable since the bleached area did not move on the membrane during the recovery. We neglect spatial inhomogeneities in the buffer. The membrane profile of the entire MinD-population including the bleached molecules is assumed to be approximately constant in the bleached area and its neighborhood. Thus, dependencies of attachment and detachment rates on membrane concentrations do not have to be taken explicitly into account. Therefore, the dynamics of the fluorescent population can be described by the equations

$$\begin{aligned}\partial_t c(\mathbf{r}, t) &= D\Delta c(\mathbf{r}, t) - k_{off}c(\mathbf{r}, t) + k_{on}(T - C(t)) \\ \partial_t C(t) &= -k_{off}C(t) + k_{on}(T - C(t)),\end{aligned}\tag{4.1}$$

where $c(\mathbf{r}, t)$ denotes the MinD concentration at a certain point on the membrane, and $C(t)$ denotes the space-averaged concentration of MinD on the membrane. The variable T indicates the total number of fluorescent MinD proteins per area after bleaching. D denotes an effective diffusion constant, and the rates k_{off}, k_{on} characterise detachment and attachment. The latter equation of the equation system (4.1) can be solved on its own

$$C(t) = \left(T_0 \left(1 - \alpha \frac{A_{bl}}{A_{ges}} \right) - T \right) \frac{k_{on}}{k_{on} + k_{off}} e^{-(k_{off} + k_{on})t} + \frac{k_{on}T}{k_{off} + k_{on}},$$

where A_{bl} and A_{ges} are the area of the bleached space, and the total membrane area, respectively. T_0 denotes the total protein number per area before bleaching. α is the fraction of the bleached molecules in A_{bl} . To abbreviate the above

expression, we introduce the term $\Delta T = (T_0(1 - \alpha \frac{Abt}{A_{ges}}) - T)$. Thus, the equation for the time evolution of $c(\mathbf{r}, t)$ reads now

$$\begin{aligned} \partial_t c(\mathbf{r}, t) &= D\Delta c(\mathbf{r}, t) - k_{off}c(\mathbf{r}, t) \\ &+ k_{on} \left(\frac{k_{off}T}{k_{off} + k_{on}} - \Delta T \frac{k_{on}}{k_{on} + k_{off}} e^{-(k_{off} + k_{on})t} \right). \end{aligned} \quad (4.2)$$

This equation is inhomogeneous. To obtain the solution space, one can add the general solution of the homogeneous part $\partial_t c(\mathbf{r}, t) = D\Delta c(\mathbf{r}, t) - k_{off}c(\mathbf{r}, t)$ to a solution of the full equation. A solution of the inhomogeneous equation with no spatial dependence can be obtained by Laplace transformation

$$c_{inh}(t) = \frac{k_{on}}{k_{off} + k_{on}} T (1 - e^{-k_{off}t}) + \frac{k_{on}}{k_{off} + k_{on}} \Delta T (e^{-(k_{off} + k_{on})t} - e^{-k_{off}t}).$$

To get the general solution for the homogeneous part of Equation (4.1), we first solve the diffusion equation, for the following initial concentration: Inside the bleaching rectangle, say $[0, a] \times [0, b]$, the concentration is zero, outside it is one⁸. The solution is

$$\begin{aligned} c_{diff}(\mathbf{r}, t) &= \left(1 - \frac{1}{4\pi Dt} \int_0^b \int_0^a dx' dy' e^{-((x-x')^2 + (y-y')^2)/(4Dt)} \right) \\ &= \left(1 - \frac{1}{4} \left[\left(\operatorname{erf} \left(\frac{a-x}{2\sqrt{Dt}} \right) + \operatorname{erf} \left(\frac{x}{2\sqrt{Dt}} \right) \right) \left(\operatorname{erf} \left(\frac{b-y}{2\sqrt{Dt}} \right) + \operatorname{erf} \left(\frac{y}{2\sqrt{Dt}} \right) \right) \right] \right), \end{aligned}$$

where erf denotes the Gaussian error function. The full solution of equation (4.2) is then

$$c(\mathbf{r}, t) = \frac{k_{on}T_0}{k_{off} + k_{on}} c_{diff}(\mathbf{r}, t) e^{-k_{off}t} + c_{inh}(t).$$

Thus, the intensity profile of a bleached rectangle along x-direction for fixed y is a function

$$c(x, t) = A(t) \left(1 - \frac{1}{2} \left(\operatorname{erf} \left(\frac{a-x}{2\sqrt{Dt}} \right) + \operatorname{erf} \left(\frac{x}{2\sqrt{Dt}} \right) \right) \right) + B(t),$$

where $A(t)$ and $B(t)$ depend on y . The form of the above equation is also kept if the concentration profile in x-direction is averaged over some interval in y-direction.

To analyse the experimental data, intensity profiles along the x-direction (see Figure 4.4a and b, 2nd frame in the top image series) were fitted to the function

$$I(x) = A \left(1 - \frac{1}{2} \left(\operatorname{erf} \left(\frac{x_2-x}{\sigma} \right) + \operatorname{erf} \left(\frac{x-x_1}{\sigma} \right) \right) \right) + B. \quad (4.3)$$

at successive times. Intensities from the experiment were averaged over a certain interval of the y-axis to reduce the noise. The constants x_1 and x_2 were determined from the intensity profile at time zero after bleaching. The remaining

⁸The calculation is easily adapted to the case of a rest fluorescence in the bleached area.

parameters A , B and $\sigma = \sqrt{4Dt}$ were fitted for each time individually, see Figure 4.4a1-4 and b1-4. The parameter A scales the depth of the bleached well and B tunes the homogeneous background. Thus, σ^2 could be determined for each frame of the recorded FRAP movie and these values were plotted versus time. The diffusion constants D_d and D_{de} were then deduced fitting the linear function $\sigma^2(t) = 4Dt$ to the experimental values, see Fig. 4.4a4 and b4. These diffusion constants correspond to the translational movement of the respective fastest protein species. For example in the case of D_d , we assumed the translational movement of slow MinD/MinE complexes to be superimposed by the fast movement of MinD alone. It should be noted that the measured values are effective diffusion constants which might not only result from Brownian motion.

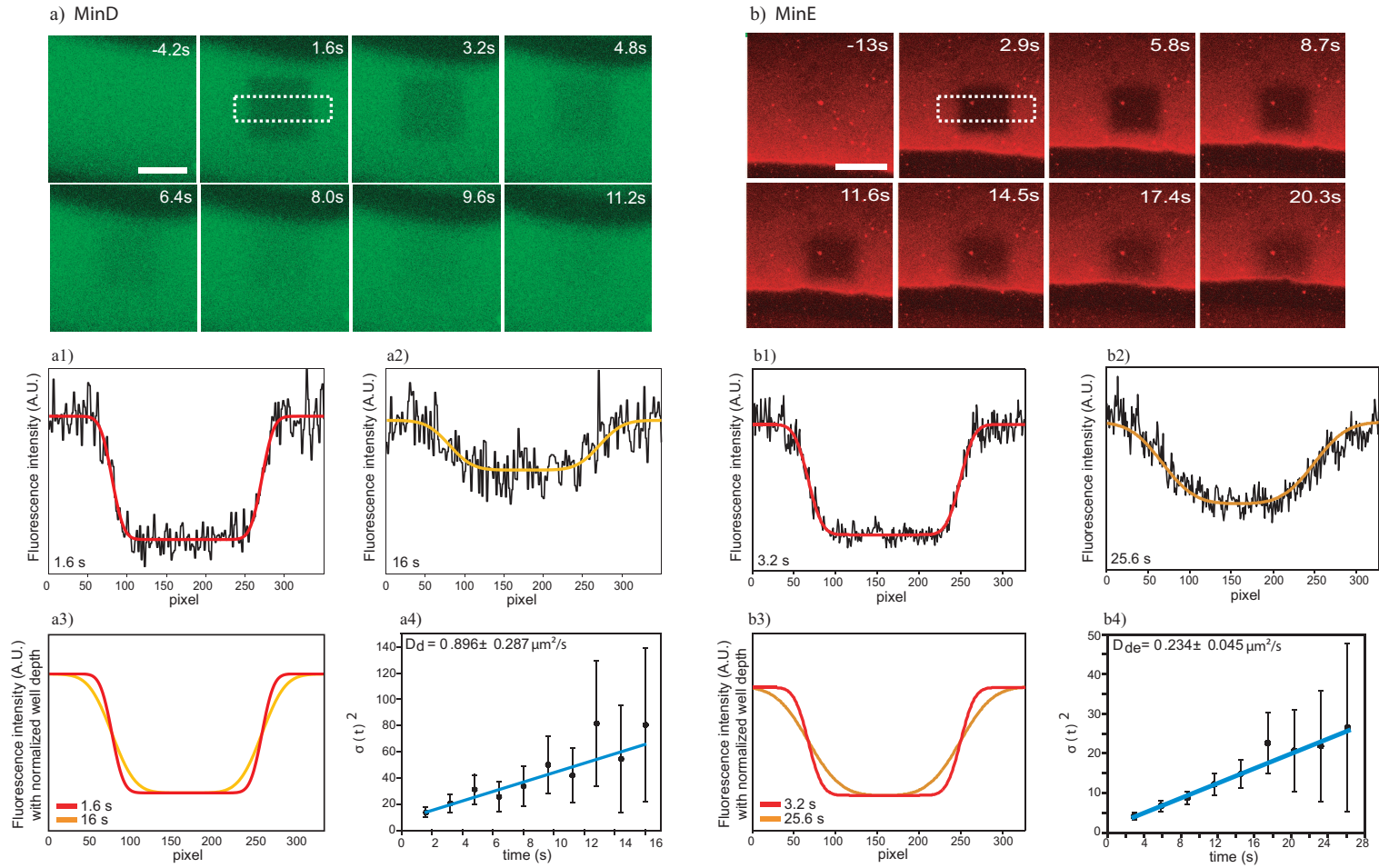


Figure 4.4: Photobleaching experiments on *in vitro* surface waves of Min proteins. a) MinD, b) MinE. Analysis of FRAP data was used to estimate effective diffusion constants of MinD and MinE in the membrane-bound state. a1), a2) Intensity profile of MinD along the line given in the second frame in a) at a fixed time after bleaching. Solid lines are fits to the function (4.3). a3) Fits for different times with normalized well depth. a4) Fitted parameter $\sigma^2(t) = 4Dt$ for successive times. D_d is determined by linear regression. The images b1)–b4) are the analogues of a1)–a4) but for MinE FRAP data.

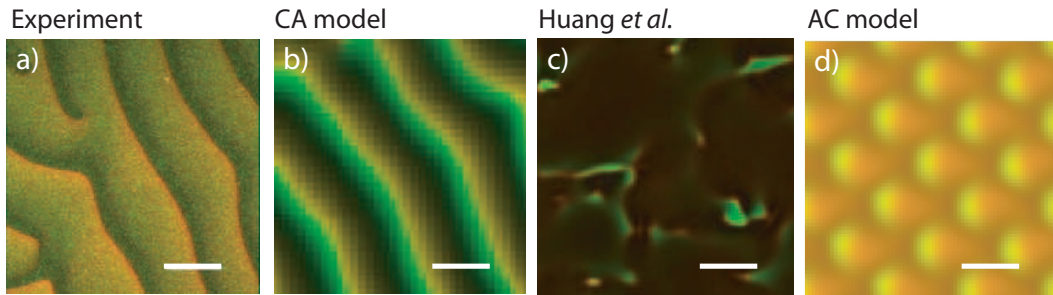


Figure 4.5: Comparison of pattern formation in the experiment and different computational models. a) Confocal image of protein waves from the experiment. b) Waves forming in the CA model given by equations (4.4)–(4.7). c) and d) present structures produced by the model suggested by Huang *et al.* [35] and by the AC model (see Section 2.3.2), respectively. The scale bars show $50\mu\text{m}$. The green color channel encodes MinD concentration, the red channel encodes MinE concentration.

4.2 Modeling *in vitro* dynamics of Min proteins

We wanted to understand the generation of the instability and the emergence of structures in the experiments described above. We use a mesoscopic description in terms of concentration fields for the Min proteins. Many descriptions of this kind have been suggested to account for the Min patterns in the *E. coli* cell, which were either on the basis of a classical reaction-diffusion mechanism or which assumed attractive interactions between bound MinD molecules leading to an aggregative current on the membrane (see Section 2.3.1). However, the waves observed in the experiments were qualitatively different from the behavior predicted by existing theories (see Figure 4.5 c,d).

In the experiment, regions of high MinE densities initiated MinD detachment and thus pattern formation. From this observation, we deduced a computational model that includes cooperative effects during MinE binding to the membrane similar to those suggested in [32]⁹. The state of the system is described by the densities c_D and c_E of MinD and MinE in the buffer, along with the densities c_d and c_{de} of MinD and MinD/MinE complexes on the membrane. The time evolution of the concentrations is given by dynamic equations which embody the concept of cooperative attachment (CA)

$$\partial_t c_D = +\omega_{de}c_{de} - c_D(\omega_D + \omega_{dD}c_d) + D_D\Delta c_D \quad (4.4)$$

$$\partial_t c_E = +\omega_{de}c_{de} - c_Ec_d(\omega_E + \omega_{eE}c_{de}^2) + D_E\Delta c_E \quad (4.5)$$

$$\partial_t c_d = -c_Ec_d(\omega_E + \omega_{eE}c_{de}^2) + c_D(\omega_D + \omega_{dD}c_d) + D_d\Delta c_d \quad (4.6)$$

$$\partial_t c_{de} = -\omega_{de}c_{de} + c_Ec_d(\omega_E + \omega_{eE}c_{de}^2) + D_{de}\Delta c_{de}. \quad (4.7)$$

The respective attachment/detachment dynamics is parametrized by the parameters $\omega_D, \omega_{dD}, \omega_E, \omega_{eE}$ and ω_{de} . The first terms in Equations (4.4) and (4.5) describe unbinding of MinD/MinE complexes from the membrane. The appearance of this term with a minus-sign in Equation (4.7) assures that no material

⁹This model however includes protein synthesis and degradation as an essential ingredient, which was shown to be unimportant for the functioning of the Min system.

is lost or generated during this process. The second term in Equation (4.4), $c_D(\omega_D + \omega_{dD}c_d)$, describes binding of MinD to the membrane, with an effective rate that increases with higher concentrations of membrane-bound MinD. The second term in Equation (4.5), $c_Ec_d(\omega_E + \omega_{eE}c_{de}^2)$, accounts for cooperative attachment of MinE to membrane-bound MinD/MinE complexes. Note that we assume in our model cooperative attachment for MinD as well as for MinE. For the exchange of ADP for ATP in unbound MinD, we assume that it is so fast that we do not have to consider explicitly the concentrations of MinD bound to ADP. For each rate, we used only the terms with the lowest order non-linearity that were sufficient to reproduce the phenomena observed experimentally. All parameters are effective parameters and might account for multiple processes. Diffusive transport of the proteins is captured by the last terms in the equations, where Δ is the Laplace operator.

Units of concentrations. For simplicity, the densities c_D and c_E in Equations (4.4)–(4.7) are taken as two-dimensional surface densities. This concept is motivated by the following considerations: Particle exchange between membrane and buffer happens mostly within a certain layer of the buffer beneath the membrane, parallel to the membrane surface. This is due to the finite diffusion constant in the buffer and finite binding rates. The height of this layer will be determined by the buffer diffusion constants of MinD and MinE as well as typical residence times of Min proteins in the buffer. A buffer diffusion of $60\mu\text{m}^2/\text{s}$ and a residence time of 1–3s gives as typical distance $\approx 10\mu\text{m}$. Thus, within an exchange layer beneath the membrane with a height on the order of magnitude $10\mu\text{m}$, proteins will permanently switch between diffusion in the buffer and a membrane bound state. Between the exchange layer and the bulk part of the buffer on top, particle currents will be negligible since concentration gradients are not strong at this distance from the membrane. Thus, we assume that the bulk part can be neglected for the dynamics on the membrane. We describe binding of proteins from the exchange layer to the membrane by an effective binding rate proportional to the surface concentration of the exchange layer somewhat simplifying the actual situation in the experiment. Since the height of the exchange layer can only be roughly estimated, we transform the actual protein concentrations in the buffer into surface densities used in the equations by multiplying the volume concentrations with the total height of the buffer. Experimentally, we checked that stirring of the buffer did not have an effect on the protein pattern on the membrane. Thus concentration gradients in the bulk of the buffer do not seem to play a significant role.

Emerging patterns. In a suitable parameter regime, the equations produce patterns made up of ordered wave trains traveling with a constant velocity similar to the structures observed in the *in vitro* experiments. Examples of solutions are shown in Figure 4.6. MinE cooperativity proved to be crucial to reproduce the dynamic patterns observed experimentally (Figure 4.2). Our theory captures a similar protein density distribution within a protein band (Figure 4.8). The peak of the MinE distribution follows the concentration maximum of MinD. However, we do not capture the sharp drop of the MinE concentration after the peak. Experimentally obtained dependencies of wavelengths and velocities on the MinE concentration are qualitatively reproduced by the theory along general lines (see Figure 4.7c and d).

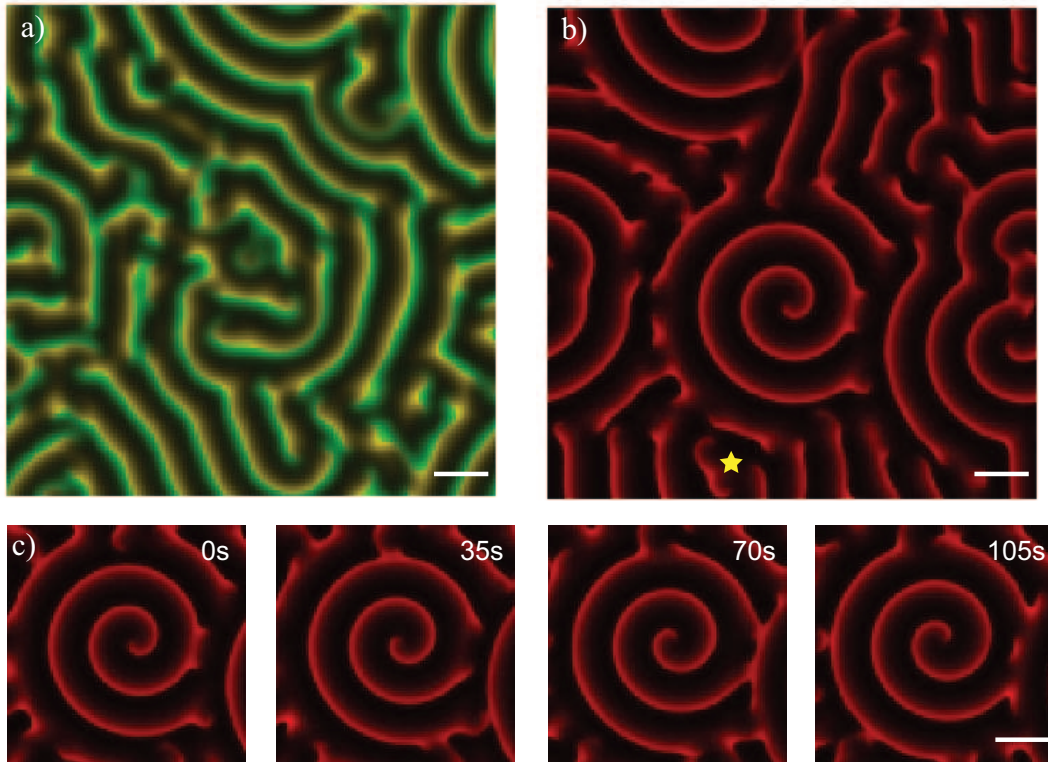
In silico Min patterns (CA model)

Figure 4.6: Patterns generated by the computational CA model given by the equations (4.4)–(4.7). The images a) and b) show a snap shot from simulations on a domain with side length $900\mu\text{m}$ and periodic boundary conditions. The green color channel encodes MinD intensity, the red channel encodes MinE intensity. c) Rotating spiral from b) at progressive times. The yellow star in b) marks the center of an occurring double spiral in the simulation. The scale bars indicate $100\mu\text{m}$. The chosen parameters and initial conditions are given in the paragraph on numerical methods 4.2.1.

The values of the diffusion constants in the buffer and on the membrane influence the characteristic size of the developing pattern. Diffusion in the buffer is by orders of magnitude larger than on the membrane. Still, the bulk cannot be assumed to be well-stirred. The finite values for the diffusion constants in the buffer assure that homogeneous oscillations are suppressed.

4.2.1 Numerical methods and parameter choice

Equations (4.4)–(4.7) have been solved using a forward Euler discretization scheme for the time step.

Simulation shown in Figure 4.6a We used as initial concentrations a homogeneous protein distribution plus random fluctuations which were independently chosen for each grid point and took values up to a hundredth of the constant concentration value. The grid spacing of the simulation is $7.5\mu\text{m}$ and the time step $\Delta t = 0.01\text{s}$.

Simulation shown in Figure 4.6b The initial concentrations were homogeneous protein distributions with a spiral profile of small amplitude added to

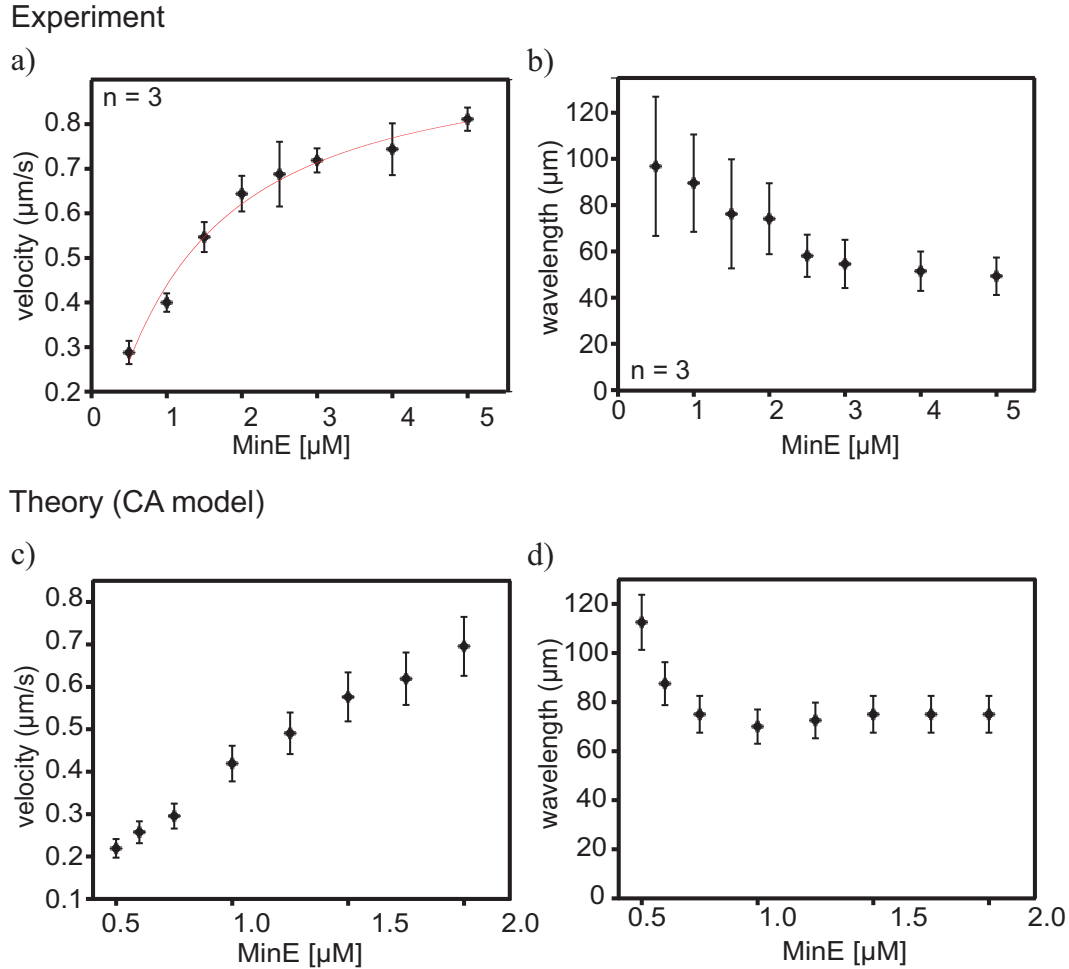


Figure 4.7: Surface wave velocity and wavelength as a function of MinE concentration (MinD, $1\mu\text{M}$). a) and b) show experimental data. Each data point has been obtained from $n = 3$ independent measurements. Error bars indicate the standard deviation. Fitting data of a) to the Hill equation yielded $v_{max} = 0.94\mu\text{m/s}$. c) and d) display results from the computational model. Error bars indicate the uncertainty with which velocity and wavelength could be extracted from the simulations. Experiment and theory report an increase of the wave velocity and a dip of the wavelength for increasing MinE concentrations. Parameters of the simulations were chosen as in Figure 4.6 apart from the MinE concentration. For MinE concentrations higher than $2\mu\text{M}$ the spatial patterns were lost in the simulation and homogeneous oscillation occurred.

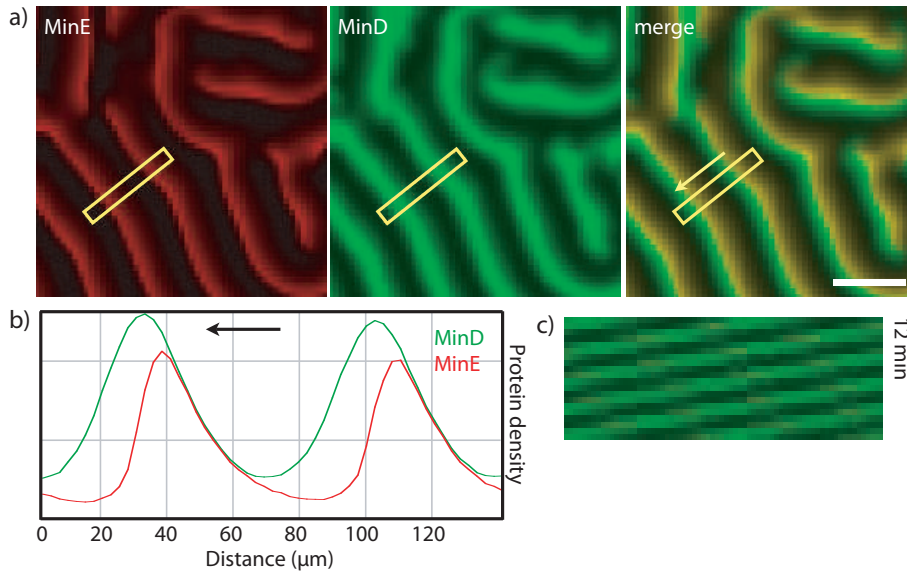


Figure 4.8: Concentration profile of waves and kymograph along a line parallel to direction of movement predicted by the computational AC model. a) Image of Min protein waves with MinD concentration encoded by green color intensity and MinE encoded by red color intensity. Scale bar, $50\mu\text{m}$. Intensity profile plots along the line indicated in a). The concentration was averaged over the width of the line. The arrows in a) and b) displays the direction of wave propagation. c) Kymograph for MinD along the line indicated in a). The time proceeds from top to bottom.

MinD. In this way, we wanted to check if a spiral distribution is stable in the system. Starting out with a spiral profile does not necessarily mean, that this structure is kept during the simulation. For the presented model, wavelengths and extension of the spiral had to be chosen carefully in order to keep the spiral. In the cases where the spiral was kept, it deformed after simulation start and changed its profile and wavelength, sometimes also the position of its middle. For instance in Figure 4.6b the middle of the spiral has moved downwards away from the middle. We also tried to obtain spirals in this way integrating the dynamical systems described in [13,37] and [35], which were introduced in the Section 2.3.1. However, in these cases the initial spirals resolved very fast and vanished completely. The initial spiral profile was achieved by adding the function $0.01 \sin(\sqrt{(x^2 + y^2)}/\lambda^2 + \varphi(x, y))$ to each grid point not more than $105\mu\text{m}$ away from the middle of the simulated square. The origin of the coordinate system was set to be the middle of the grid. The function $\varphi(x, y)$ is the angle of polar coordinates in the plane. The value of the wavelength λ was set to $48.75\mu\text{m}$. The grid spacing of the simulation is $3.75\mu\text{m}$ and the time step $\Delta t = 0.01\text{s}$.

The following parameters are chosen for the simulation of Figure 4.6a and b: $\omega_{de} = 0.029\text{s}^{-1}$, $\omega_D = 2.9 \cdot 10^{-4}\text{s}^{-1}$, $\omega_{dD} = 4.8 \cdot 10^{-8}\mu\text{m}^2/\text{s}$, $\omega_E = 1.9 \cdot 10^{-9}\mu\text{m}^2/\text{s}$, $\omega_{eE} = 2.1 \cdot 10^{-20}\mu\text{m}^6/\text{s}$, $D_D = D_E = 60\mu\text{m}^2/\text{s}$, $D_d = 1.2\mu\text{m}^2/\text{s}$, $D_{de} = 0.4\mu\text{m}^2/\text{s}$. Protein concentrations in the buffer were taken as $1\mu\text{M}$ for MinD and MinE. Converting this value to a 2D concentration by multiplication with the height of the buffer, which was estimated as 5mm , gives a surface density of $3 \cdot 10^6$ particles per μm^2 . In total, a square of $900\mu\text{m}$ was integrated with periodic boundary conditions. In

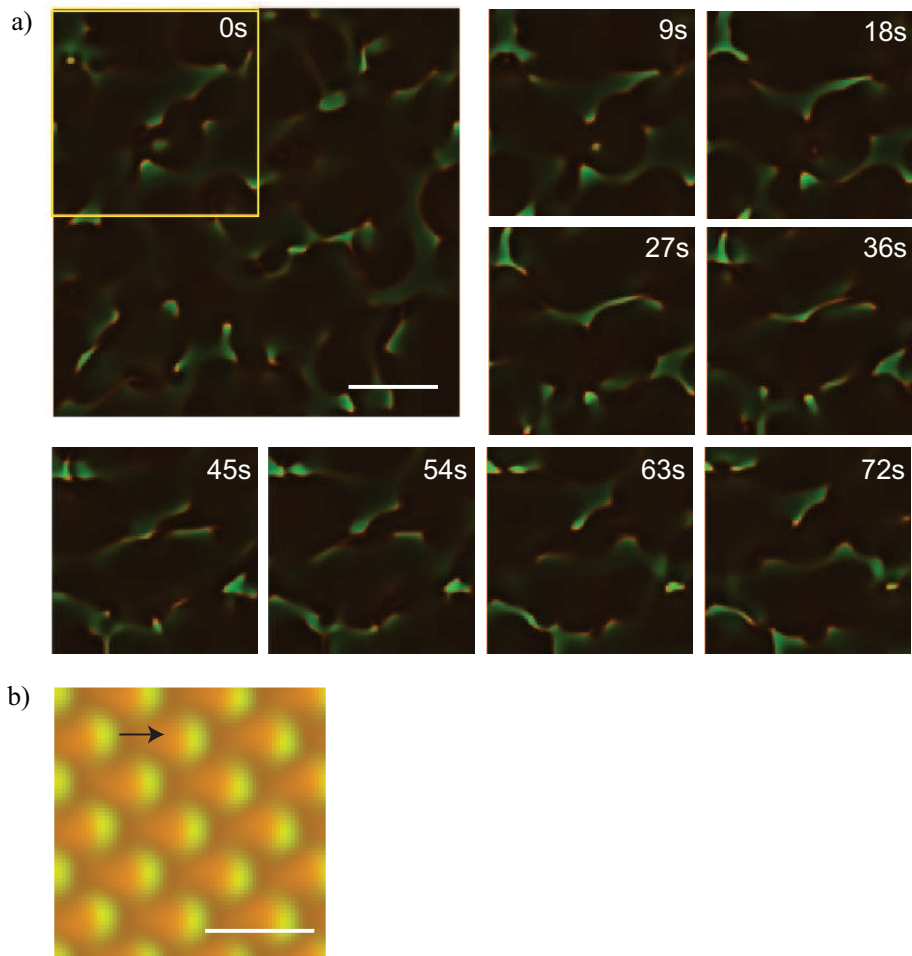


Figure 4.9: a), b) Patterns generated by the computational models suggested by Huang and colleagues [35] and by the AC model, respectively (see also Section 2.3.1). The green color channel encodes MinD concentration, the red channel encodes MinE concentration. a) The first frame shows the entire simulated domain. The following smaller frames show the simulation results for exceeding times in the extract indicated in yellow for $t = 0s$. We searched the parameter space of the model in the neighborhood of the parameters given in [35] and [49] and did not find a regime where ordered wave trains or spirals formed. b) A quadratic domain of $250\mu m$ is shown with periodic boundary conditions. The pattern stays equal over time but translocates to the right with constant velocity $v \approx 0.25\mu m/s$ as indicated by the black arrow. Scanning the parameter space of the model close to the bifurcation, we did not find regions of traveling plane waves. The scale bars indicate $100\mu m$. The parameters of the simulations a) and b) are given in 4.2.1.

the simulations, concentrations reach maximal values of $\sim 6 \cdot 10^6 \mu\text{m}^{-2}$ for MinD, and $\sim 5.4 \cdot 10^6 \mu\text{m}^{-2}$ for MinE. For the given parameters different values for the diffusion constant D_{de} have been tested. In the range from $0.5 \mu\text{m}^2/\text{s}$ to $0.1 \mu\text{m}^2/\text{s}$ the results of simulations were qualitatively similar.

Testing other computational models. Of course, the question arises which Min patterns are predicted in a flat two-dimensional geometry by theoretical descriptions suggested previously. Accordant simulations of the models presented in [35] and [13] are shown in Figure 4.9. For Figure 4.9a, a square of $450 \mu\text{m}$ has been simulated with periodic boundary conditions. The total concentration of MinD in the system was $1 \mu\text{M}$, and of MinE $0.35 \mu\text{M}$. The remaining parameters were $\sigma_{de} = 0.7 \text{s}^{-1}$, $\sigma_{ADP \rightarrow ATP} = 1 \text{s}^{-1}$, $\sigma_D = 0.098 \text{s}^{-1}$, $\sigma_{dD} = 6.6 \cdot 10^{-7} \mu\text{m}^2/\text{s}$, $\sigma_E = 4 \cdot 10^{-5} \mu\text{m}^2/\text{s}$, $D_D = D_E = 63 \mu\text{m}^2/\text{s}$, $c_{\text{max}} = 18.75 \cdot 10^6 \mu\text{m}^{-2}$. The concentrations range for MinD from 0 to $\sim 17.25 \cdot 10^6 \mu\text{m}^{-2}$, and for MinE from 0 to $\sim 7.5 \cdot 10^6 \mu\text{m}^{-2}$. Again spatial variations along the z-direction in the buffer were neglected and concentrations were assumed as surface concentrations. Figure 4.9b displays results of Min protein dynamics according the aggregation current model. Shown is a square of $250 \mu\text{m}$ side length with periodic boundary conditions. The total concentration of MinD in the system was $1 \mu\text{M}$, and of MinE $1 \mu\text{M}$. The remaining parameters were $\omega_{de} = 0.002 \text{s}^{-1}$, $\omega_D = 0.0004 \text{s}^{-1}$, $\omega_E = 3.3 \cdot 10^{-9} \mu\text{m}^2/\text{s}$, $c_{\text{max}} = 6 \cdot 10^6 \mu\text{m}^{-2}$, $D_d = 1.5 \mu\text{m}^2/\text{s}$, $k_1 = 7.2 \cdot 10^{-12} \mu\text{m}^6/\text{s}$, $k_2 = 1.8 \cdot 10^{-10} \mu\text{m}^8/\text{s}$, $k_1 = -k_1$, $k_2 = 10^{-4} \cdot k_2$. The concentrations range for MinD from 0 to $\sim 1 \cdot 10^6 \mu\text{m}^{-2}$, and for MinE from 0 to $\sim 6 \cdot 10^5 \mu\text{m}^{-2}$. The buffer proteins were assumed to be well-stirred, i.e. spatial variations of the concentrations within the buffer were neglected.

4.3 Solutions of the derived CA model in cell geometries

4.3.1 Wild type cells

We numerically solved the dynamic equations (4.4)–(4.7) of the cooperative attachment model also in a bacterial geometry (see Figure 4.10), where we used lower values for the diffusion constants of the membrane bound proteins according to [46]. We assumed the pattern to be invariant with respect to rotations around the bacterium's long axis, which led to an effectively one-dimensional description. We have used a 1D spatial grid with lattice spacing of $0.2 \mu\text{m}$. The time step¹⁰ was $\Delta t = 3 \cdot 10^{-5} \text{s}$. The resulting dynamics is shown in Fig. 4.10 and clearly reveals the pole-to-pole oscillations typical for the Min proteins in *E. coli*.

4.3.2 Thick cells

In Chapter 3, we have seen that solutions for the Min dynamics in cells with a radius to length ratio greater than in usual *Escherichia coli* cells are not anymore

¹⁰The smaller time step compared to the simulation of the *in vitro* setting is necessary due to the smaller grid spacing Δx in order to still match the Courant stability criterion.

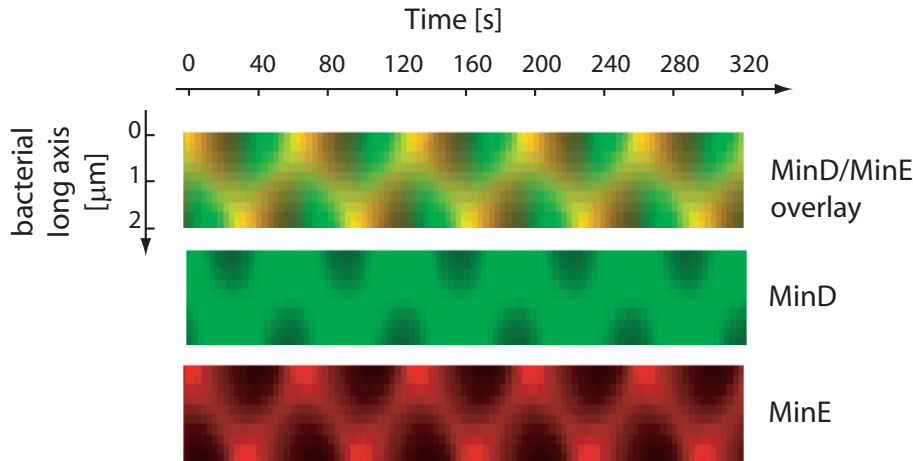


Figure 4.10: Example of pattern formation in the cell according to the equations (4.4)–(4.7). MinD intensity, green channel; MinE intensity, red channel. The oscillation period is 67s. The overall MinD and MinE concentration was set to $1000\mu\text{m}^{-1}$ and $400\mu\text{m}^{-1}$, respectively. The cell length is $2\mu\text{m}$. The remaining parameter values are $\omega_{de} = 0.125\text{s}^{-1}$, $\omega_D = 0.0013\text{s}^{-1}$, $\omega_{dD} = 9.3 \cdot 10^{-4}\mu\text{m}/\text{s}$, $\omega_E = 3.8 \cdot 10^{-5}\mu\text{m}/\text{s}$, $\omega_{eE} = 8 \cdot 10^{-9}\mu\text{m}^3/\text{s}$, $D_D = D_E = 12.5\mu\text{m}^2/\text{s}$, $D_d = D_{de} = 0.013\mu\text{m}^2/\text{s}$. For simplicity, we used the same cytoplasmic diffusion constants for MinD and MinE. The respective values are motivated by Meacci *et al.* [46].

rotationally symmetric with respect to rotation around the long axis of the bacterium. This is predicted by the AC model as well as by the model presented by Huang, Meir and Wingreen [35], (see also 2.3.1). In general, it is expected that each modeling dynamical system should give solutions of this kind for the cell radius becoming larger than L_{crit}/π , where L_{crit} is the minimal cell length for which oscillations occur. Inserting $2\mu\text{m}$ for this quantity gives a threshold radius of $\approx 0.65\mu\text{m}$. If the cell radius gets into this regime, the smallest wave vector of circumferential modes takes about the same value as the smallest non-vanishing long axis mode for a cell of $2\mu\text{m}$ length. Since this wave vector is unstable, yielding long axis oscillations, also the lowest circumferential mode should become unstable. Probing the behavior of the computational model derived for the description of the *in vitro* structures observed in two dimensions, we also find solutions which vary along the cell circumference. Two examples are shown in Fig. 4.11 and Fig. 4.12. In Fig. 4.11, a traveling wave forms which runs around the cell staying in a fixed plane, crossing the cell poles. This solution in fact looks similar to the oscillations which we observed *in vivo* in cells with enlarged radius, see Figure 3.6. In Fig. 4.12, we present a chiral solution similar to the one shown in Fig. 3.1. A solution with the reversed handedness exists simultaneously.

Numerical methods and parameters. The simulations were performed subdividing the cytoplasmic bulk into pie slices adapted to the grid on the membrane of the model cell. Thus cytoplasmic concentrations were averaged over one pie slice. A control simulation with a finer subdivision of the cytoplasmic bulk did not display qualitative differences in the distribution of membrane-bound proteins. The chosen parameters for the solution shown in Fig. 4.11 were $\omega_{de} = 0.125\text{s}^{-1}$, $\omega_D = 5.6 \cdot 10^{-4}\mu\text{m}/\text{s}$, $\omega_{dD} = 6.3 \cdot 10^{-4}\mu\text{m}^3/\text{s}$, $\omega_E = 2.5 \cdot 10^{-5}\mu\text{m}^3/\text{s}$, $\omega_{eE} = 1.2 \cdot 10^{-8}\mu\text{m}^7/\text{s}$, $D_D = D_E = 12.5\mu\text{m}^2/\text{s}$, and $D_d = D_{de} = 0.013\mu\text{m}^2/\text{s}$. The av-

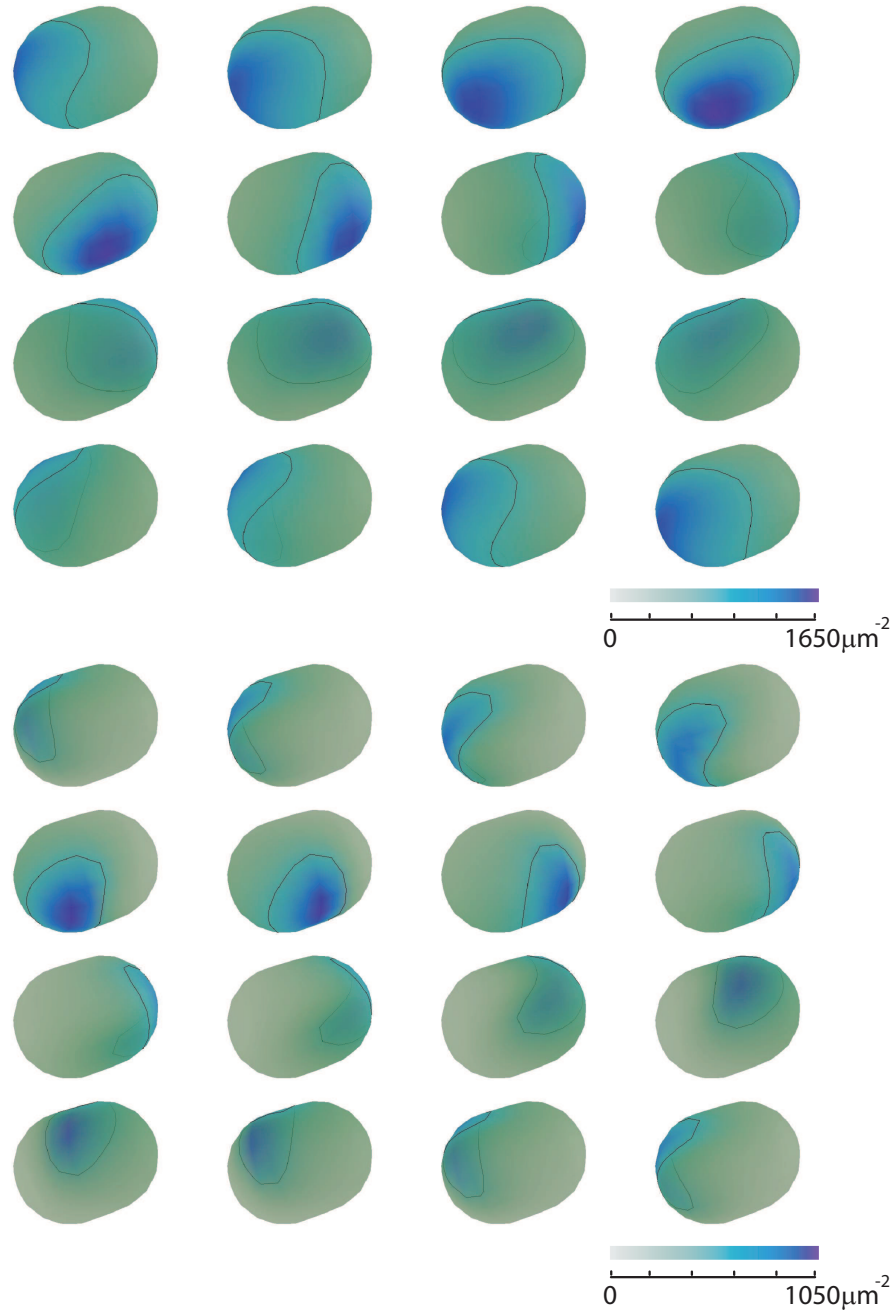


Figure 4.11: Solution of the dynamic equations (4.4)-(4.7) with circumferential modulations. a) Concentration of membrane-bound MinD, $c_d + c_{de}$. The black line on the bacterium indicates an iso-concentration curve at half the concentration maximum. The concentration peak travels around the cell staying in a plane which crosses the cell poles. The concentration range is indicated in the legend shown at the bottom. b) Distribution of MinE on the membrane corresponding to the solution presented in a).

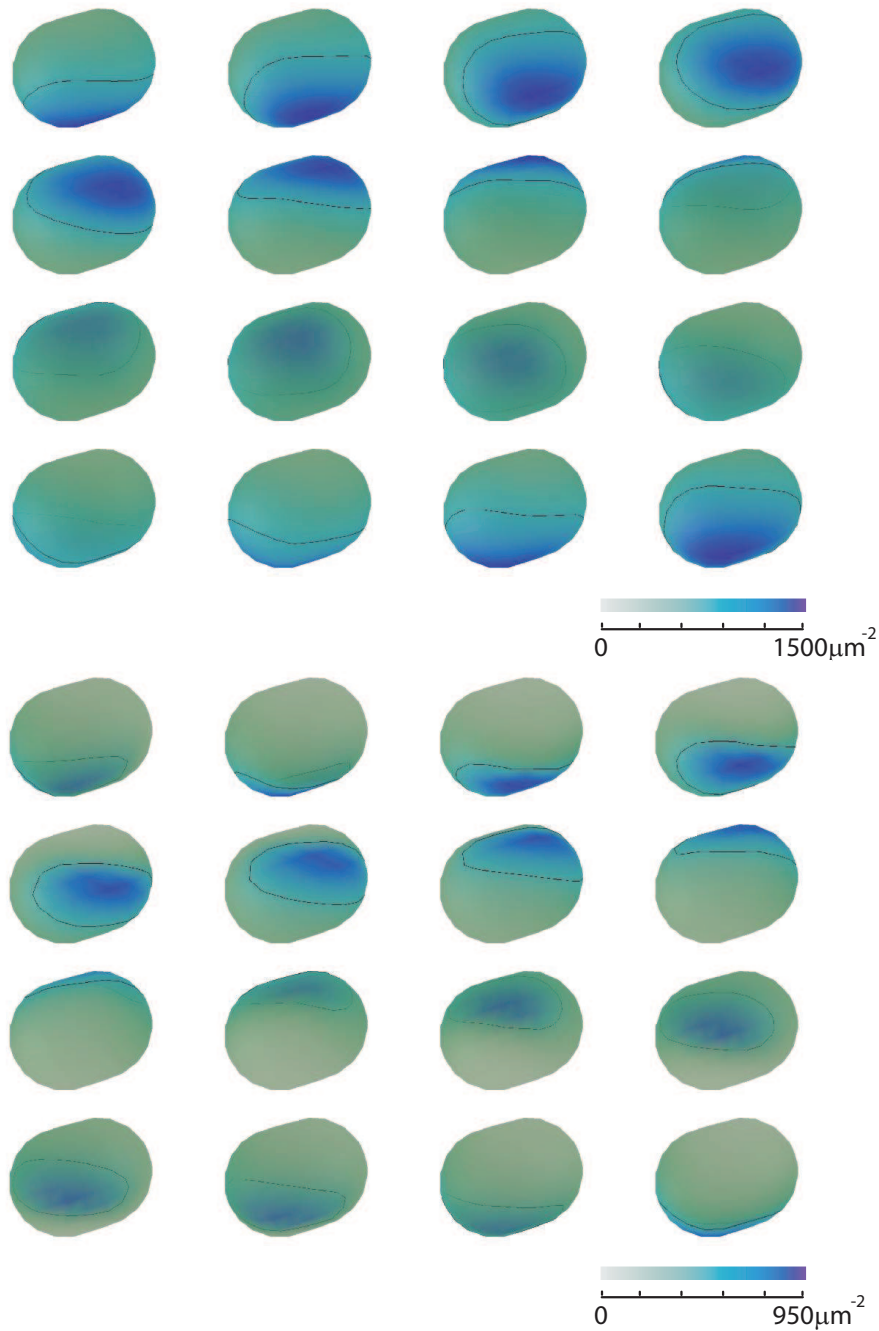


Figure 4.12: Chiral solution of the dynamic equations (4.4)-(4.7). a) Concentration of membrane-bound MinD, $c_d + c_{de}$. The black line on the bacterium indicates an iso-concentration curve at half the concentration maximum. In addition to the pole-to-pole oscillations, the distribution turns around the long axis. A solution with the opposite sense of rotation coexists with the one presented here. The concentration range is indicated in the legend shown at the bottom. b) Distribution of MinE on the membrane corresponding to the solution presented in a).

average protein density was for MinD $1500\mu\text{m}^{-3}$ and for MinE $600\mu\text{m}^{-3}$. For the solution presented in Fig. 4.11, the parameters were equal apart from ω_{dD} which was set to $\omega_{dD} = 0.0013\text{s}^{-1}$.

4.3.3 Filamentous cells

Escherichia coli cells with a cell length that exceeds typical wild type lengths are called filamentous cells. Filamentous cells are known to change their oscillation pattern of Min proteins. The observed standing wave of protein concentration gains wave nodes such that cells expressing fluorescent MinD exhibit additional stripes (see also Fig. 2.4). For cells exceeding $6\mu\text{m}$ in length, we observed also the occurrence of traveling waves of Min proteins, see Fig. 4.13b,c. The cell shown there has a length of $11\mu\text{m}$.

We have probed the model presented in this chapter in filamentous cells. Examples of solutions are shown in Fig. 4.13 and 4.14. Fig. 4.13 displays a $10\mu\text{m}$ model cell. The parameters are chosen as for the solution in a $2\mu\text{m}$ cell presented in Fig. 4.10. For this parameter set, the system switches directly to traveling waves for longer cells. Wave nodes of the concentration profile are not gained. In Fig. 4.14, we present simulations of the model for different cell lengths: a) $2\mu\text{m}$, b) $5\mu\text{m}$. These simulations were performed for parameter values $\omega_{de} = 0.17\text{s}^{-1}$, $\omega_D = 0.017\text{s}^{-1}$, $\omega_{dD} = 3.3 \cdot 10^{-3}\mu\text{m}/\text{s}$, $\omega_E = 3.3 \cdot 10^{-5}\mu\text{m}/\text{s}$, $\omega_{eE} = 8.3 \cdot 10^{-10}\mu\text{m}^3/\text{s}$, $D_D = D_E = 1.7\mu\text{m}^2/\text{s}$, and $D_d = D_{de} = 0.008\mu\text{m}^2/\text{s}$. The average protein density for MinD and for MinE was $1000\mu\text{m}^{-1}$. In a length range from $2 - 8\mu\text{m}$, standing wave solutions are preferred. From about $10\mu\text{m}$ on, the standing wave solution starts to get instable. Note that the diffusion constants in the cytoplasm were chosen lower than the actually measured values from [46] which were for MinD $\sim 16\mu\text{m}^2/\text{s}$ and $\sim 10\mu\text{m}^2/\text{s}$ for MinE. Also the MinE fraction is higher than usually anticipated.

In general, the model seems to prefer traveling wave solutions for longer cells which is not surprising as it was designed to describe traveling waves in an open geometry. This fact suggests that the model might be too slender to explain all the phenomena observed in the Min system.

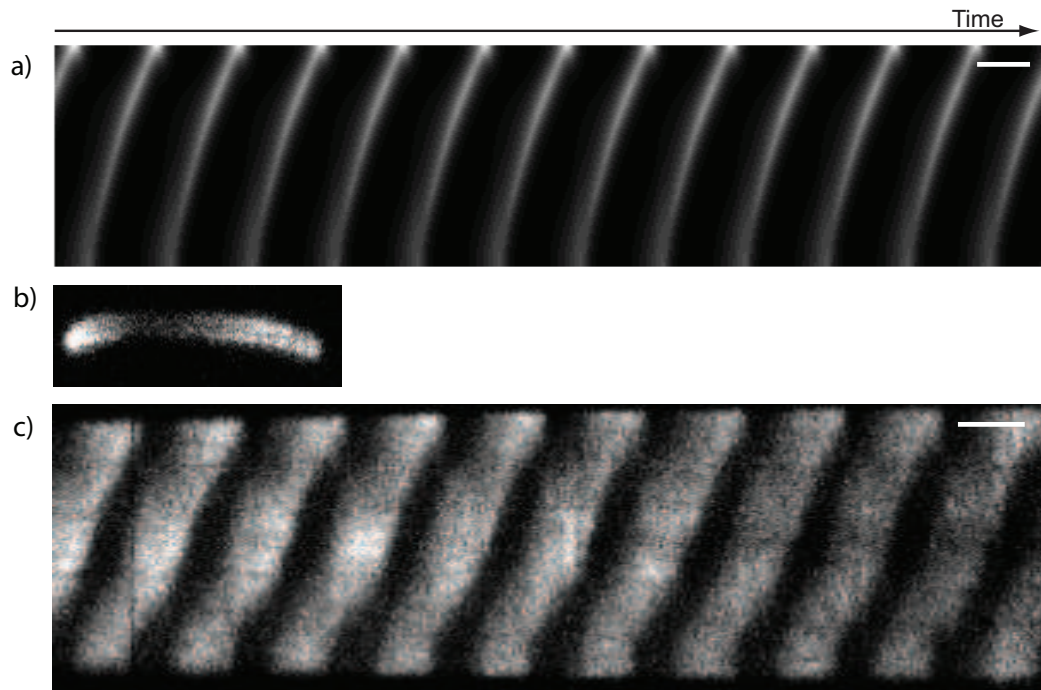


Figure 4.13: a) Kymograph of a traveling wave solution in a one-dimensional cell of $10\mu\text{m}$ length. The oscillation period is 100s . concentrations range from $0 - 11000\mu\text{m}^{-1}$ for MinD and $0 - 6900\mu\text{m}^{-1}$ for MinE. b) Micrograph of *E. coli* cell expressing fluorescent MinD with a length of $11\mu\text{m}$. c) Kymograph of the cell shown in b), recorded for a time interval of 870s . Thus the oscillation period is roughly 87s . Scale bars show 1min .

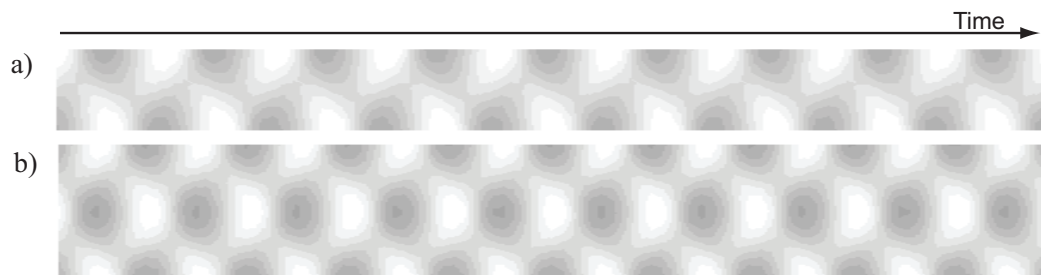


Figure 4.14: Kymographs of Min oscillations in a one-dimensional model cell. Cell lengths are $2\mu\text{m}$ in a) and $5\mu\text{m}$ in b). The oscillation periods are 66.7s and 60s in a) and b), respectively. MinD concentrations range from $800 - 1200\mu\text{m}^{-1}$ and MinE concentrations from $200 - 530\mu\text{m}^{-1}$.

Chapter 5

Mobility of Min proteins in *Escherichia coli* measured by fluorescence correlation spectroscopy

Theoretical works and *in vitro* experiments [12] have indicated that the pole-to-pole oscillations of Min proteins in *Escherichia coli* are formed by self-organization of MinD and MinE [61]. At the heart of self-organization of the Min system are successive biochemical state changes and displacement of Min proteins (see Fig. 2.5). Respective dynamical processes are attachment and detachment of Min proteins to and from the membrane, diffusion in the cytoplasm and possibly movement of Min proteins on the membrane. Each of these processes adds a characteristic time scale to the dynamical system.

To check the quality of a theoretical description of Min oscillations, quantitative comparison with experiments is necessary. In this chapter, we pinpoint two characteristic time scales of MinD and of MinE dynamics, using fluorescence correlation spectroscopy in living *E. coli* cells [46]. Especially, we determine the mobility of MinD and MinE in the cytoplasm. Our work is the first study which determines parameters of the Min system *in vivo*.

There are several techniques to measure protein mobilities using fluorescence microscopy. Direct measurements of the displacement of individual proteins have been used to determine the mobility of membrane proteins in the bacterium *Caulobacter crescentus* [62]. Fluorescence recovery after photobleaching (FRAP), where the fluorescent proteins present in a defined region are bleached and the recovery of the fluorescence is recorded, was used to measure the diffusion constants of cytoplasmic proteins [63]. Fluorescence correlation spectroscopy (FCS) records the fluorescence intensity emitted from an illuminated region in the sample containing fluorescent particles [64]. The fluctuations of the respective intensity gives information about dynamic processes in which the fluorescent particles are involved. To deduce dynamical parameters from the system, the autocorrelation function of intensity fluctuations is calculated. Fitting this to the autocorrelation curve, theoretically expected for the process under study, yields the searched-for values. In bacteria, FCS was used to measure the concentration of phosphorylated CheY involved in chemotaxis [65]. Also, the transcription activity at the RNA level could be determined [66,67].

We have applied FCS to MinD and MinE tagged to Green Fluorescent Protein (GFP) in *E. coli*. We found that a simple diffusion process cannot account for the measured autocorrelation curves. Instead there are two time scales visible, the faster of which can be attributed to cytoplasmic diffusion. The slower time scale could result from diffusion of membrane-bound proteins or from protein exchange between the cytoplasm and the membrane. Independently of the processes responsible for the slower time scale, we determine the diffusion constant of cytoplasmic MinD to be approximately $16\mu\text{m}^2/\text{s}$, while for MinE we find about

$10\mu\text{m}^2/\text{s}$. As a control, we also measured the mobility of GFP and found significant deviations to previous measurements [63]. The origin of the second time scale in the correlation curve of Min proteins could not be uniquely determined by fitting of the data. Assuming that membrane diffusion is at its origin, the membrane diffusion constant was estimated to be $\approx 0.2\mu\text{m}^2/\text{s}$. Considering exchange of particles in the cytoplasm and on the membrane as underlying process, one obtains $\tau_1 \approx 300\text{ms}$ for the time scale associated to membrane attachment and $\tau_2 \approx 100\text{ms}$ for the time scale associated to detachment. Experiments have been performed by Giovanni Meacci and Jonas Ries. Data analysis has been carried out by Jonas Ries and the author.

5.1 Materials and Methods

5.1.1 Strains

EGFP and His6-EGFP were expressed in BL21(DE3)pLysS using the vectors pBAT4 and pET9d, respectively (Novagen, CN Biosciences). GFP-MinD was expressed in JS964 [56] (J. Lutkenhaus, U. Kansas, USA) and WM1255 [68] (W. Margolin, U. Texas, USA), and MinE-GFP in WM1079 [68] (W. Margolin, U. Texas, USA). For details on culturing of the strains see [46].

5.1.2 Optical setup

Fluorescence correlations spectroscopy (FCS) measurements were performed on a LSM Meta 510 system (Carl Zeiss, Jena, Germany) using a $40\times$ NA 1.2 UV-VIS-IR C-Apochromat water immersion objective and a home-built detection unit at the fiber output channel: A bandpass filter (AHF Analyse Technik, Tübingen, Germany) was used behind a collimating achromat to reject the residual laser and background light. Another achromat (LINOS Photonics, Göttingen, Germany) with a shorter focal length was used to image the internal pinhole onto the aperture of the fiber of the avalanche photo diode (SPCM-CD 3017, PerkinElmer, Boston, MA, USA). The correlation curves were obtained with a hardware correlator Flex 02-01D (correlator.com, Bridgewater, NJ, USA). The position for FCS measurements could be selected accurately in a corresponding laser scanning microscope (LSM) image. The waist w_0 of the detection volume was determined in calibration measurements with the fluorescent dye Alexa Fluor 488 diffusing freely in water to be $w_0 = 157 \pm 12\text{nm}$.

5.1.3 Theoretical autocorrelation curves

The experimental autocorrelation curves were analyzed by fitting autocorrelation curves expected for different processes. The detection volume in the measurement has an ellipsoidal shape, rotationally symmetric around the z-axis, which is supposed to be orthogonal to the focal plane. Since the extension in z-direction of the detection volume is larger than the diameter of the bacterium, the cytosolic diffusion can be approximated to occur in two dimensions. Fitting with a more refined model taking into account the geometry of the detection volume in the

bacterium [69] did not significantly change the values we obtained assuming a planar disk shape in two dimensions.

Two diffusing species. For two independent species diffusing with respective diffusion constants D_1 and D_2 the correlation curve is [64,70]

$$G_{\text{diff}}(\tau) = \frac{1}{N_1 + N_2} \left\{ F \frac{1}{1 + \tau/\tau_1} + (1 - F) \frac{1}{1 + \tau/\tau_2} \right\} \quad (5.1)$$

Here, the number fraction of particles of one species is given by $F = N_1/(N_1 + N_2)$, where N_1 and N_2 are the average numbers of particles of the different species in the detection volume. The characteristic relaxation times τ_1 and τ_2 are linked to the respective diffusion constants and the width w_0 of the detection volume through $\tau_i = w_0^2/(4D_i)$, $i = 1, 2$.

Exchange between mobile and immobile state. For particles changing between a mobile state (diffusion constant D) and an immobile state, we assume the following reaction kinetics for the fraction F of the mobile state $dF/dt = -F/\tau_1 + (1 - F)/\tau_2$, where τ_1 and τ_2 are the cytosolic and membrane residence times, respectively. Thus, if exchange between the mobile and immobile population is in equilibrium, we have $\tau_2 = (1 - F)\tau_1/F$, i.e. F and τ_1 can be considered as independent variables whereas τ_2 is a function of F and τ_1 . The autocorrelation of the fluctuations has the form [64,70]

$$G_{\text{ex}}(\tau) = \frac{(2\pi)^{-3}}{(N_1 + N_2)} \int_0^\infty dk k e^{(-\frac{w_0^2}{4}(k_x^2 + k_y^2))} \times \quad (5.2)$$

$$\sum_{j=1,2} (X_{1j} + X_{2j})(X_{j1}^{-1} F + X_{j2}^{-1} (1 - F)) e^{\lambda_j \tau}$$

$$= \frac{(2\pi)^{-2} w_0^2}{(N_1 + N_2)} \int_0^\infty dk k e^{-\frac{w_0^2}{4}(k_x^2 + k_y^2)} \{A_1 e^{\lambda_1 \tau} + A_2 e^{\lambda_2 \tau}\} \quad (5.3)$$

where $\lambda_{1,2}$ are the eigenvalues of the matrix of the reaction kinetics of the proteins in Fourier space

$$\mathbf{M}_{\text{react}} = \begin{pmatrix} -D k^2 - \tau_1^{-1} & \tau_2^{-1} \\ \tau_1^{-1} & -\tau_2^{-1} \end{pmatrix}. \quad (5.4)$$

Therefore, we obtain for the eigenvalues

$$\lambda_{1,2} = -\frac{(Dk^2 + \tau_1^{-1} + \tau_2^{-1})}{2} \pm \frac{\sqrt{(Dk^2 + \tau_1^{-1} + \tau_2^{-1})^2 - 4Dk^2/\tau_2}}{2}.$$

\mathbf{X} is the matrix obtained by combining the eigenvectors of $\mathbf{M}_{\text{react}}$ as column vectors

$$\mathbf{X} = \begin{pmatrix} \lambda_1 + \tau_2^{-1} & \lambda_2 + \tau_2^{-1} \\ \tau_1^{-1} & \tau_1^{-1} \end{pmatrix}.$$

Its inverse is readily calculated to be

$$X^{-1} = \frac{\tau_1}{(\lambda_1 - \lambda_2)} \begin{pmatrix} \tau_1^{-1} & -(\lambda_2 + \tau_2^{-1}) \\ -\tau_1^{-1} & (\lambda_1 + \tau_2^{-1}) \end{pmatrix}.$$

Inserting these expressions into the Equation (5.2), we can calculate the factors A_1 and A_2

$$A_{1,2} = \{ \lambda_{2,1} + Dk^2\tau_1/(\tau_1 + \tau_2) \} / (\lambda_{2,1} - \lambda_{1,2}).$$

Anomalous diffusion. For a single species diffusing anomalously in two dimensions the autocorrelation function is given by [71]

$$G_a(\tau) = \frac{1}{N} \frac{1}{1 + \left(\frac{\tau}{\tau_a}\right)^\alpha} \quad (5.5)$$

Here, $\tau_a^{-\alpha} = 4\Gamma/w_0^2$, where the anomalous exponent α governs the spreading of an initially localized distribution $\langle x^2 \rangle \sim t^\alpha$ and where Γ is the anomalous transport coefficient.

5.2 Data analysis

The correlation curves were fitted in the time interval $\tau \in [2\mu\text{s}, 1\text{s}]$. To this end, a weighted nonlinear least-squares fit algorithm was programmed in Matlab. Weights were determined according to the noisiness of the data, in a moving time window. Curves were selected automatically based on convergence of the fit algorithm and goodness of the fit ($\chi^2 < 1.2$ for EGFP and $\chi^2 < 1.4$ for Min proteins). For measurements on the Min proteins, up to 40 measurements have been performed subsequently on a single cell. By the course of the intensity in the detection volume during subsequent measurements, data could be sorted according to low and high intensity states. This was done by hand-selection. Only those measurements were kept where the cell was in a quasi-steady state. Since the detection volume of the measurement was small ($w_0 \approx 157\text{nm}$) compared to the wavelength of the standing MinD wave in the bacterium, measurements with the cell in a quasi-steady state were characterized by a roughly constant fluorescence intensity recording, see Figures 5.3 and 5.6a.

In order to see the differences of the fits to the theoretical correlation curves (5.1) and (5.3), and to compare the resultant fit parameters with the actual parameter values, we applied the fitting algorithm to simulated data. These were produced by simulating the anticipated reaction kinetics of 1000 particles in a two-dimensional box of $4\mu\text{m}$ length and $1\mu\text{m}$ width. Particles were counted in a disk-shaped area with Gaussian shape and a waist of 160nm . We simulated three different kinetic scenarios of a system with one type of fluorophore and two characteristic time scales. First, particles were assumed to be either fast or slowly diffusing with diffusion constants $D_1 = 17\mu\text{m}^2/\text{s}$ or $D_2 = 0.15\mu\text{m}^2/\text{s}$. The fraction of fast diffusing particles was set to $F = 0.75$. In the second scenario, particles were either in a mobile state diffusing with $D = 17\mu\text{m}^2/\text{s}$ or in an immobile state. The fraction of mobile particles was again set to $F = 0.75$. The transition rate from the mobile to the immobile state was chosen as $\omega_1 = 3.33\text{s}^{-1}$, and for the reverse process $\omega_2 = 10\text{s}^{-1}$. In the third scenario, the processes from the first and the second scenario are simulated simultaneously, with the same parameters. Here, slow diffusion and binding happen on a comparable time scale. Results obtained from a simulation time of 100s with time step $\Delta t = 10^{-5}\text{s}$ are shown in Figure 5.1. The analytical expressions of the correlation curves (5.1) (in blue)

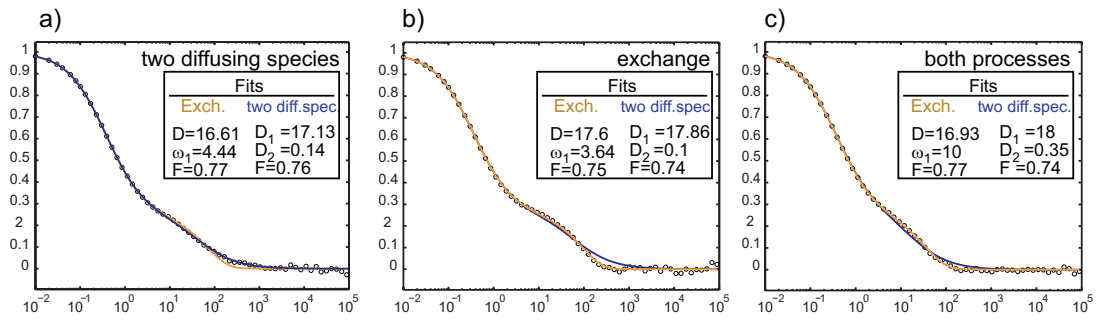


Figure 5.1: Simulated correlation curves for different kinetic processes anticipated. a) Two independent diffusing particle species. Diffusion constants are $D_1 = 17\mu\text{m}^2/\text{s}$ and $D_2 = 0.15\mu\text{m}^2/\text{s}$. The fraction of fast diffusion particles is $F = 0.75$. b) Exchange between a mobile and an immobile state. The fraction of mobile particles is $F = 0.75$ diffusing with $D = 17\mu\text{m}^2/\text{s}$. The transition rate from the mobile to the immobile state was chosen as $\omega_1 = 3.33\text{s}^{-1}$, and for the reverse process $\omega_2 = 10\text{s}^{-1}$. c) Processes from a) and b) occurring at the same time. The analytical expressions for the correlation curves (5.3) (in yellow) and (5.1) (in blue) were fitted to the data. The respective fit parameters are shown in the insets. Deviations of the fit are mostly due to boundary effects which are not captured by the theoretical autocorrelation curve.

and (5.3) (in yellow), corresponding to the first and the second kinetic scenario respectively, were fitted to the data and the fit parameters are shown in the insets. In the data sets of Fig. 5.1a and b, the fit quality clearly improves for the correct theoretical correlation curve fitted. In Fig. 5.1c, the exchange model gives the better fit to the data although neither of the fitted curves is the correct model. The obtained exchange rate ω_1 or diffusion constant D_2 , respectively, overestimate the correct values. This is because exchange and slow diffusion are happening at the same time giving rise to a faster decay of correlations compared to only one process taking place. Deviations from the correct theoretical correlation curves with the exact parameters are due to finite simulation times and most of all due to boundary effects.

In analogy to the experimental measurements, simulations were also performed with time step $\Delta t = 10^{-7}\text{s}$ for a total period of 5s. For the kinetic scenarios one and two (two diffusing species and exchange with an immobile reservoir), hundred simulations have been performed with different seeds of the random number generator. The resultant autocorrelation curves were fitted to the theoretical autocorrelation curves (5.1) and (5.3). The mean values of the obtained fit parameters are given in Table 5.1. They show that fitting of the correct and the false model to the data give approximately the correct values for the fast diffusion constant and the fraction of fast diffusing particles. Deviations from the theoretical correlation curves with the exact parameter values are due to the relatively short simulation time of 5s and due to effects of the system boundary.

<i>simulation</i> <i>type</i>	two species fit			exchange model fit		
	D_1 ($\mu\text{m}^2/\text{s}$)	D_2 ($\mu\text{m}^2/\text{s}$)	F	D ($\mu\text{m}^2/\text{s}$)	ω_1 (s^{-1})	F
two species	17.2 ± 0.6	0.18 ± 0.07	0.77 ± 0.04	16.7 ± 0.4	4.9 ± 1.6	0.78 ± 0.04
exchange	17.6 ± 0.42	0.1 ± 0.03	0.76 ± 0.04	17.3 ± 0.4	3.1 ± 0.8	0.77 ± 0.04

Table 5.1: Results from fits of simulated data in analogy to experimental measurements. Simulations were performed for a time period of 5s with a time step of $\Delta t = 10^{-7}\text{s}$. Two scenarios have been considered: In the first scenario, two particle species diffuse with distinct diffusion constants. In the second scenario, particles diffuse and exchange with an immobile particle reservoir. In both cases, hundred simulations have been performed. The data have been fitted to the theoretical correlation curves of both scenarios. The obtained mean of the fit parameters and the associated standard deviation are given above.

5.3 Measurement results and discussion

EGFP. First, the autocorrelation of the fluorescence fluctuations of Enhanced Green Fluorescent Protein (EGFP) was measured in living *E. coli*. A typical correlation curve is depicted in Figure 5.2a. The correlation curves of GFP fluorescence were fitted to the theoretically expected correlation for one diffusing particle species in two dimensions (see (5.1), with $F=1$). In view of the data analysis for fluorescent MinD and MinE, fits were also performed for the autocorrelation curves G_{diff} with F as fit parameter, G_{ex} and G_{a} , see Section 5.1.3. A histogram of the diffusion constants obtained by fitting G_{diff} to 1021 curves is presented in Figure 5.2b. The histogram is well described by a log-normal distribution with a geometric mean of $D = 17.9_{-3.4}^{+4.3}\mu\text{m}^2/\text{s}$. Within the accuracy of our measurements, different cells give the same value for the EGFP diffusion constant. The fraction of the fast component was $F = 0.96 \pm 0.03$, indicating that most of the dynamics is due to fast diffusion. We arrived at the same conclusion using G_{ex} for the data analysis, see Table 5.2. Figure 5.2c presents a histogram of anomalous exponents from analyzing the same curves using G_{a} .

The values of the diffusion constants are surprisingly large compared to previous measurements of the EGFP diffusion constant using FRAP. In [63], a value of $D_{\text{GFP}} \simeq 7.5\mu\text{m}^2/\text{s}$ was obtained. There, it was also found that the diffusion constant can be changed significantly by adding a His-tag. We examined His6-EGFP expressed in the same strain as was used for the measurement of EGFP mobility. Using either G_{diff} or G_{ex} defined in Equations (5.1) and (5.3), respectively, we found a decrease in the diffusion constant of about 20% compared to EGFP. Based on the anomalous diffusion model, we found a slightly reduced value for the anomalous mobility, $\Gamma = 5.6_{-2.8}^{+5.7}\mu\text{m}^2/\text{s}^\alpha$, while the anomalous exponent remained the same, $\alpha = 0.88 \pm 0.1$.

Quasi-steady states during Min oscillations. Analysis of fluorescence fluctuations requires a well-defined average state. Apparently, this is not the case for the Min system, which is dynamic and oscillates with a period of about 80s [13,19,20], see Figure 5.3a. However, there are regions in the bacterium in which the fluorescence signal is quasi-stationary for about 10s. In Figure 5.3b, the fluorescence

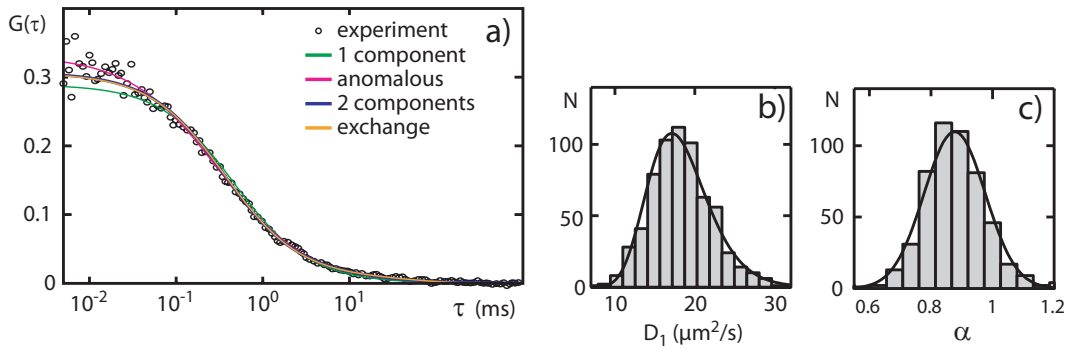


Figure 5.2: Diffusion coefficients of EGFP in *E. coli* measured by fluorescence correlation spectroscopy. a) Typical autocorrelation curve $G(\tau)$ for EGFP (black circles) and non-linear least square fits of correlation curves expected for different processes. Green: diffusion, see (5.1) with $F = 1$, gives $D = 12.9 \pm 2.3 \mu\text{m}^2/\text{s}$ with $\chi^2 = 1.6$. Pink: anomalous diffusion, see eq:singleanodiff), yields $\alpha = 0.83 \pm 0.01$ and $\Gamma = 4.7 \pm 0.75 \mu\text{m}^\alpha/\text{s}$ with $\chi^2 = 1.1$. Blue: two independent diffusing populations, see (5.1), yields $D_1 = 17.7 \pm 3.6 \mu\text{m}^2/\text{s}$, $D_2 = 0.3 \pm 0.2 \mu\text{m}^2/\text{s}$, and $F = 0.96 \pm 0.01$ with $\chi^2 = 1.1$. Yellow: exchange between a mobile and an immobile state, see (5.3), yields $D = 14.8 \pm 2.8 \mu\text{m}^2/\text{s}$, $\tau_1 = 2.3 \pm 1.0\text{s}$, and $F = 0.97 \pm 0.004$ with $\chi^2 = 1.1$. No significant autofluorescence of cells was detected, but there was a non-correlated background of 8kHz from the medium. b) Histogram of diffusion coefficients obtained from fitting G_{diff} to 1020 measurements. Solid line: log-normal distribution with geometric mean $D = 17.9_{-3.4}^{+4.3} \mu\text{m}^2/\text{s}$. c) Histogram of anomalous exponents from fitting G_a to the same curves as in (b). Solid line: normal distribution with mean $\alpha = 0.88$ and variance $\sigma_\alpha^2 = 0.09$. In (b) and (c) only fits with $\chi^2 < 1.2$ were considered.

intensity in a confocal volume positioned in one cell half is presented. Phases of high and low constant fluorescence occur as well as phases of strongly varying fluorescence. These phases reflect the dwelling of MinD in one cell half for a large fraction of a half-period as well as the comparatively rapid transition to the opposite cell half. Figure 5.3c displays the fluorescence intensity along the bacterial long axis for six different times separated by 2s. The intensity variations during this period are less than 5%. Fluorescence profiles in cross-sections perpendicular to the long axis also show only moderate fluctuations, Figure 5.3d,e. The form of the low intensity profile shows a relatively smooth plateau whereas the high intensity profile exhibits two peaks. This results from a low fraction of membrane-bound MinD in the low-intensity region and a high fraction in the high-intensity region [20]. The fluorescence profiles for different times indicate that the respective amounts of cytoplasmic and membrane-bound MinD are quasi-stationary within the 10s shown.

GFP-MinD. MinD-motility was measured in the strain JS964. For the FCS analysis only fluorescence curves taken from regions in quasi-steady state were considered. Every individual measurement lasted for 5s. A typical autocorrelation curve is shown in Figure 5.4a. From the graph it is obvious that two distinct time scales are present. We checked, that neither of them is due to bleaching. To this end, GFP was adsorbed on an untreated cover slip. Then intensity traces and correlation curves were recorded for this immobilized GFP. The intensity curves

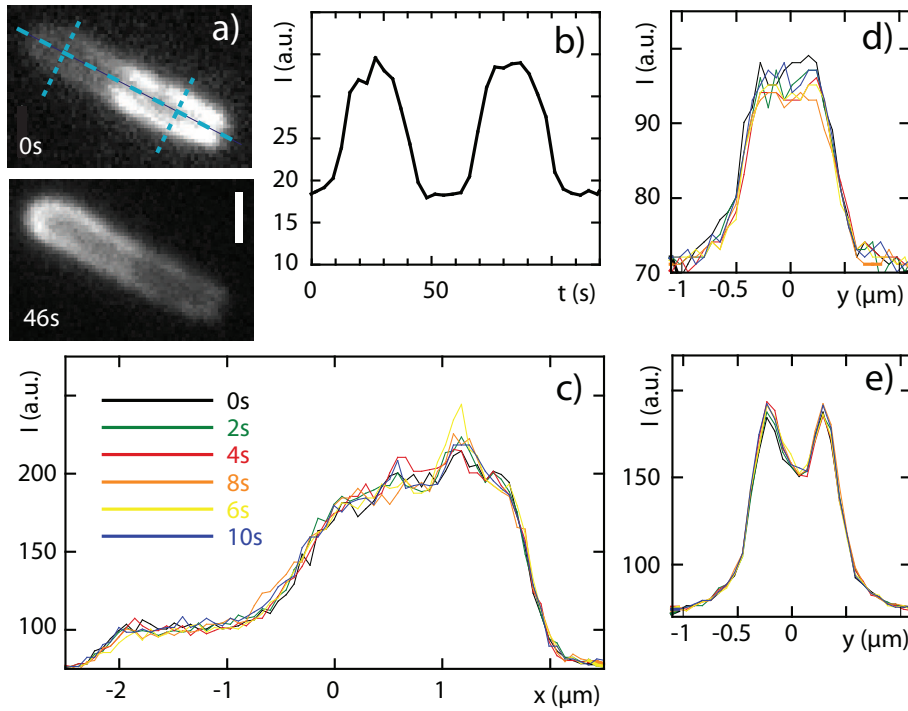


Figure 5.3: Quasi steady states. a) GFP-MinD fluorescence in *E. coli* at different phases of the oscillation cycle. Scale bar: $1\mu\text{m}$. b) Fluorescence intensity in a confocal volume located in one cell half as a function of time. Oscillations with a period of 60s are clearly seen. Around states of maximal and minimal intensity, time-intervals of roughly constant fluorescence intensity can be detected. c,d,e) Fluorescence intensity along the long axis (c) and the cross-sections (d, e) indicated in (a) for six different times separated by 2s each. The curves vary around a quasi-stationary mean profile. The differences in the cross-section profiles (d) and (e) reflect the different fractions of membrane-bound proteins in the low- and high-intensity phases in a cell half.

could be fitted to an exponential curve with a decay time of a few seconds, see Figure 5.4a inset¹¹. The corresponding FCS curves show a decay with a similar characteristic time. These times are larger than the two time scales apparent in Figure 5.4a. Furthermore, the correlation curves were largely independent of the excitation intensity (data not shown). We conclude that neither of the time scales is due to bleaching of immobilized molecules.

One of the time scales detectable in Figure 5.4a is readily attributed to MinD diffusing freely in the cytosol. The existence of MinD bound to the membrane suggests two obvious candidate processes leading to the other time scale visible in the correlation curves. First of all, it could be attributed to diffusion of MinD on the membrane. Secondly, it could result from the exchange of MinD between the membrane and the cytosol. We analyzed the measured correlation curves using separately the two different models. Of course, the two processes are not mutually exclusive. It would thus be desirable to analyze the correlation curves using a model that accounts for diffusion on the membrane as well as for binding and

¹¹Some measurements indicated a bi-exponential decay with characteristic times of 0.8s and 4s.

unbinding. However, the expected correlation curve differs only by small amounts from the curves for either of the two alternatives separately (see also Fig. 5.1). The accuracy of our measurements does not allow distinguishing between them. If MinD is incorporated into helices [30] a significant fraction of membrane-bound MinD might be immobile. Since these molecules do not contribute to fluctuations in the average fluorescence intensity, FCS cannot detect them.

We first present the results assuming two states of different mobility. Figure 5.4b displays the two diffusion constants obtained from fits of G_{diff} (5.1) to different correlation curves measured on a single cell. We interpret the faster diffusion constant to represent the mobility of cytosolic MinD. It is of the same order as the diffusion constant of EGFP. The smaller diffusion constant is interpreted as resulting from the mobility of membrane-bound MinD. This is supported by the estimated value of the fraction of the fast component: In agreement with the measurements of the cross-sections, Figure 5.3d, e, the fraction of fast moving proteins is larger in the low-intensity regions than in the high-intensity regions, see Figure 5.4c. Histograms of fast and slow diffusion constants summarizing series of measurements on different cells are shown in Figure 5.4d, e. Both histograms are well described by a log-normal distribution. The geometric mean value for the fast diffusion constant is $D_1 = 17.0_{-2.5}^{+3.0} \mu\text{m}^2/\text{s}$. For the slow diffusion constant we find $D_2 = 0.17_{-0.08}^{+0.14} \mu\text{m}^2/\text{s}$. This value is one order of magnitude higher than the diffusion constant for the transmembrane histidine kinase PleC measured by single protein tracking in *C. crescentus* [62]. PleC is a transmembrane protein whereas MinD binds to the polar heads of the lipids forming the membrane. Therefore, the values are compatible. No correlation could be detected between the values of the fast and slow diffusion constants (data not shown). Separating the curves into those with low and high average intensity does not reveal significant differences between the respective fast and slow diffusion constants, see Table 5.2. For the membrane diffusion constant, a difference would be plausible e.g. due to crowding and particle interactions in the regime of higher concentrations. In the low-intensity regions, however, the fraction $F = 0.81 \pm 0.1$ of the fast-diffusing component is larger than in the high-intensity regions, where $F = 0.71 \pm 0.1$. The difference in the fractions is more pronounced when averaging over several measurements on a single cell than when averaging over measurements on different cells, Figure 5.4c. This presumably reflects different protein concentrations in different cells or a different position of the detection volume in the cells during measurements.

The same data were analyzed based on the exchange of MinD between a mobile (cytosolic) state and an immobile (membrane-bound) state, disregarding diffusion of membrane-bound proteins. As suggested by the cross-section profiles, Figure 5.3d, e, we assume the average fraction of mobile molecules to be constant during one measurement. In that case, the residence times τ_1 and τ_2 of MinD in the mobile and immobile states, respectively, are related to the fraction F of mobile molecules by $F = \tau_1/(\tau_1 + \tau_2)$. The results obtained from analyzing the same curves as in Figure 5.4b, c are displayed in Figure 5.5a, b. The diffusion constants are in the same range as the values of the fast diffusion constant obtained above. The same holds for the value of the mobile fraction F . Histograms of the diffusion constant and the residence time in the mobile state are presented in Figure 5.5c, d. Differences in the values for low- and high-intensity regions are not significant,

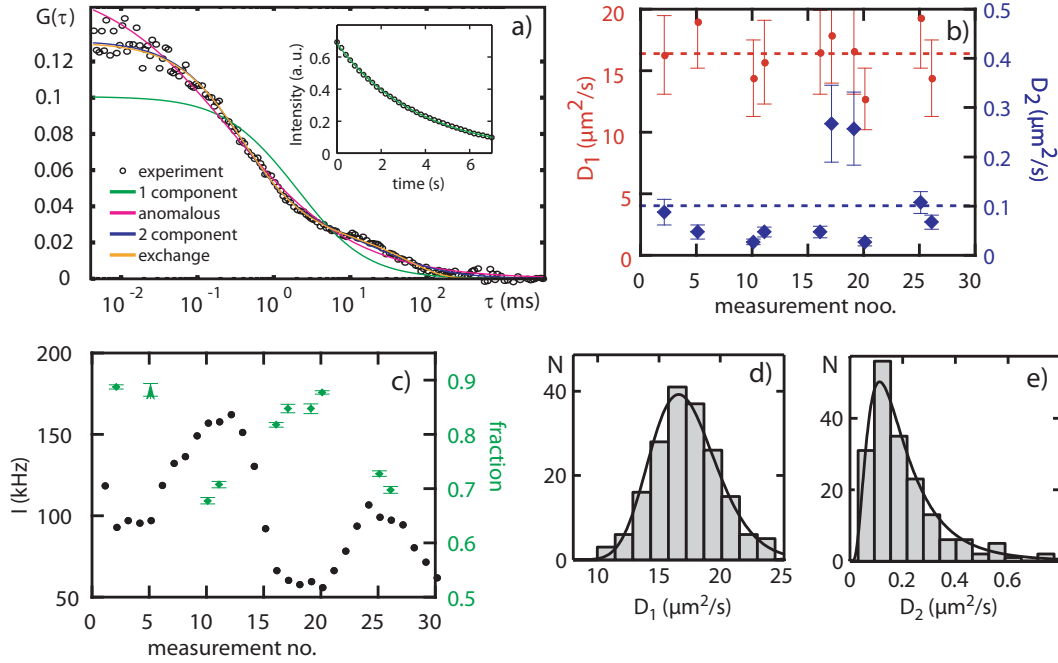


Figure 5.4: Fluorescence correlation analysis of MinD data — two independent diffusing species. a) Typical autocorrelation curve for GFP-MinD in a region of quasi-steady state (black circles) and non-linear least square fits of different expected correlation curves. Green and pink: diffusion and anomalous diffusion, respectively. Essential features of the experimental curve are missed ($\chi^2 = 5.6$ and 1.8, respectively). Blue: two independent diffusing populations, see (5.1), yields $D_1 = 19.8 \pm 4.3 \mu\text{m}^2/\text{s}$, $D_2 = 0.11 \pm 0.02 \mu\text{m}^2/\text{s}$, and $F = 0.74 \pm 0.01$ with $\chi^2 = 1.1$. Yellow: exchange between a diffusing and an immobile state yields $D = 15.7 \pm 3.1 \mu\text{m}^2/\text{s}$, $\tau_1 = 302 \pm 25 \text{ms}$, and $F = 0.83 \pm 0.004$ with $\chi^2 = 1.18$. b) Apparent diffusion constants D_1 and D_2 for 10 curves admitting a good fit ($\chi^2 < 1.4$) among 30 successive measurements on a single cell. The mean values are $D_1 = 16.4 \pm 2.1 \mu\text{m}^2/\text{s}$ (mean \pm SD) and $D_2 = 0.1 \pm 0.09$ (mean \pm SD). c) Fluorescence intensity and fast fraction for the same measurements as in (b). The fast fraction is higher for low intensities. d,e) Histograms of the diffusion constants. Only curves with quasi-steady fluorescence intensity and a fit quality of $\chi^2 < 1.4$ were retained. Solid lines: log-normal distributions with geometric means $D_1 = 17.0^{+3.0}_{-2.5} \mu\text{m}^2/\text{s}$ and $D_2 = 0.17^{+0.14}_{-0.08} \mu\text{m}^2/\text{s}$.

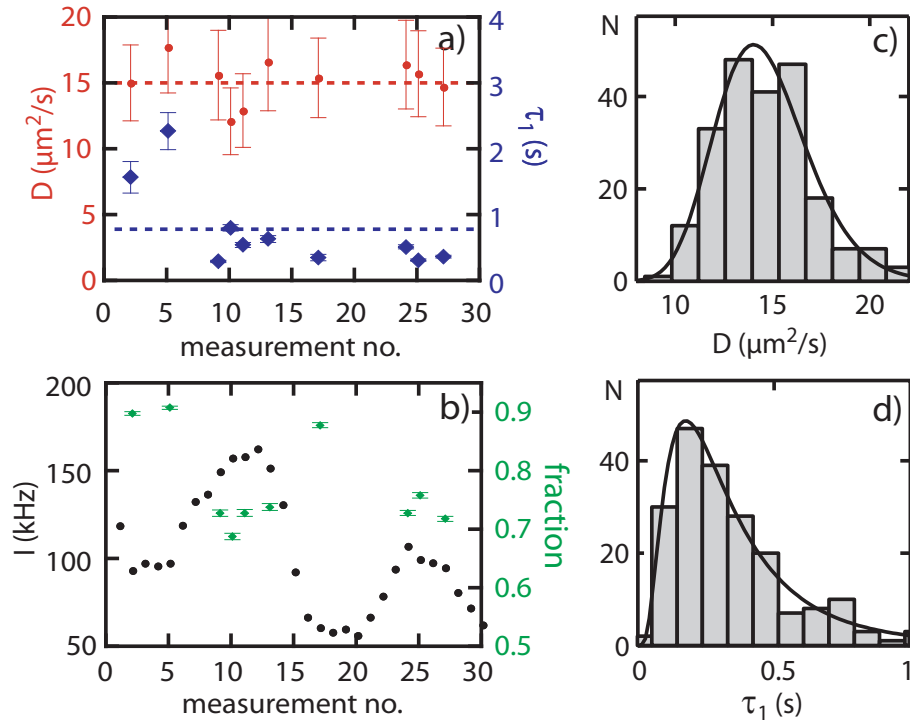


Figure 5.5: Fluorescence correlation analysis of MinD data — exchange between diffusing and immobile state. a) Apparent diffusion constants and residence times in the mobile state for the same 30 successive measurements on a single cell as in figure 5.4b,c. The mean values are $D = 15.0 \pm 1.9 \mu\text{m}^2/\text{s}$ and $\tau_1 = 783 \pm 651 \text{ms}$ (mean \pm SD). b) Fluorescence intensity and mobile fraction for the same measurements as in (a). The mobile fraction is higher for low intensities. c,d) Histograms of the diffusion constants and residence times obtained from the same 2017 measurements as in figure 5.4d,e. Solid lines: log-normal distributions with geometric means $D = 14.4^{+2.6}_{-2.2} \mu\text{m}^2/\text{s}$ and $\tau_1 = 322^{+422}_{-183} \text{ms}$.

although the residence times are on average larger in the low-intensity regions, see Table 5.2. The measurements were repeated using a different strain (WM1255). The average cytosolic diffusion constants were smaller in this strain, while the average residence time were a little larger, see Table 5.2. In view of the broadness of the distributions, however, the differences were not significant.

MinE-GFP. For measuring the mobility of MinE, the same strategies were applied as for MinD. An example of a quasi-steady state of the MinE distribution is shown in Figure 5.6a. As for MinD, two distinct relaxation times can be detected in the correlation curves. We analyzed these curves using the same theoretical descriptions as for MinD. Histograms of the two different diffusion constants and of the diffusion constant together with the residence time in the mobile state, respectively, are presented in Figure 5.6b-e. As before, the histograms are well described by log-normal distributions. Assuming two independent populations with different mobilities, we find $D_1 = 11.2^{+2.9}_{-2.3} \mu\text{m}^2/\text{s}$ and $D_2 = 0.20^{+0.23}_{-0.11} \mu\text{m}^2/\text{s}$. The fraction of the faster diffusion population is $F = 0.79 \pm 0.10$. While cytosolic diffusion of MinE is thus smaller than for MinD, the diffusion constants for membrane-bound MinD and MinE are the same. This is compatible with MinE being bound to MinD on the membrane. Assuming the other model, we obtain

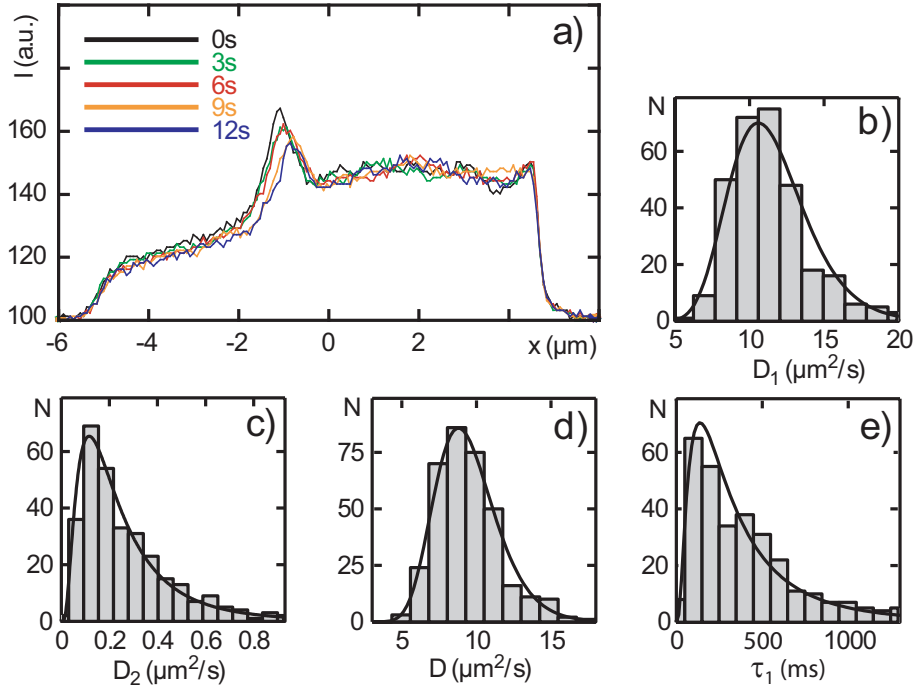


Figure 5.6: Fluorescence correlation analysis of MinE. a) Quasi-steady state of the MinE distribution along a cell's long axis. Five curves separated each by 3s vary around a mean profile. An accumulation of MinE close to the cell center, commonly known as MinE ring, can clearly be recognized. It moves slowly to one cell pole. b,c) Histograms of the diffusion constants assuming two independent diffusing species. Only curves with quasi-steady fluorescence intensity and a fit quality of $\chi^2 < 1.4$ were retained. Solid lines: log-normal distributions with geometric means $D_1 = 11.2_{-2.3}^{+2.9} \mu\text{m}^2/\text{s}$ and $D_2 = 0.20_{-0.11}^{+0.23} \mu\text{m}^2/\text{s}$. d,e) Histograms of the diffusion constants and residence times obtained from the same measurements as in (b,c) assuming exchange between a diffusing and an immobile state. Solid lines: log-normal distributions with geometric means $D = 9.3_{-1.9}^{+2.3} \mu\text{m}^2/\text{s}$ and $\tau_1 = 396_{-274}^{+888} \text{ms}$.

for MinE $D = 9.3_{-1.9}^{+2.3} \mu\text{m}^2/\text{s}$ and $\tau_1 = 396_{-274}^{+888} \text{ms}$. The mobile fraction is in this case $F = 0.86 \pm 0.09$. Separating the curves into those from a low-intensity and those from a high-intensity phase, no significant differences between neither the values of the diffusion constants nor the residence times in the different phases can be detected, see Table 5.2.

Discussion

In this chapter, we have presented the first measurements of dynamic parameters of the Min system *in vivo*. For this, we have used Fluorescence correlation spectroscopy in living *E. coli*. The possibility to apply FCS relies on the existence of quasi-stationary steady states in some regions of the bacterium for time intervals of at least 10s, see Figure 5.3c-e and 5.6a. Our correlation data clearly show the existence of more than one relaxation time. We interpret the faster component to result from diffusion of cytosolic proteins. The second time scale could result

from (i) the mobility of proteins in the membrane-bound state or alternatively from (ii) transitions between the cytoplasm and the membrane. We find that all in all both models fit equally well to the data, although there can be significant differences in the fit quality for individual curves. Using either models for analyzing the experimental data, we find values around $16\mu\text{m}^2/\text{s}$ and $10\mu\text{m}^2/\text{s}$ for the respective cytosolic diffusion constants of GFP-MinD and MinE-GFP. Therefore, a cytosolic MinD molecule explores the volume of a $4\mu\text{m}$ long cell within roughly a second. Cytosolic MinE, which readily forms dimers, needs about 1.5s, i.e. only slightly longer.

(i) Assuming slower diffusion on the membrane as second time scale.

The diffusion constants we obtained for membrane-bound proteins are about two orders of magnitude smaller than the cytosolic diffusion constants. For membrane-bound MinD, it would be of the same order as the value assumed in the AC model studied in [13].

(ii) Assuming exchange with the membrane-bound state as second time scale.

For the average residence time of MinD in the cytoplasm, we find a value of about 300ms. The residence time of MinE in the cytosol is somewhat larger than for MinD which is compatible with the fact that MinE requires MinD as a substrate in order to bind to the membrane. From the residence time in the cytosol and the cytosolic diffusion constants, we can determine the diffusion length $\ell = (Dt)^{1/2}$. This is the average distance traveled by a cytosolic molecule. For MinD and MinE we find $\ell \simeq 2\mu\text{m}$. This value would indicate that in small bacteria of about $2\mu\text{m}$ in length, the distribution of cytosolic MinD and MinE should be homogenous.

Comparing the different values measured in high- and low-intensity phases, respectively, we find that the fraction of cytosolic proteins is always larger in the low-intensity phases. This is not only an effect due to averaging but is also present in individual cells, see Figs. 5.4c and 5.5b. Based on the cooperative attachment (CA) models, a shorter cytosolic residence time of MinD in the high-intensity phase than in the low-intensity phase is expected. Indeed, on average, our measurements confirm this expectation, see Table 5.2. Caution should be taken, though, because the error bars are quite large. The average residence time of MinE in the cytosol, too, depends on being in a high- or low-intensity phase. This is expected since a higher number of membrane-bound MinD should lead to a higher rate of MinE binding to the membrane.

			two species				exchange			
	N_{tot}	N_{sel}	D_1 ($\frac{\mu\text{m}^2}{\text{s}}$)	D_2 ($\frac{\mu\text{m}^2}{\text{s}}$)	F	N	D ($\frac{\mu\text{m}^2}{\text{s}}$)	τ_1 (ms)	F	N
EGFP ^a	1021		17.9 ^{+4.3} _{-3.4}	0.22 ^{+0.51} _{-0.16}	0.96 ^{+0.03} _{-0.03}	652	17.9 ^{+4.4} _{-3.6}	1100 ⁺⁷¹⁵⁰ ₋₉₅₃	0.97 ^{+0.04} _{-0.04}	690
His6-EGFP ^a	555		14.9 ^{+3.7} _{-3.0}	0.14 ^{+0.53} _{-0.11}	0.96 ^{+0.04} _{-0.04}	214	15.0 ^{+5.7} _{-4.1}	1870 ⁺¹²²⁰⁰ ₋₁₆₂₀	0.97 ^{+0.05} _{-0.05}	220
GFP-MinD ^b	2017	438	17.0 ^{+3.0} _{-2.5}	0.17 ^{+0.14} _{-0.08}	0.77 ^{+0.11} _{-0.11}	181	14.4 ^{+2.6} _{-2.2}	322 ⁺⁴²² ₋₁₈₃	0.79 ^{+0.11} _{-0.11}	217
GFP-MinD ^b l.i.		191	16.7 ^{+3.1} _{-2.6}	0.18 ^{+0.16} _{-0.08}	0.81 ^{+0.10} _{-0.10}	105	14.7 ^{+3.0} _{-2.5}	464 ⁺⁶⁴³ ₋₂₇₀	0.86 ^{+0.08} _{-0.08}	104
GFP-MinD ^b h.i.		247	17.4 ^{+2.6} _{-2.3}	0.15 ^{+0.11} _{-0.06}	0.71 ^{+0.10} _{-0.10}	76	14.1 ^{+2.2} _{-1.9}	230 ⁺²⁰⁹ ₋₁₁₀	0.73 ^{+0.10} _{-0.10}	113
GFP-MinD ^c	738	102	14.3 ^{+2.9} _{-2.4}	0.16 ^{+0.18} _{-0.08}	0.80 ^{+0.08} _{-0.08}	50	12.4 ^{+1.8} _{-1.6}	522 ⁺⁷²¹ ₋₃₀₃	0.84 ^{+0.07} _{-0.07}	43
MinE-GFP ^d	1807	528	11.2 ^{+2.9} _{-2.3}	0.20 ^{+0.23} _{-0.11}	0.79 ^{+0.10} _{-0.10}	307	9.3 ^{+2.3} _{-1.9}	396 ⁺⁸⁸⁸ ₋₂₇₄	0.86 ^{-0.09} _{+0.09}	350
MinE-GFP ^d l.i.		310	11.4 ^{+2.8} _{-2.3}	0.21 ^{+0.25} _{-0.11}	0.82 ^{+0.09} _{-0.09}	198	9.6 ^{+2.5} _{-2.0}	478 ⁺¹¹⁰⁵ ₋₃₃₄	0.88 ^{-0.08} _{+0.08}	223
MinE-GFP ^d h.i.		218	10.9 ^{+3.1} _{-2.4}	0.20 ^{+0.20} _{-0.10}	0.75 ^{+0.11} _{-0.11}	109	8.8 ^{+1.9} _{-1.5}	285 ⁺⁵⁴² ₋₁₈₇	0.81 ^{-0.09} _{+0.09}	127

Table 5.2: Mobility of EGFP, His6-EGFP, GFP-MinD, MinE-GFP. For the Min proteins, curves from low-intensity phases (l.i.) and high-intensity (h.i.) phases were analyzed separately. N_{tot} : total number of correlation curves analyzed. D_1 , D_2 : diffusion constants for two independent populations, D , τ_1 : diffusion constant and residence time in the mobile state for proteins switching between a mobile and an immobile state, F : fraction of the faster/mobile population, N : number of curves allowing for a sufficiently good fit. Values were considered only from curves where the fit produced a $\chi^2 < 1.4$ (for EGFP $\chi^2 < 1.2$) and where the intensity was constant. Displayed are the mean values and the 1σ confidence interval. For EGFP, the values of D_1 and D are well described by a log-normal distribution. The values of D_2 and τ_1 scatter extremely and are described neither by log-normal nor by normal distributions. For the Min proteins, the values of D_1 , D_2 , D , and τ_1 are well described by a log-normal distribution. For all strains, the values of F follow a normal distribution. ^aBL21(DE3)pLys, ^bJS964, ^cWM1255, ^dWM1079.

Chapter 6

Min oscillations and cell growth

The Min system of the bacterium *E. coli* exhibits spatiotemporal structures formed by the Min proteins MinC, MinD and MinE. These proteins are confined by the cell membrane and bind to it. Therefore, it is an intuitive guess that the Min patterns change when the cell grows.

Theoretical considerations as well as *in vitro* experiments suggest that the patterns form by self-organization of the Min proteins, see Section 2.3.1, 4.1 and [12]. For a pattern forming dynamical system, it is known that the onset of a bifurcation as well as the shape of the evolving pattern depends on the geometry of the spatial domain [10]. Thus, if Min proteins self-organize a change of the Min pattern is predicted if the cell length changes.

Another aspect of Min patterns and cell growth is that the cell length is associated to the cell age. Passing through the different stages of the cell's life cycle, the parameters which rule the Min dynamics might change over time. Possible candidates for varying parameters are the concentrations of the Min proteins, their concentration ratio, binding and unbinding rates, the ATP hydrolysis rate of MinD, membrane diffusion of MinD etc.

In the literature, data on Min oscillations for cells of different lengths are available. They show that in filamentous *E. coli* cells the Min pattern gains additional concentration maxima, i.e. the number of wave nodes in the standing concentration wave increases [20]. However, to our knowledge, no published data exist on the evolution of Min oscillations in a single, growing cell. Since we were curious how Min patterning changes in a growing cell over time, we performed experiments where we recorded the fluorescence from GFP-MinD in *E. coli* cells over time spans on the order of the cell's life cycle.

For the strain we used, cells were typically $2\mu\text{m}$ long directly after division. Cell division normally occurred at lengths of $4\mu\text{m}$ and longer. During our experimental work, we found interesting new results for the Min patterns in short, newborn *E. coli* cells. Instead of regular Min oscillations they display stochastic switching of Min concentration maxima between the cell poles. We compare these results with predictions of different computational models. Furthermore, we report on Min patterns in filamentous *E. coli* cells which exhibit lengths greater than $4\mu\text{m}$.

6.1 Min pattern in short “newborn” *E. coli* cells

We have systematically studied the Min-protein dynamics as a function of cell length in growing *E. coli* cells with initial cell length shorter than $3\mu\text{m}$. Surprisingly, in cells shorter than $2.5\mu\text{m}$, we found that concentration maxima of MinD switched stochastically from one cell pole to the other. The corresponding spatiotemporal Min pattern evolves in terms of switching between two mirror-symmetric MinD-distributions. Transitions between these two states happened within a few seconds. The residence times in each of the two states varied strongly

and were partly much longer than the times observed for regular Min oscillations. In cells longer than $3\mu\text{m}$, the Min proteins displayed periodic switching between the two states, that is, they show the regular oscillations described in Section 2.1.

6.1.1 Materials and Methods

Data acquisition. We used cells of the *E. coli* strain JS964 containing the plasmid pAM238 encoding for MinE and GFP-MinD [19]. Bacteria were grown overnight in a 3ml LB medium at 37°C with spectinomycin at $25\mu\text{g ml}^{-1}$. Cells were induced with Isopropyl- β -D-thiogalactopyranosid (IPTG). During measurements, the samples were kept at a temperature of 29°C using a Bachhoffer chamber. The fluorescence recordings were taken with an Olympus FV 1000 confocal microscope, at an excitation wavelength of 488nm from a helium laser at low power. We used an Olympus UPLSAPO 60x, NA 1.35 oil immersion objective and recorded a frame every 3s. A measurement lasted 40min. During this period, the focus was manually readjusted at irregular intervals.

In total, we extracted data from 209 cells obtained from 5 different measurements. We extracted data only for cells which, at the beginning of the measurement, were smaller than $3\mu\text{m}$. Cell lengths were determined from differential interference contrast (DIC) images with an accuracy of $\pm 150\text{nm}$ at the beginning and the end of a measurement. The cell length in-between was determined by linear interpolation. Some of the cells in the field of view divided during the measurement time. If division occurred after more than 20min of measurement, they were included in the data analysis. In these cases, fluorescence recordings were used until cell constriction terminated.

Data analysis. Recordings of a fluorescent cell over time was mapped to a time series of a two state system by subtracting the total fluorescence emitted in one cell half from the other. Then, the moving average over four time points was taken in order to reduce noise. The resultant function f is positive when the fluorescence maximum is in one cell half and negative in the opposite case. The zero crossings of f are taken to indicate the times of switching events. Usually, these switching events could also be read off directly from kymographs, see the examples in Fig. 6.1. The residence time in one of the two states is given by the corresponding interswitching interval. To each residence time, we assigned the cell length at the start of the respective residence period. The power spectrum shown in Fig. 6.3c was obtained as follows: We selected cells which matched the constraint of the initial cell length (see figure caption). Then, we used the intensity data f of each selected cell calculated as described above. The Fourier transform of the intensity data set was computed and normalized by division by $\sqrt{\sum_t f_t^2}$, where the iterator t counts the time step. To calculate the power spectrum, the absolute value squared of the Fourier transform was taken. The obtained power spectra were then averaged over the cell ensemble associated to the cell length constraint.

Analysis of the simulation results was done in the same way as for the experimental results. The corresponding function f , though, was obtained by the moving average of five consecutive data points.

6.1.2 Results

In total, we analyzed 209 cells, each of which was tracked for a consecutive time of 40 minutes, see Materials and Methods. During this time, the cells grew for up to $1\mu\text{m}$. Typical kymographs¹² of the fluorescence intensity along the cells' long axis are presented in Fig. 6.1. In cells shorter than $2.5\mu\text{m}$, MinD typically shifted stochastically from one cell half to the other, see Fig. 6.1a. The residence times of MinD in one cell half varied largely in these cells ranging from 35s to more than 40min . Complete switching from one cell half to the other occurred in an interval of less than 15s . The extension of the region covered by MinD in one cell half did not change notably between two exchange events.

For cell lengths between $2.5\mu\text{m}$ and $3\mu\text{m}$, the Min pattern typically shifted from stochastic exchange events to regular oscillations with a period of about 80s , see Fig. 6.1b. The precise lengths at which this transition occurred, differed between cells. In the oscillatory regime, between two switching events, the region covered by MinD first grew monotonically from the cell end and then shrank monotonically towards the same end. Analogously to the stochastic exchange regime, the transition of MinD from one half to the other was fast compared to the oscillation period. In a small number of cells ($N=5$), we observed a shift from regular oscillations to stochastic exchanges. Cells longer than $3.5\mu\text{m}$ invariably displayed regular oscillations, see Fig. 6.1c. The oscillation period typically decreased slightly with increasing cell length. For the cell shown in Fig. 6.1c, the initial period is approximately 87s , while it is approximately 70s at the end.

About 5% of the cells divided during the observation time, see Fig. 6.1d, e. In all these cases, MinD oscillated regularly prior to division. Consistent with our findings in non-dividing cells, the pattern displayed by the Min proteins in the daughter cells immediately after division correlated with their length: daughter cells shorter than $2.5\mu\text{m}$ typically displayed stochastic switching, while the Min proteins mostly oscillated in daughter cells longer than $3\mu\text{m}$. In some cases, however, the two daughter cells showed different MinD patterns, in spite of having equal lengths: while in one daughter MinD oscillated, it showed stochastic shifts in the other. In these cases, judged from the fluorescence intensities, the distribution of MinD between the daughter cells was significantly uneven. Note, that for some cells the brighter daughter displayed oscillations, while for others it was the fainter daughter. From our data, we could not detect a clear correlation between the fluorescence intensity and the dynamic behavior. The corresponding distribution of MinE could not be assessed simultaneously.

Quantitative analysis. For a quantitative analysis, the fluorescence data were transformed into a real-valued time-dependent function f by subtracting the fluorescence intensities in the two cell halves, see Figure 6.2 and Materials and Methods. The residence time τ of MinD in one cell half is defined as the interval between two consecutive zeros of f . The residence time averaged over all measurements together with its standard deviation is shown in Fig. 6.3a as a function of cell length. Cell lengths were binned to $0.2\mu\text{m}$ and residence times were assigned to the length of the cell at the beginning of the respective dwell period¹³.

¹²See the glossary for 'kymograph'.

¹³Within 500s , which is exceptionally large for a residence time, the bacteria grew at most $0.2\mu\text{m}$ in length, such that our results do not depend significantly on the exact assignment rule.

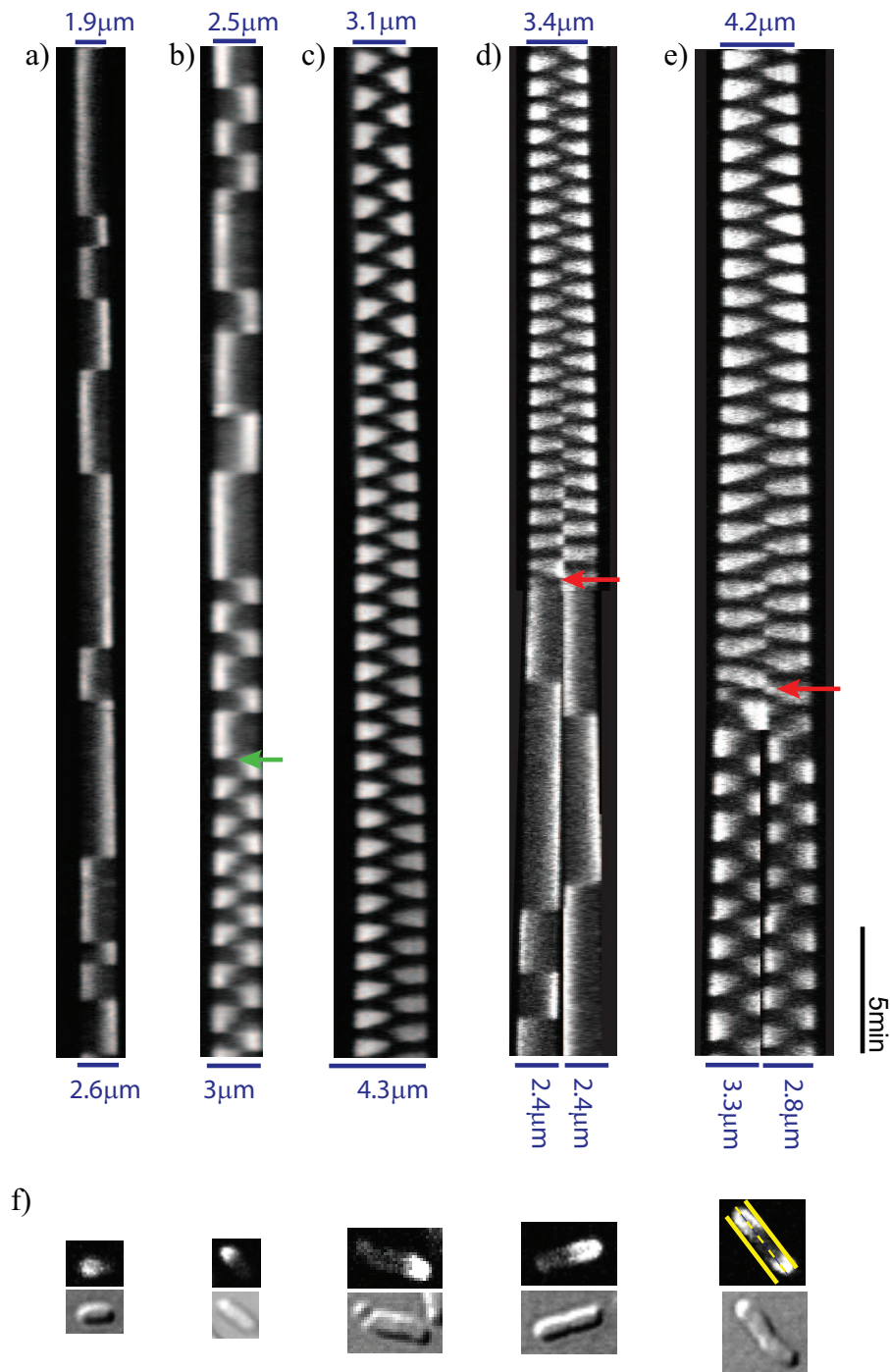


Figure 6.1: Kymographs of GFP-MinD fluorescence obtained from line scans along the long axis of five different bacteria. Fluorescence intensities have been averaged over the width of the respective cells. Time increases from top to bottom. The initial cell lengths are given at the top, final cell lengths at the bottom. a) Stochastic exchange of MinD between the two cell halves. b) Stochastic exchange turned into regular oscillations when this cell reached a length of $2.8\mu\text{m}$ (green arrow). c) Regular Min oscillations with a period of 73s. d, e) Min dynamics in dividing cells. Daughter cells show either stochastic switching (d) or regular oscillations (e). Divisions occurred, respectively, at lengths of $4\mu\text{m}$ and $5\mu\text{m}$ of the mother cells (red arrows indicate the time when fluorescence stopped to be exchanged between the two daughters). f1-f5) DIC and fluorescence images of the respective cells used in (a)-(e) at the beginning of the measurements.

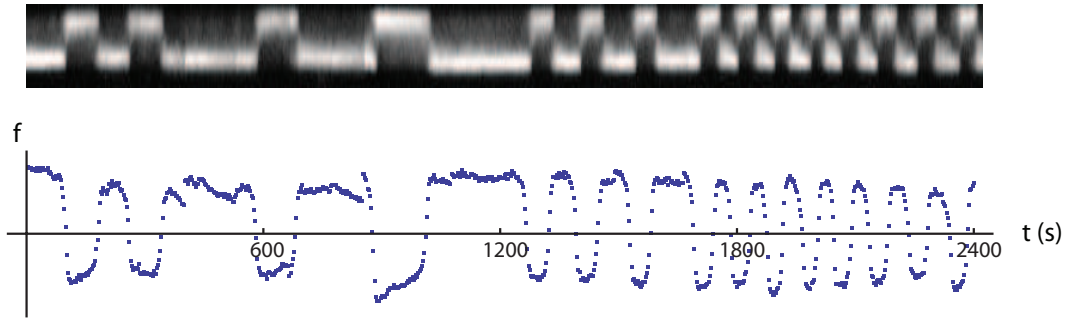


Figure 6.2: Kymograph of *E. coli* cell with fluorescently labeled MinD and corresponding fluorescence intensity curve f obtained by subtracting the fluorescence intensity of one cell half from the intensity of the other cell half.

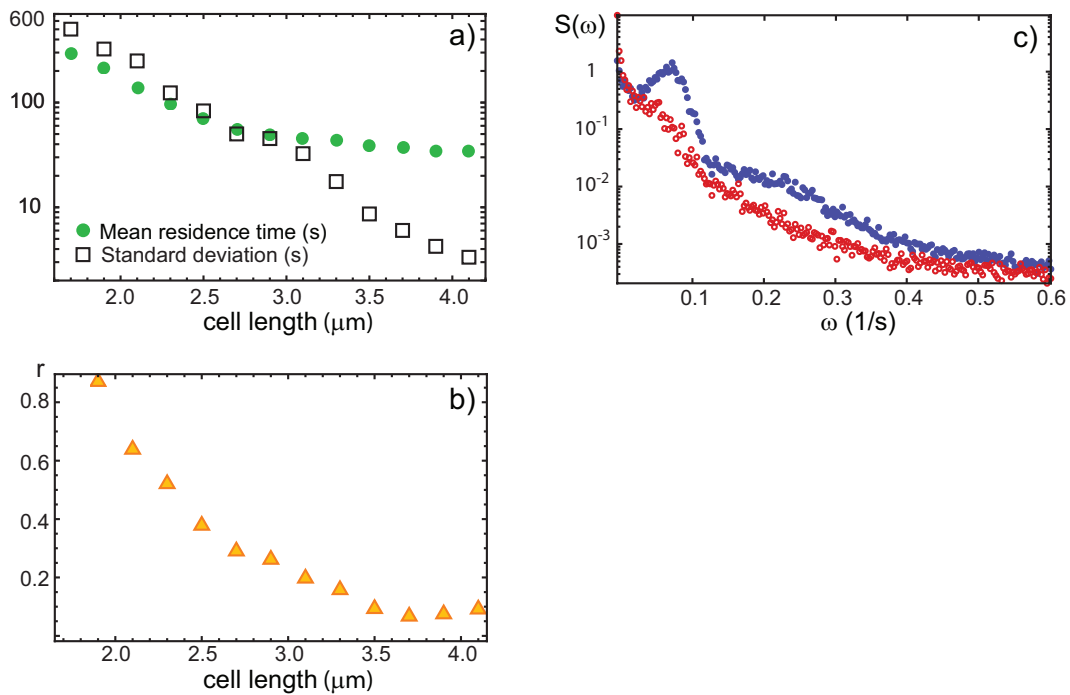


Figure 6.3: Residence time distributions averaged over all measurements. a) Mean (green dots) and standard deviation (black squares) of residence times τ as a function of cell length. Cell lengths have been binned to $0.2\mu\text{m}$. b) Ratio r of the standard deviation of residence times to their mean. Ratios have been calculated for single cells at a given length and were then averaged over the cell ensemble, see text for details. c) Power spectra $S(\omega)$ of the fluorescence function f for cells of length smaller than $2\mu\text{m}$ (red) and longer than $2.5\mu\text{m}$ (blue). The blue curve exhibits a peak at frequency 0.07s^{-1} corresponding to a period of $\simeq 90\text{s}$.

The mean residence time $\langle \tau \rangle$ decreases with cell length. For lengths smaller than $2.7\mu\text{m}$, $\langle \tau \rangle$ decreases exponentially with decay length $\approx 0.5\mu\text{m}$, while for longer cells it decays exponentially with decay length $\approx 2\mu\text{m}$. The corresponding standard deviation, too, is monotonically decreasing with increasing cell length. At $L = 2.7\mu\text{m}$ it falls below the mean residence time which indicates a transition from stochastic switching to regular oscillations. For cells larger than $3.5\mu\text{m}$ the standard deviation is below 10s such that the oscillation period varies remarkably little from cell to cell.

The existence of a transition from stochastic switching to regular oscillations is further supported by the power spectra corresponding to f for two different selections of cells, see Fig. 6.3c. In the first selection, we choose cells which are initially shorter than $2\mu\text{m}$. For the second selection, we choose cells initially longer than $2.5\mu\text{m}$. The first selection of cells contains mainly bacteria which exclusively switch stochastically during the observation time. For this cell ensemble, the averaged power spectrum monotonically decreases as a function of the frequency ω . The second selection of cells, which are on average longer, contains a considerable number of bacteria which start to oscillate regularly during the observation time. For this cell set, the averaged spectrum shows a clear peak at $\omega = 0.07/\text{s}$. This corresponds to a period of $T = 2\pi/\omega \approx 90\text{s}$.

The data in Fig. 6.3a and c reflect population averages. To rule out that the observed transition just reflects a reduction of cell-to-cell variability with increasing length and thus protein number, we considered the Min dynamics also in single cells. To this end, we analyzed the stochasticity of switching in individual cells by calculating for individual cells the ratio r_{sc} of the standard deviation of the residence time and the corresponding mean, $r_{sc} = (\langle \tau^2 \rangle_{sc} - \langle \tau \rangle_{sc}^2)^{1/2} / \langle \tau \rangle_{sc}$. Here, $\langle \dots \rangle_{sc}$ denotes the time average for a single cell over an interval during which the cell grew for $0.2\mu\text{m}$. In Figure 6.3b, we present the average ratio r as a function of the cell length, $r = \langle r_{sc} \rangle$, where $\langle \dots \rangle$ denotes the average over all measured cells in the respective length interval. The value of r initially drops monotonically and stays constant for cell lengths larger than $3.5\mu\text{m}$. These results confirm the findings obtained from ensemble averages. Note, that only cells were considered that, within a length interval of $0.2\mu\text{m}$, showed at least 5 switching events. In this way, very long residence times are not considered. Furthermore, the number of events entering r_{sc} is quite small which tends to systematically underestimate the standard deviation of the “real” distribution. For these reasons, the values of r are smaller than the ratio of the standard deviation and the mean displayed in Fig. 6.3a.

In addition to the change in the average residence time at the transition from stochastic switching to regular oscillations, there is also a qualitative change in the distribution of residence times for cells with a given length, see Fig. 6.4. For cells longer than $3.5\mu\text{m}$, the distribution can be fitted well by a log-normal distribution with a geometric mean of 37.5s and a geometric standard deviation of 1.2s. In contrast, for cells smaller than $2.5\mu\text{m}$, a log-normal distribution dramatically fails to describe the measured distribution of residence times. Instead, it decays algebraically as $N^{-\alpha}$ with $\alpha = 2.2$. This is in contrast to a usual random telegraph process in which a system switches stochastically between two states at given constant rates. In this case, the distribution of residence times in one state decays exponentially. For the distribution of MinD residence times, we have calculated

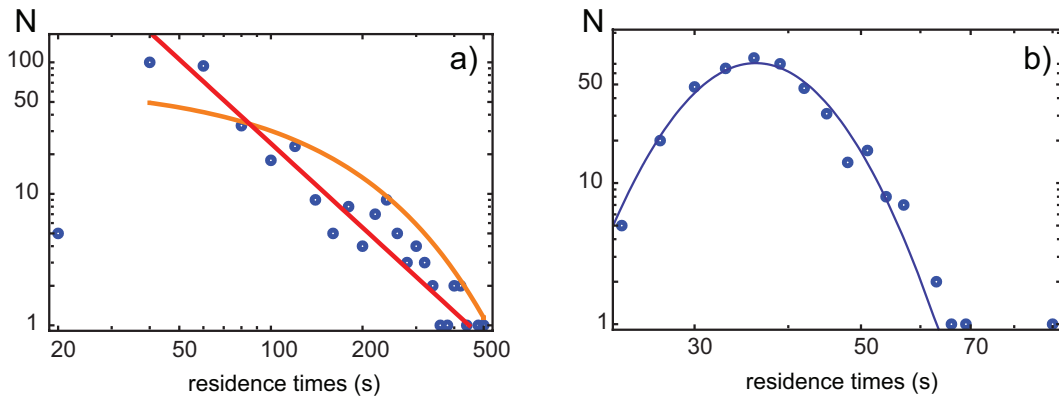


Figure 6.4: Histograms of residence times. a) Residence times for cell lengths between 2 and $2.2\mu\text{m}$ and b) for lengths between 3.5 and $4\mu\text{m}$. Times are binned into 20s intervals (a) and into 3s intervals (b). Solid lines in (a) result from fits of an algebraic distribution with exponent -2.2 (red line) and of an exponential distribution with a characteristic length of 0.008 (orange). The solid line in (b) represents the fit of a log-normal distribution with geometric mean 37.5s and geometric standard deviation 1.2s.

the logarithm of the likelihood ratio of the algebraic to the exponential decay. With a value of 110 it is strongly indicative of an algebraic decay [72].

What is at the origin of the transition between stochastic switching and oscillations of MinD?

The data presented above show that the form of the MinD pattern correlates with the cell length. One possible explanation for this phenomenon is suggested by theoretical analysis of the Min dynamics (see Section 2.3.1) and by *in vitro* experiments (see Section 4.1) which indicate that the Min-protein patterns are self-organized. In this case, it is conceivable that the system size can act as a control parameter in the self-organized system. Consequently, the cell length might directly determine if the MinD distribution is switching stochastically or oscillates. In this scenario, for cells below a critical length, the Min-system settles into one of two mirror-symmetric stationary states. Transitions between these states occur stochastically due to intrinsic or external noise. In cells longer than the critical length, the Min-system would then self-organize into the oscillatory pattern.

Computational models do not support the idea of the cell length as control parameter. We have tested the idea of the cell length acting as control parameter by investigating several models that have been presented for the dynamics of MinD and MinE. Neglecting fluctuations, the model presented by Meinhardt and de Boer [32] and the cooperative attachment model suggested by us (Section 4.2, [12]) show a transition from a stable stationary state that coexists with its mirror-symmetric state to an oscillatory state upon increasing the system length¹⁴. However, the first of these models relies on protein synthesis and degradation, which has been shown to be irrelevant for the oscillation

¹⁴H. Meinhardt, private communication with K. Kruse

mechanism. The stationary states, we obtained within the second model, show only a slight difference between the MinD levels in the two cell halves (less than 5%) [73]. Correspondingly, in a stochastic version of this model, we could not detect exchanges comparable to the experiments. The aggregation current model considered in Section 2.3.2 does present stationary bistable states, however, we did not find a transition to oscillatory states by changing only the system length. For all other models that we tested, we did not find stationary states comparable to those observed experimentally. We conclude that the models do not support the idea of the cell length to be a control parameter for the transition between stochastic exchanges and oscillations.

Cell age as control parameter. We have found that the form of the Min patterns depends on the cell length. However, we could interpret our result also in the alternative way that the Min pattern depends on the cell age, since the length of the cell correlates strongly with age. While aging, the cell adopts different stages of the life cycle and thus the parameters of the Min system might change over time.

This idea is supported by the following observations: As noted above, some daughter cells of about the same length showed different MinD patterns. In addition, occasionally cells shorter than $2\mu\text{m}$ showed oscillations, while in some cells longer than $3\mu\text{m}$, MinD was switching stochastically between the two cell halves. Therefore, factors other than the cell length have to influence the MinD pattern. While, in principle, factors external to the Min system might play a role, for example, the lipid composition of the cytoplasmic membrane, we will in the following discuss only mechanisms intrinsic to the Min system.

- It is conceivable that MinD and/or MinE production in the cell is not constant over time but peaks at a certain phase of the life cycle. This would result in varying Min protein concentrations in the course of the cell's life cycle. However, we see stochastic oscillations in daughter cells directly after division of a regularly oscillating mother cell (see Fig. 6.1d). Assuming that segregation of Min proteins to the daughter cells is approximately equal, the daughter cells will have the same Min protein concentration as the mother. In this scenario, the protein concentration could not trigger the altered Min switching of the daughter cells. On the other hand, it is possible that Min proteins are consumed in the process of division or that the Min segregation to the different daughter cells is considerably uneven. In these cases, the protein concentration in the daughter cells could still differ from those in the mother and might play a role for the altered Min patterning behavior.
- Prior to division the bacterial cell duplicates its DNA and segregates the two chromosomes to either half of the cell. The presence of the DNA close to the cell poles might as well influence the parameters of the Min dynamics. Proteins which are associated with the DNA could influence membrane binding, ATP hydrolysis or ATP exchange of MinD. This might facilitate the resolution of the Min concentration maximum at the pole leading to a limited residence time. In this way, the cell could assure that Min oscillations work in the "regular" way directly before constriction of the cell.
- During Min pattern formation in the *E. coli* cell, MinE is not distributed evenly on top of the MinD concentration maximum at the pole. At the rim

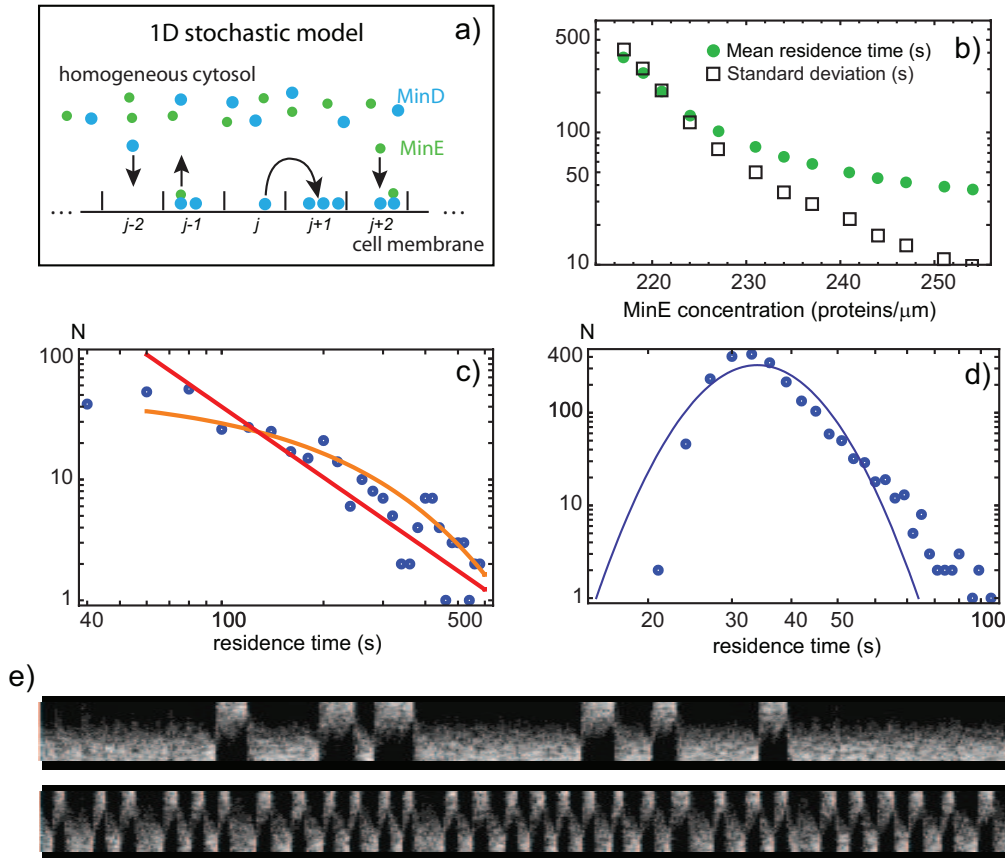


Figure 6.5: Results of simulations with the stochastic model introduced in Appendix D. a) Schematic illustration of stochastic model. Min protein distribution in the cytoplasm is considered as homogeneous due to large cytoplasmic diffusion. The cell membrane is modeled as one-dimensional array of spatial bins in which Min proteins can dwell. b) Dependence of mean residence times (green dots) and standard deviation (grey squares) on the MinE concentration used in the simulations. The MinD concentrations was fixed as $720\mu\text{m}^{-1}$. c),d) Histograms of residence times in stochastically and periodically switching cells, respectively. Time bins are 20s for c) and 3s for d). In c), Solid lines result from fits of an algebraic distribution with exponent -1.9 (red line) and of an exponential distribution with a characteristic length of 0.006 (orange), see also Fig. 6.4. As part of the tail, we considered data points with $\Delta T \geq \Delta T_{\min}$. ΔT_{\min} was chosen as 60s. The exponential fit is slightly favored for the tail distribution according to the likelihood ratio. This contrasts the situation in the experiment where for shorter cells the algebraic decay clearly suits better. In d), the blue curve shows the corresponding log-normal distribution with geometric mean 35.7s and geometric standard deviation 1.3s. e) Kymographs of two solutions to the stochastic model introduced in Appendix D for a time interval of 40min and a MinE concentration of 221 and 254 MinE proteins per micrometer, respectively. The oscillation period in the second kymograph is 75s.

The chosen parameters were $\omega_D = 0.08\text{s}^{-1}$, $\omega_E = 0.6\text{s}^{-1}$, $\omega_{de} = 0.08\text{s}^{-1}$, $D_d = 0.12\mu\text{m}^2/\text{s}$, $r_d = 1.2\mu\text{m}$, $r_{de} = 0.1\mu\text{m}$, $g_d = 35k_B T$, $g_{de} = -20k_B T$, $n_{\max} = 43$. The cell length is $2.5\mu\text{m}$ and the total simulation time was 1300min. The cell was subdivided in $m = 75$ spatial bins. The MinD concentrations was $720\mu\text{m}^{-1}$.

of the MinD aggregation, a MinE concentration maximum forms known as the MinE ring. The role of the MinE ring for Min oscillations is not entirely clear. It has been shown experimentally that the MinE ring is not necessary for Min oscillations to occur in cells [29,74] but it seems to support robustness of Min oscillations. In the following, we will anticipate that the concentration of Min proteins stays constant while the cell grows. It is conceivable that the MinE ring forms a passive reservoir of MinE proteins, which effectively reduces the number of active MinE proteins that act on MinD detachment from the membrane. Assuming that the MinE ring is constituted by a fixed number of MinE proteins independently of the cell length, the fraction of buffered MinE would be higher in shorter cells than in longer cells. Thus the ratio of active MinE to MinD would be reduced in shorter cells which might give rise to the stochastic switching of MinD maxima.

Conversely, the MinE ring might be especially active in MinD detachment from the membrane in comparison to the sparse MinE cover on top of the MinD tube at the membrane. In this scenario, it is possible that the absolute number of MinE is not high enough in short cells to form a complete MinE ring which reaches its full activity in MinD removal from the poles. Thus, the effective detachment rate of MinD from the membrane would be smaller for shorter cells which could induce stochastic switching of Min.

Taking up the idea of a reduced fraction of active MinE in short cells as mentioned in the third point of the above listing, we have performed simulations using a stochastic version of the aggregation current model introduced in Section 2.3.2. This particle based model was developed by G. Meacci as part of his PhD thesis [75]. A short description of this model is given in Appendix D. Since this model in its simplest form does not capture the formation of the MinE ring, we tested the properties of solutions varying MinE concentrations in the system (at fixed cell length). We find stochastic switching of Min proteins for low MinE numbers similar to those observed in small *E. coli* cells. When increasing the MinE concentration, a transition to regular oscillations takes place, see Figure 6.5. Thus, the model predicts that a decrease of the MinE concentration can trigger a transition from regular oscillations to stochastic switching. According to the model also a joint decrease of MinD and MinE concentrations, or the change of the maximal concentration of Min proteins on the membrane can trigger this transition (data not shown).

According to our simulations, stochastic solutions show a residence time distribution whose tail better fits to an exponential decay as is expected for a random telegraph process. This contrasts the situation in the experiment where we find an algebraic decay for the residence time distribution of short cells, see Figure 6.4a. If, however, we take into account fluctuations of the protein numbers in different cells around a given mean, we then find an algebraic decay, see Fig. 6.6. This mechanism is similar to suggestions by Tu and Grinstein for explaining power-law switching of bacterial flagellar motors [76].

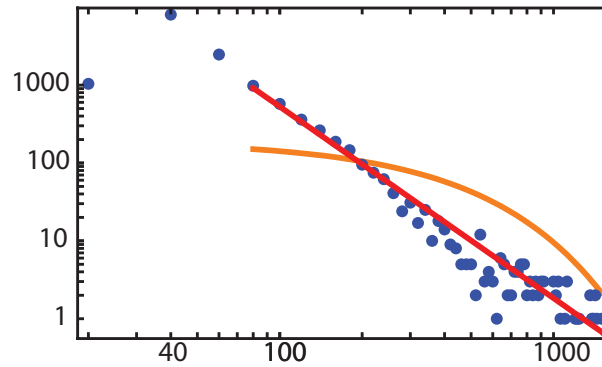


Figure 6.6: Distribution of residence times obtained from simulations of the stochastic version of the AC model (see Appendix D). The data have been obtained from different runs which varied in the total MinD and MinE concentrations. The values of the concentrations were drawn from a Gaussian distribution with mean value $360\mu\text{m}^{-1}$ for MinD and $134\mu\text{m}^{-1}$ for MinE and a standard deviation of 10%. The remaining parameters are as in Figure 6.5. The algebraic fit (red curve) has an exponent of -2.46 whereas the exponential fit (orange curve) decays with a rate of 0.003s^{-1} .

6.2 Min oscillations in filamentous “overaged” cells

When grown at higher temperatures, a fraction of cells of our strain grows filamentous, i.e. it does not divide around the typical length of $4\mu\text{m}$ but extends further in length before a septum is formed. As already mentioned, the Min pattern changes in filamentous cells. Typically, wave nodes are gained in the concentration profile if cells grow filamentous resulting in a zebra-striped fluorescence pattern. We have observed the switching process from normal Min oscillations to a pattern with three stripes, i.e. two wave nodes, in growing cells. Examples are shown in Figure 6.7a,b. We have noted that frequently a transient state with traveling waves bridges between states of one and two wave nodes. This is nicely illustrated in the kymograph depicted in Figure 6.7a.

If cells with a two-wave-node Min pattern grow even longer, either additional wave nodes appear [20], or, as we have found, traveling wave patterns are chosen. Examples are shown in Figure 6.7c,d. This traveling wave patterns can also contain defects as in the upper part of Figure 6.7d. Surprisingly, concentration peaks travel only in one direction (from left to right or reversed) within the cell, i.e. the waves are not reflected at the polar cell boundary but presumably Min proteins detach from the membrane, and a new concentration peak forms at the opposing cell pole. Also, only one fluorescence maximum is present.

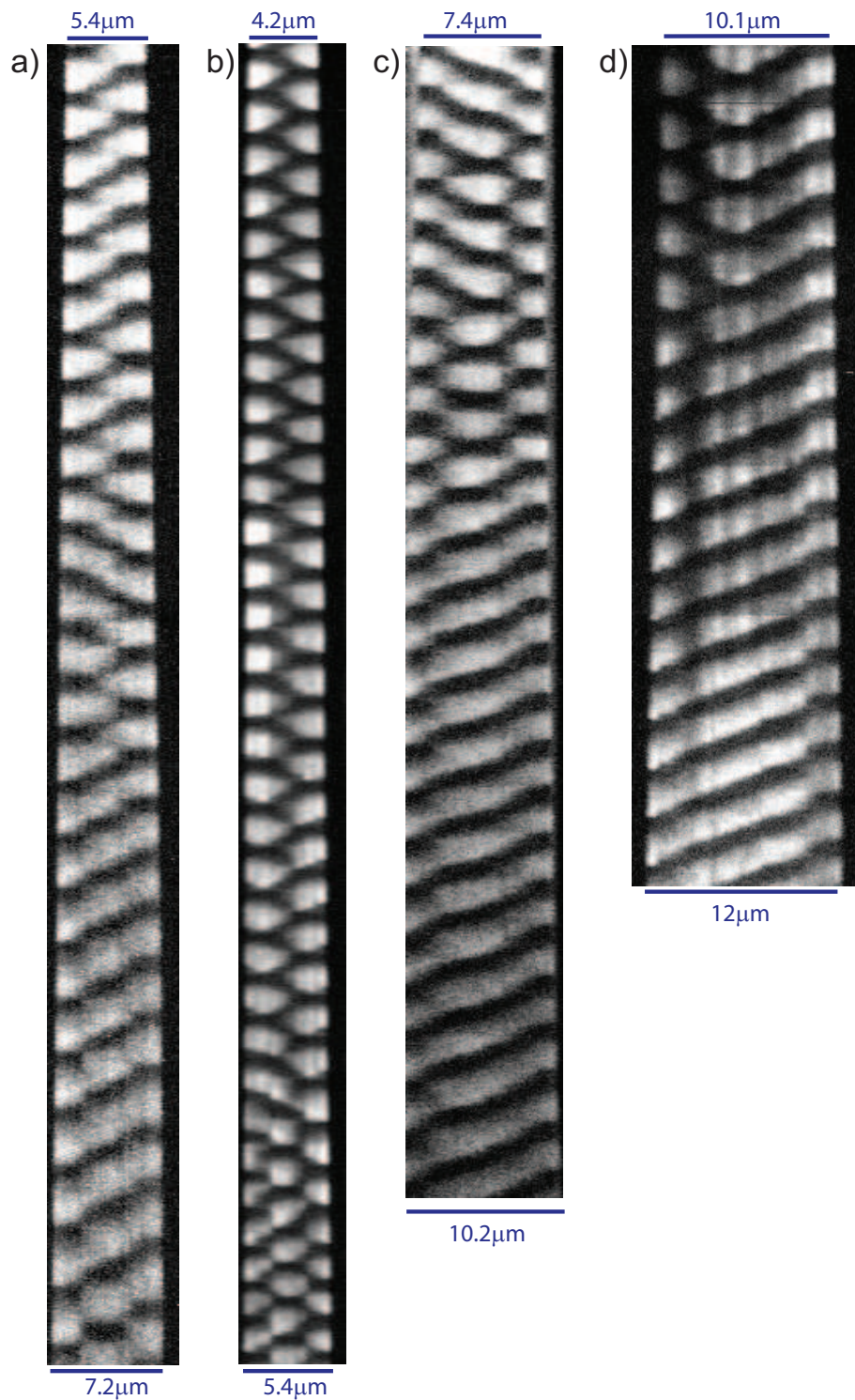


Figure 6.7: Kymographs of filamentous *E. coli* cells expressing fluorescently labeled MinD. Time proceeds from top to bottom. a),b) Cells switching from normal Min oscillations to a three-stripe pattern were fluorescence maxima at the poles alternate with a fluorescence maximum at the cell middle. c),d) Cells switching from a three-stripe pattern with two wave nodes to a traveling wave pattern.

Chapter 7

Conclusions and Outlook

For a long time, bacteria were considered as unstructured bags of enzymes. Only since a few years, it is known that they build up cytoskeletal structures just as eukaryotic cells in order to maintain their cell shape, to accomplish cell division and metabolic processes [4]. Min proteins are a class of cytoskeletal proteins which is found in many bacteria. They are involved in the regulation of the division process of the cell and help to position the division machinery to the cell middle. In *Escherichia coli*, there are three Min proteins, MinC, MinD and MinE, which form spatiotemporal patterns in the cell [17]. They bind to the inner cytoplasmic membrane and form concentration maxima at one cell pole which persist for a characteristic dwell time. Then, this concentration maximum resolves and switches to the opposite pole of the cell. This cycle is repeated and gives rise to the so-called Min oscillations [17]. The Min protein MinC suppresses the formation of the contractile ring and thus prevents cell division at both cell poles but not in the middle of the cell [17].

In this thesis, we asked for the mechanism that guides the Min proteins to form dynamic, spatially inhomogeneous patterns. We did both theoretical and experimental studies on the Min system. The theoretical work of this thesis includes the analysis of two computational models which are based on different underlying assumptions which aspect of Min protein interactions causes the instability in the Min system. Experimentally, this has not yet been clarified and both models are based on plausible scenarios. The first computational model, which we termed aggregation current (AC) model, assumes that MinD binds from the cytosol to the inner cytoplasmic membrane in an unbiased way and then forms aggregates by mutual interactions of bound proteins which give rise to an aggregating current term in the equations. In the second computational model, we assumed instead cooperative attachment (CA) of MinD and MinE to the membrane and did not take interactions of bound proteins into account. In both scenarios, an instability arises leading to spatiotemporal patterns. We examined the solutions predicted by the different models for differently shaped cells and in flat open geometries corresponding to a flat membrane in an *in vitro* experimental situation. The experimental part of this thesis includes the observation of Min oscillations in growing cells and in cells with an enlarged radius. In this context, we performed fluorescence microscopy on an *E. coli* strain expressing fluorescently labeled MinD. Furthermore, we were able to extract characteristic time scales of the *in vivo* Min dynamics by analyzing data from fluorescence correlation spectroscopy.

7.1 Summary of results

- Our aggregation current (AC) model as well as our cooperative attachment model (CA) can reproduce the Min patterns observed in wild type cells. Accordant solutions can either be obtained in a bounded one-dimensional

space interval with zero-flux boundary conditions, or in a model cell given by a cylinder with hemispherical caps.

- To characterize the AC model further, we studied solutions in an open geometry. For one space dimension, the AC model of Min oscillations can create traveling or standing wave patterns of concentrations dependent on chosen parameters. We calculated the mode coupling coefficient of the respective amplitude equations of the dynamic system close to the Hopf bifurcation. From this, we could read off whether the system stabilizes traveling or standing wave solutions. For two space dimensions, however, we found that planar wave solutions are not stable. Therefore, this model cannot account for the Min patterns which have been found *in vitro*.
- The CA model can generate planar wave trains of concentrations in one and two space dimensions. We also observed the existence of stable spiral distributions. The CA model thus predicts two-dimensional patterns which come close to the *in vitro* patterns of Min proteins observed in experiments. This computational model can account for patterns from *in vivo* and *in vitro* experiments.
- Both computational models suggested in this thesis predict that for cells with an enlarged radius circumferential modes can appear in the oscillations. This is expected if the radius of the cell becomes larger than L_{crit}/π , where L_{crit} is the minimal cell length for which oscillations occur. We estimate $L_{\text{crit}}/\pi \approx 0.65\mu\text{m}$. We performed an *in vivo* study with *E. coli* cells of enlarged radius and indeed observed circumferential modulations of Min concentrations especially during the switching between the cell poles. These thickened cells were obtained by treatment with the drug A22 which perturbs the cytoskeleton of *E. coli*.
- Analysis of fluorescence correlation spectroscopy obtained from measurements on Min proteins *in vivo* revealed characteristic time scales of Min dynamics. Therefrom, we could estimate diffusion constants of $\approx 17\mu\text{m}^2/\text{s}$ and $\approx 11\mu\text{m}^2/\text{s}$ for MinD and MinE, respectively.
- Min oscillations depend on the cell geometry and change while the cell grows. We recorded the oscillation of fluorescently labeled MinD for extended periods of up to 40min. We found that for short cells of around $2\mu\text{m}$ length MinD maxima form but tend to switch stochastically between the two cell poles with much longer residence times as have been observed for regularly oscillating cells. When the cells lengthen the switching becomes more periodic. We found that on average standard deviations of residence times drop below the mean value at a length of around $2.7\mu\text{m}$ indicating a transition from stochastic switching to oscillations. Before cell division, Min oscillations always had become regular.

For our AC as well as for our CA model, we could reproduce the Min oscillations observed in wild type cells. Yet, we cannot conclusively tell which mechanism creates the instability in the Min system. Both computational models have their strengths and their weaknesses. Oscillations in filamentous *E. coli* mutants are

more accurately described by the AC model [13]. Also, it shows the existence of stationary spatially inhomogeneous states which resembles those observed for very short *E. coli* cells where the majority of Min proteins is located in one cell half. By contrast, *in vitro* patterning of the Min system is more aptly captured by our CA description which relies on cooperative binding.

7.2 Outlook on future work

Microscopic processes

In this thesis, we posed the question which mechanism generates the instability in the Min system. To address this issue, we made a coarse-grained approach in terms of mean field equations. The two models considered in this thesis rely on different underlying assumptions regarding Min protein interactions and kinetics. Our analysis has shown, that we cannot rule out one or the other assumption by looking merely at the pattern formation predicted by the obtained mathematical models. It would thus be beneficial to gain more experimental insight into the Min system to validate or falsify the different approaches.

On the microscopic level, many question regarding the Min system are still open. The following issues are pivotal to understand the functioning of the Min system:

- What kind of MinD aggregates form on the membrane? Does it form unstructured clusters of proteins, or do filamentous polymers form? If filamentous polymers exist, is there a preferred direction of orientation? Helical polymer structures of MinD have been reported in the literature [30]. However, we performed TIRF microscopy on *E. coli* expressing fluorescently labeled MinD (data not shown) and did not observe helix structures. We conclude therefore that MinD helices are not necessarily contained in the Min system and might only occur for certain strains and/or special salt/protein concentrations.
- How do MinD proteins gather to form aggregates on the membrane? Do they aggregate while bound to the membrane (as assumed in the AC model), or do they bind self-enhanced (as in cooperative attachment models)?
- Does MinE really bind to one fixed MinD protein on the membrane with which it detaches jointly? Alternatively, MinE might have some kind of processivity, i.e. it could stay attached to the membrane when the MinD protein detaches to which it was formerly associated. A second possibility is that MinE forms polymers on the membrane which is merely nucleated at bound MinD.
- How is the MinE ring formed and what is its role for the pattern formation? Is the MinE ring especially active in detaching MinD from the membrane or is it a passive MinE reservoir, which reduces the concentration of MinE interacting with MinD?
- Do the same processes take place during the pattern formation in the *E. coli* cell and on the supported lipid bilayer *in vitro*? Do the same kind of microscopic structures form?

In the long run, a particle-based description of Min proteins is desirable to incorporate the effect of noise on Min patterns and to include polymerization processes.

Interaction with the division machinery

The way in which the Min system interacts with the division machinery of the *E. coli* cell is not entirely clarified. It is known that the protein MinC, which basically follows the dynamics of MinD, depolymerizes FtsZ polymers. However, it is not clear if the FtsZ concentration on the membrane along the bacterial long axis is just depleted proportional to the time-averaged concentration of MinC on the membrane or if the relationship to the MinC concentration is more involved. It might be the case that a threshold concentration or a minimal dwell time of MinC has to be reached to induce an effect on FtsZ polymers.

Another interesting question is, if changes in the Min pattern due to increasing cell length induce the onset of cell division. The Min system could provide a measure for the length of the cell by changing its pattern when the cell grows. This could trigger the assembly of the division machinery at the appropriate time.

Appendix A

The case of large diffusion constants in the aggregation current (AC) model

We consider the case of large cytoplasmic diffusion constants of MinD and MinE in the context of the aggregation current model introduced in 2.3.2. We show in the following, that in this case the dynamic equations for the cytoplasmic concentration fields (2.2)-(2.3) decouple from the equations for the membrane-bound proteins (2.4)-(2.5).

In the case of large cytoplasmic diffusion constants D_D and D_E , the times needed to diffuse along the whole length L of the bacterium, L^2/D_D and L^2/D_E , respectively, are short compared to all other relevant time-scales in the Min dynamics. Thus, the distribution of Min proteins in the cytoplasm can be assumed to be spatially homogeneous, i.e. we can choose cytoplasmic concentration fields $c_D(x, t) = c_D(t)$ and $c_E(x, t) = c_E(t)$. Integrating the equations (2.2)-(2.3) over the entire space and dividing by the cell volume, we obtain the following decoupled set of ordinary differential equations for the cytoplasmic concentration fields

$$\frac{d}{dt}c_D = -\omega_D(c_{\max} - \mathcal{D} + c_D)c_D + \omega_{de}(\mathcal{E} - c_E) \quad (\text{A.1})$$

$$\frac{d}{dt}c_E = -\omega_E(\mathcal{D} - \mathcal{E} - c_D + c_E)c_E + \omega_{de}(\mathcal{E} - c_E). \quad (\text{A.2})$$

Here, the variables \mathcal{D} and \mathcal{E} denote the total spatially averaged concentration of MinD and MinE, respectively.

For physical conditions $0 \leq c_D \leq \mathcal{D}$ and $0 \leq c_E \leq \mathcal{E}$, the above equations have one fixed point which is always stable [13]. Asymptotically, the cytoplasmic distributions will approach the stationary state $\{C_D, C_E\}$. In this limit, the dynamics of the membrane-bound Min proteins is described by two partial differential equations

$$\partial_t c_d = \omega_D C_D (c_{\max} - c_d - c_{de}) - \omega_E C_E c_d - \partial_x j_d \quad (\text{A.3})$$

$$\partial_t c_{de} = -\omega_{de} c_{de} + \omega_E C_E c_d. \quad (\text{A.4})$$

Appendix B

Calculation of the linear spreading velocity

In this appendix, we calculate the linear spreading velocity of a localized perturbation into an unstable stationary homogenous state of the dynamic equations (2.7) and (2.8) in the situation discussed in Sec. 3.2. The distributions c_D and c_E are assumed to be homogenous, their values are free parameters. In order to simplify our calculations, we set $\bar{k}_1 = \bar{k}_2 = 0$ and restrict ourselves to parameter values such that $\bar{\omega}_D \bar{\omega}_E < \omega_{de}^2$, where $\bar{\omega}_D = \omega_D C_D$ and $\bar{\omega}_E = \omega_E C_E$. We assume that for each wave-vector k at most one of the eigenmodes grows in time and the corresponding growth exponent is real. In an open geometry, the asymptotic solutions are stationary if the rates satisfy the condition above.

The linear spreading velocity is obtained from the solution of the dynamic equations that are obtained by linearizing (2.7) and (2.8) with respect to a stationary homogenous state. In general, the solution $\mathbf{c} = (c_d, c_{de})$ to these equations can be written as

$$\mathbf{c}(x, t) = \frac{1}{2\pi} \int_{-\infty}^{\infty} dk e^{\Lambda(k)t + ikx} \bar{\mathbf{c}}(k), \quad (\text{B.1})$$

where $\bar{\mathbf{c}}(k) = \int_{-\infty}^{\infty} dx \mathbf{c}(x) \exp(-ikx)$ denotes the Fourier transform of $\mathbf{c}(x, t = 0)$. The matrix $\Lambda(k)$ is the time-evolution operator of the linearized dynamic equations in Fourier representation

$$\Lambda(k) = \begin{pmatrix} -\bar{\omega}_D - \bar{\omega}_E + (K - D_d)k^2 + Kk^4 & -\bar{\omega}_D \\ \bar{\omega}_E & -\omega_{de} \end{pmatrix}, \quad (\text{B.2})$$

where K is the dimensionless control parameter $K = c_{\max}^2 k_1^2 / (\omega_{de} k_2)$. Let $\mathbf{e}_1(k)$ denote the normalized eigenmode of $\Lambda(k)$ associated to the eigenvalue λ_1 , that has the larger real part of the two eigenvalues. Then, we can write

$$\mathbf{c}(x, t) = \frac{1}{2\pi} \int_{-\infty}^{\infty} dk e^{\lambda_1(k)t + ikx} (\bar{\mathbf{c}}(k) \cdot \mathbf{e}_1(k)) \mathbf{e}_1(k). \quad (\text{B.3})$$

Now consider a uniformly translated reference frame with coordinates $\xi = x - v^*t$. Here, v^* is the average spreading velocity of the perturbation in the limit of large times. Adapting coordinates to this frame, Eq. (B.3) becomes

$$\mathbf{c}(x, t) = \frac{1}{2\pi} \int_{-\infty}^{\infty} dk e^{i\xi k} e^{(\lambda_1(k) + iv^*k)t} (\bar{\mathbf{c}}(k) \cdot \mathbf{e}_1(k)) \mathbf{e}_1(k). \quad (\text{B.4})$$

As we have chosen the frame such that we ride on the front, we must have for consistency $v^* = \frac{\lambda_{1,r}}{k_i}$.¹⁵ Otherwise the absolute value of $e^{(\lambda_1(k) + iv^*k)t}$ would decay or grow exponentially. v^* is the velocity with which the front spreads in

¹⁵Subscripts r and i denote the real and imaginary parts, respectively, i.e. $k = k_r + ik_i$ and $\lambda_1 = \lambda_{1,r} + i\lambda_{1,i}$.

the linearized case. As for the chosen parameter regime the emerging pattern in the wake of the front is stationary with wavelength ℓ , the concentration $\mathbf{c}(\xi, t)$ in the moving frame oscillates with frequency $\omega = v^*/\ell$. From (B.4), we can read off ω as $(\lambda_{1,i}(k) + v^*k_r)$. This determines ℓ provided we know v^* .

For large times, the integral (B.4) can be approximated by focusing on the factor $E(t) := e^{(\lambda_1(k) + iv^*k)t}$. Assuming a holomorphic integrand, the integration contour is first moved into the complex plane such that integration is along a contour of constant phase of $E(t)$. Then a saddle point approximation is performed [77]. At a saddle point k^* on a contour of constant phase, the gradient of the real and the imaginary part of $E(t)$ have to vanish. Therefore, the exponent $(\lambda_1(k) + iv^*k)t$ has to obey $\partial(\lambda_{1,r} - v^*k_i)/\partial k_r \Big|_{k^*} = \partial(\lambda_{1,r} - v^*k_i)/\partial k_i \Big|_{k^*} = 0$. Consequently,

$$\partial\lambda_{1,r}/\partial k_i \Big|_{k^*} = \lambda_{1,r}/k_i \Big|_{k^*} \quad (\text{B.5})$$

$$\partial\lambda_{1,r}/\partial k_r \Big|_{k^*} = 0, \quad (\text{B.6})$$

where

$$\lambda_1(k) = p(k)/2 + \sqrt{p(k)^2/4 - \bar{\omega}_D \bar{\omega}_E}$$

with

$$p(k) = \omega_{de} - \bar{\omega}_D - \bar{\omega}_E + (K - D_d)k^2 - Kk^4.$$

We have solved Eqs. (B.5) and (B.6) numerically. To this end we neglected $\bar{\omega}_D \bar{\omega}_E$ in the expression for $\lambda_1(k)$. The good agreement between the values we obtain for the asymptotic linear spreading velocity and the results from our numerical solutions of the dynamic equations (2.7) and (2.8) justifies this approximation, see Fig. 3.8d.

Appendix C

Derivation of amplitude equations

C.1 The case of $\bar{k}_1 = \bar{k}_2 = 0$

We are deriving the coefficient g_1 of the amplitude equations for the dynamical system given by Equations (3.6) for the special case of $\bar{k}_1 = \bar{k}_2 = 0$, i.e. $\delta = 0, \delta\zeta = 0$. To this end, we perform a perturbation calculation substituting the Expansions (3.8) into the Equation (3.7) which describes the time evolution of deflections from the homogeneous state.

C.1.1 Second order equation

The terms of second order in ϵ give the following equation

$$\begin{aligned}
 (\partial_{t_0} - \mathcal{L})\mathbf{X}_2 &= -\partial_{t_1}\mathbf{X}_1 & (C.1) \\
 &+ D_d \begin{pmatrix} 1 \\ 0 \end{pmatrix} 2\partial_{x_0}\partial_{x_1}\mathbf{X}_1 - K'_c \begin{pmatrix} 1 \\ 0 \end{pmatrix} (2\partial_{x_0}\partial_{x_1}X_{d,1} + 4\partial_{x_0}^3\partial_{x_1}X_{d,1}) \\
 &- K'_1 \begin{pmatrix} 1 \\ 0 \end{pmatrix} (\partial_{x_0}^2 X_{d,1} + \partial_{x_0}^4 X_{d,1}) \\
 &- K'_c \begin{pmatrix} 1 \\ 0 \end{pmatrix} \partial_{x_0}(\alpha X_{d,1} + \beta X_{de,1})(\partial_{x_0}X_{d,1} + \partial_{x_0}^3 X_{d,1}).
 \end{aligned}$$

Here, \mathcal{L} is the time evolution operator of the linearized equations. The term in the second line on the r.h.s. vanishes due to the form of k_c . The remaining terms linear in \mathbf{X}_1 give a solvability condition on A_L and A_R . This condition demands that the occurring terms on the r.h.s. of the above equation have to be in the image space of the operator $(\partial_{t_0} - \mathcal{L})$. This requirement puts constraints on the terms with Fourier components $\exp(i(\pm\omega_c t_0 \pm k_c x_0))$, since for these modes the null space of the operator is not zero. The solvability condition results in equations for A_L and A_R , separately. These equations include the time derivatives $\partial_{t_1} A_{L/R}$ and show that $A_{L/R}$ exponentially grow or decay with t_1 if K'_1 is nonzero. Since exponential growth or decay is not expected for a subcritical bifurcation, K'_1 has to be zero. The equations of the solvability condition then give $\partial_{t_1} A_{L/R} = 0$ and thus $\partial_{t_1}\mathbf{X}_1$ vanishes. The term on the l.h.s. as well as the term nonlinear in \mathbf{X}_1 in Equation (C.1) give information about \mathbf{X}_2 . Expansion of the term nonlinear in \mathbf{X}_1 in Fourier components give the following expression for \mathbf{X}_2

$$\begin{aligned}
 \mathbf{X}_2 &= (\partial_{t_0} - \mathcal{L})^{-1} \left\{ -K'_c \begin{pmatrix} 1 \\ 0 \end{pmatrix} \partial_{x_0}(\alpha X_{d,1} + \beta X_{de,1})(\partial_{x_0}X_{d,1} + \partial_{x_0}^3 X_{d,1}) \right\} \\
 &= C_{2,2}\mathbf{U}_{2,2} \exp(2i(\omega_c t + k_c x)) + C_{2,-2}\mathbf{U}_{2,-2} \exp(2i(\omega_c t - k_c x)) \\
 &\quad + C_{-2,2}\mathbf{U}_{-2,2} \exp(-2i(\omega_c t + k_c x)) + C_{-2,-2}\mathbf{U}_{-2,-2} \exp(-2i(\omega_c t - k_c x)) \\
 &\quad + C_{0,2}\mathbf{U}_{0,2} \exp(-2ik_c x) + C_{0,-2}\mathbf{U}_{0,-2} \exp(-2ik_c x)
 \end{aligned}$$

where

$$\begin{aligned}
C_{2,2} &= -2A_L^2 k_c^2 (k_c^2 - 1) K'_c v_d (\alpha v_d + \beta v_{de}) \\
C_{2,-2} &= -2A_R^2 k_c^2 (k_c^2 - 1) K'_c v_d (\alpha v_d + \beta v_{de}) \\
C_{-2,2} &= C_{2,-2}^*, \quad C_{-2,-2} = C_{2,2}^* \\
C_{0,2} &= -2A_R k_c^2 (k_c^2 - 1) K'_c A_L^* (\beta v_{de} v_d^* + v_d (2\alpha v_d^* + \beta v_{de}^*)) \\
C_{0,-2} &= -2A_L k_c^2 (k_c^2 - 1) K'_c A_R^* (\beta v_{de} v_d^* + v_d (2\alpha v_d^* + \beta v_{de}^*))
\end{aligned}$$

and

$$\mathbf{U}_{n,m} = e^{-i(n\omega_c t_0 + mk_c x_0)} (\partial_{t_0} - \mathcal{L})^{-1} \begin{pmatrix} 1 \\ 0 \end{pmatrix} e^{i(n\omega_c t_0 + mk_c x_0)}. \quad (\text{C.2})$$

The Coefficients $C_{.,.}$ have been calculated by defining the Mathematica function

$$\text{Coeff}[expr_ , n_ , m_] := ((\text{Coefficient}[expr//Expand, \text{Exp}[I * (n * \omega * t + m * k_c * x)]]/.Exp[y_] - > 0)//Simplify$$

and setting e.g.

$$C_{2,2} = \text{Coeff}[-K'_c \partial_{x_0} (\alpha X_{d,1} + \beta X_{de,1}) (\partial_{x_0} X_{d,1} + \partial_{x_0}^3 X_{d,1}), 2, 2].$$

The inverse of $(\partial_{t_0} - \mathcal{L})$ is chosen, such that no elements from the null space of the operator are added, i.e. the mapping preserves Fourier modes. This can be done, since we can assume that \mathbf{X}_2 is orthogonal to the null space of $(\partial_{t_0} - \mathcal{L})$. If the projection of \mathbf{X}_2 to the null space of $(\partial_{t_0} - \mathcal{L})$ were not zero but \mathbf{X}_2^0 , then we could define an alternative $\mathbf{X}'_2 = \mathbf{X}_2 - \mathbf{X}_2^0$ and $\mathbf{X}'_1 = \mathbf{X}_1 + \epsilon \mathbf{X}_2^0$. For \mathbf{X}'_2 and \mathbf{X}'_1 all relations hold, which we derived so far for \mathbf{X}_1 and \mathbf{X}_2 . Note that this special choice of \mathbf{X}_2 is possible since the expansion of $\mathbf{X} = \epsilon \mathbf{X}_1 + \epsilon^2 \mathbf{X}_2 + \dots$ is not unique.

C.1.2 Third order equation

The third order equation is of the form

$$\begin{aligned}
(\partial_{t_0} - \mathcal{L})X_3 &= -\partial_{t_1} \mathbf{X}_2 - \partial_{t_2} \mathbf{X}_1 \\
&+ \begin{pmatrix} 1 \\ 0 \end{pmatrix} (D_d 2\partial_{x_1} \partial_{x_0} \mathbf{X}_2 - K'_c (2\partial_{x_0} \partial_{x_1} X_{d,2} + 4\partial_{x_0}^3 \partial_{x_1} X_{d,2})) \\
&- K'_c \begin{pmatrix} 1 \\ 0 \end{pmatrix} \partial_{x_0} \mathcal{F}_1 (\partial_{x_0} X_{d,2} + \partial_{x_0}^3 X_{d,2}) \\
&- K'_c \begin{pmatrix} 1 \\ 0 \end{pmatrix} \partial_{x_0} \mathcal{F}_2 (\partial_{x_0} X_{d,1} + \partial_{x_0}^3 X_{d,1}) \\
&+ \begin{pmatrix} 1 \\ 0 \end{pmatrix} (D_d (2\partial_{x_0} \partial_{x_2} + \partial_{x_1}^2) X_{d,1} - K'_c (\partial_{x_1}^2 + 6\partial_{x_0}^2 \partial_{x_1}^2 + 2\partial_{x_0} \partial_{x_2} + 4\partial_{x_0}^3 \partial_{x_2}) X_{d,1} \\
&\quad - K'_2 (\partial_{x_0}^2 + \partial_{x_0}^4) X_{d,1} \\
&\quad - K'_c \partial_{x_1} \mathcal{F}_1 (\partial_{x_0} + \partial_{x_0}^3) X_{d,1} \\
&\quad - K'_c \partial_{x_0} \mathcal{F}_1 (\partial_{x_1} + 3\partial_{x_1} \partial_{x_0}^2) X_{d,1}),
\end{aligned}$$

where we have used that $K'_1 = 0$. The symbols $\mathcal{F}_1, \mathcal{F}_2$ denote the first and the second order part of the function \mathcal{F} , which was introduced in (3.7). The sum of terms, containing derivatives with respect to x_2 , vanishes, which can be seen by plugging in the value of k_c . All terms linear in \mathbf{X}_2 give no contribution to the solvability condition, since \mathbf{X}_2 contains only Fourier components of second or zeroth order. Also, this is true for the terms in the last two lines. The remaining terms which give a contribution to the solvability condition are

$$\begin{aligned}
(\partial_{t_0} - \mathcal{L})X_3 &= -\partial_{t_2}\mathbf{X}_1 \\
&\quad -K'_c \begin{pmatrix} 1 \\ 0 \end{pmatrix} \{ \partial_{x_0}\mathcal{F}_1(\partial_{x_0}X_{d,2} + \partial_{x_0}^3X_{d,2}) + \partial_{x_0}\mathcal{F}_2(\partial_{x_0}X_{d,1} + \partial_{x_0}^3X_{d,1}) \} \\
&\quad + \begin{pmatrix} 1 \\ 0 \end{pmatrix} \left(D_d(\partial_{x_1}^2)X_{d,1} - K'_c(\partial_{x_1}^2 + 6\partial_{x_0}^2\partial_{x_1}^2)X_{d,1} - K'_2(\partial_{x_0}^2 + \partial_{x_0}^4)X_{d,1} \right) + \dots \\
&= -\partial_{t_2}\mathbf{X}_1 \\
&\quad -K'_c \begin{pmatrix} 1 \\ 0 \end{pmatrix} \partial_{x_0}(\alpha X_{d,1} + \beta X_{de,1})(\partial_{x_0}X_{d,2} + \partial_{x_0}^3X_{d,2}) \\
&\quad -K'_c \begin{pmatrix} 1 \\ 0 \end{pmatrix} \partial_{x_0}(\alpha X_{d,2} + \beta X_{de,2} - \gamma X_{d,1}(X_{d,1} + X_{de,1}))(\partial_{x_0}X_{d,1} + \partial_{x_0}^3X_{d,1}) \\
&\quad + \begin{pmatrix} 1 \\ 0 \end{pmatrix} (4K'_c k_c^2 \partial_{x_1}^2 X_{d,1} - K'_2(k_c^4 - k_c^2)X_{d,1}) + \dots
\end{aligned}$$

The dots ... are a placeholder for terms which do not give a contribution to the solvability condition. The terms in the second and third line after the second equality sign give contributions to the prefactor of the terms $A_L|A_L|^2, A_L|A_R|^2, A_R|A_L|^2$ and $A_R|A_R|^2$ in the equation (3.2). To obtain the nonlinear parts of the equation for A_L , we are interested in those terms which contain the Fourier component $\exp(i(\omega_c t_0 + k_c x_0))$, and which are either proportional to $A_L|A_L|^2$ or $A_L|A_R|^2$. Lets say

$$\begin{aligned}
&-K'_c \partial_{x_0}(\alpha X_{d,1} + \beta X_{de,1})(\partial_{x_0}X_{d,2} + \partial_{x_0}^3X_{d,2}) =: \\
&\quad (a_{LL}A_L|A_L|^2 + a_{RL}A_L|A_R|^2) \exp i(\omega_c t_0 + k_c x_0) + \dots \\
&-K'_c \partial_{x_0}(\alpha X_{d,2} + \beta X_{de,2})(\partial_{x_0}X_{d,1} + \partial_{x_0}^3X_{d,1}) =: \\
&\quad (b_{LL}A_L|A_L|^2 + b_{RL}A_L|A_R|^2) \exp i(\omega_c t_0 + k_c x_0) + \dots \\
&-K'_c \partial_{x_0}(-\gamma X_{d,1}(X_{d,1} + X_{de,1}))(\partial_{x_0}X_{d,1} + \partial_{x_0}^3X_{d,1}) =: \\
&\quad (c_{LL}A_L|A_L|^2 + c_{RL}A_L|A_R|^2) \exp i(\omega_c t_0 + k_c x_0) + \dots,
\end{aligned}$$

where the dots ... are a placeholder for terms linear in A_L, A_R or with different Fourier components. The coefficients $a_{LL}, a_{RL}, b_{LL}, b_{RL}, c_{LL}, c_{RL}$ can be calculated in a straightforward but lengthy calculation. This can also be done with Mathematica, using the command

$$\begin{aligned}
Fourier11 &= \text{Coeff}[-K'_c \partial_{x_0}(\alpha X_{d,1} + \beta X_{de,1})(\partial_{x_0}X_{d,2} + \partial_{x_0}^3X_{d,2}), 1, 1]; \\
a_{LL} &= \text{Coefficient}[Fourier11, A_L A_L A_L^*]; \\
a_{RL} &= \text{Coefficient}[Fourier11, A_L A_R A_R^*];
\end{aligned}$$

The coefficients evaluate to

$$\begin{aligned}
a_{LL} &= 4k_c^4(1 - 5k_c^2 + 4k_c^4)K_c'^2 v_d |\alpha v_d + \beta v_{de}|^2 U_{2,2,d}, \\
a_{RL} &= 4k_c^4(1 - 5k_c^2 + 4k_c^4)K_c'^2 (\alpha v_d + \beta v_{de}) U_{0,2,d} (v_d(2\alpha v_d^* + \beta v_{de}^*) + \beta v_{de} v_d^*), \\
b_{LL} &= -2k_c^4(-1 + k_c^2)^2 K_c'^2 v_d (\alpha v_d + \beta v_{de}) (\alpha U_{2,2,d} + \beta U_{2,2,de}) v_d^*, \\
b_{RL} &= -2k_c^4(-1 + k_c^2)^2 K_c'^2 v_d (\alpha U_{0,2,d} + \beta U_{0,2,de}) (\beta v_{de} v_d^* + v_d(2\alpha v_d^* + \beta v_{de}^*)), \\
c_{LL} &= \gamma k_c^2(-1 + k_c^2) K_c' v_d^2 (v_d^* + v_{de}^*), \\
c_{RL} &= 2\gamma k_c^2(-1 + k_c^2) K_c' v_d (v_d + v_{de}) v_d^*.
\end{aligned}$$

Thus, we obtain as second solvability condition on A_L

$$\begin{aligned}
\partial_{t_2} A_L &= -\frac{\langle \underline{w}, (v_d, 0) \rangle}{\langle \underline{w}, \underline{v} \rangle} K_2'(k_c^4 - k_c^2) A_L + \frac{\langle \underline{w}, (v_d, 0) \rangle}{\langle \underline{w}, \underline{v} \rangle} 4K_c' k_c^2 \partial_{x_1}^2 A_L \\
&\quad + \frac{\langle \underline{w}, (1, 0) \rangle}{\langle \underline{w}, \underline{v} \rangle} (a_{LL} + b_{LL} + c_{LL}) A_L |A_L^2| \\
&\quad + \frac{\langle \underline{w}, (1, 0) \rangle}{\langle \underline{w}, \underline{v} \rangle} (a_{RL} + b_{RL} + c_{RL}) A_L |A_R^2| \\
&= -\frac{1}{2} \left(1 - \frac{i}{\omega_c}\right) K_2'(k_c^4 - k_c^2) A_L + 2 \left(1 - \frac{i}{\omega_c}\right) K_c' k_c^2 \partial_{x_1}^2 A_L \quad (C.3) \\
&\quad + \frac{1}{2i\omega_c} (a_{LL} + b_{LL} + c_{LL}) A_L |A_L^2| + \frac{1}{2i\omega_c} (a_{RL} + b_{RL} + c_{RL}) A_L |A_R^2|.
\end{aligned}$$

The same equations holds for $\partial_{t_2} A_R$, if we exchange A_R and A_L in the above equation. As first solvability condition, we had

$$\partial_{t_1} A_L = 0, \quad (C.4)$$

with the equivalent relation for A_R . Thus, multiplying equation (C.4) by ϵ^2 and (C.3) by ϵ^3 and adding the two relations, we obtain

$$\begin{aligned}
(\epsilon \partial_{t_1} + \epsilon^2 \partial_{t_2}) \epsilon A_L &= -\frac{1}{2} \left(1 - \frac{i}{\omega_c}\right) \epsilon^2 K_2'(k_c^4 - k_c^2) \epsilon A_L + 2 \left(1 - \frac{i}{\omega_c}\right) K_c' k_c^2 \epsilon^2 \partial_{x_1}^2 \epsilon A_L \\
&\quad + \frac{1}{2i\omega_c} (a_{LL} + b_{LL} + c_{LL}) \epsilon A_L \epsilon^2 |A_L^2| \\
&\quad + \frac{1}{2i\omega_c} (a_{RL} + b_{RL} + c_{RL}) \epsilon A_L \epsilon^2 |A_R^2| + \mathcal{O}(\epsilon^4).
\end{aligned}$$

Using expansions (3.8) and rescaling A_L such that $A_L \rightarrow \epsilon A_L$, we get

$$\begin{aligned}
\partial_t A_L &= -\frac{1}{2} \left(1 - \frac{i}{\omega_c}\right) \Delta K'(k_c^4 - k_c^2) A_L + 2 \left(1 - \frac{i}{\omega_c}\right) K_c' k_c^2 \partial_x^2 A_L \\
&\quad + \frac{1}{2i\omega_c} (a_{LL} + b_{LL} + c_{LL}) A_L |A_L^2| \\
&\quad + \frac{1}{2i\omega_c} (a_{RL} + b_{RL} + c_{RL}) A_L |A_R^2| + \mathcal{O}(\epsilon^4).
\end{aligned}$$

This is the amplitude equation for A_L . The respective equation holds for A_R exchanging A_R and A_L in the above equation. Rescaling of A_L, A_R , time and

space yields equations of the form of (3.2). The coefficient g_1 is then given by

$$g_1 = \frac{\operatorname{Re}\left(\frac{1}{2i\omega_c}(a_{RL} + b_{RL} + c_{RL})\right)}{\operatorname{Re}\left(\frac{1}{2i\omega_c}(a_{LL} + b_{LL} + c_{LL})\right)} = \frac{\operatorname{Im}(a_{RL} + b_{RL} + c_{RL})}{\operatorname{Im}(a_{LL} + b_{LL} + c_{LL})}. \quad (\text{C.5})$$

C.2 The case of $\bar{k}_1, \bar{k}_2 \neq 0$

Here, we derive the amplitude equations for the dynamical system given by Equations (3.6) for arbitrary choices of \bar{k}_1, \bar{k}_2 . To this end, we perform a perturbation calculation substituting the Expansions (3.8) into the Equation (3.15) which describes the time evolution of deflections from the homogeneous state.

The second order equation is here

$$\begin{aligned} (\partial_{t_0} - \mathcal{L})\mathbf{X}_2 &= -\partial_{t_1}\mathbf{X}_1 \\ &\quad -K'_c \begin{pmatrix} 1 \\ 0 \end{pmatrix} \delta(2\partial_{x_0}\partial_{x_1}X_{de,1} + \zeta 4\partial_{x_0}^3\partial_{x_1}X_{de,1}) \\ &\quad -K'_1 \begin{pmatrix} 1 \\ 0 \end{pmatrix} (\partial_{x_0}^2 X_{d,1} + \partial_{x_0}^4 X_{d,1} + \delta(\partial_{x_0}^2 X_{de,1} + \zeta \partial_{x_0}^4 X_{de,1})) \\ &\quad -K'_c \begin{pmatrix} 1 \\ 0 \end{pmatrix} \partial_{x_0}(\alpha X_{d,1} + \beta X_{de,1})(\partial_{x_0} X_{d,1} + \partial_{x_0}^3 X_{d,1} + \delta(\partial_{x_0} X_{de,1} + \zeta \partial_{x_0}^3 X_{de,1})). \end{aligned} \quad (\text{C.6})$$

The solvability condition of this equation yields

$$\begin{aligned} \partial_{t_1}A_L &= -K'_1 \frac{\langle \underline{w}, (1, 0) \rangle}{\langle \underline{w}, \underline{v} \rangle} ((k_c^4 - k_c^2)v_d + \delta(\zeta k_c^4 - k_c^2)v_{de})A_L \\ &\quad + K'_c \frac{\langle \underline{w}, (1, 0) \rangle}{\langle \underline{w}, \underline{v} \rangle} 2ik_c\delta(\zeta 2k_c^2 - 1)v_{de}\partial_{x_1}A_L. \end{aligned} \quad (\text{C.7})$$

To avoid the exponential growth, or decay of A_L , K'_1 has to be zero again. The remaining part evaluates to

$$\partial_{t_1}A_L = K'_c \frac{k_c}{\omega_c} \delta(\zeta 2k_c^2 - 1)w_E \partial_{x_1}A_L, \quad (\text{C.8})$$

where we have used that

$$\frac{\langle \underline{w}, (1, 0) \rangle}{\langle \underline{w}, \underline{v} \rangle} = \frac{\langle \underline{w}, 1/(2i\omega_c)(\underline{v} - \underline{v}^*) \rangle}{\langle \underline{w}, \underline{v} \rangle} = \frac{\langle \underline{w}, \underline{v} \rangle}{2i\omega_c \langle \underline{w}, \underline{v} \rangle} = \frac{1}{2i\omega_c}.$$

Thus the group velocity is $s_0 = K'_c \frac{k_c}{\omega_c} \delta(\zeta 2k_c^2 - 1)w_E$. The analogous equation to (C.8) for A_R yields $\partial_{t_1}A_R = -s_0 \partial_{x_1}A_R$. The form of \mathbf{X}_2 is thus

$$\begin{aligned} \mathbf{X}_2 &= -\frac{K'_c \delta w_E}{2\omega_c^2} \underline{v}^* (2\zeta k_c^2 - 1) \partial_{x_0} \partial_{x_1} (A_L e^{i(\omega_c t + k_c x)} + A_R e^{i(\omega_c t - k_c x)}) + \text{c.c.} \\ &\quad + C_{2,2} \mathbf{U}_{2,2} \exp 2i(\omega_c t + k_c x) + C_{2,-2} \mathbf{U}_{2,-2} \exp 2i(\omega_c t - k_c x) \\ &\quad + C_{-2,2} \mathbf{U}_{-2,2} \exp -2i(\omega_c t - k_c x) + C_{-2,-2} \mathbf{U}_{-2,-2} \exp -2i(\omega_c t + k_c x) \\ &\quad + C_{0,2} \mathbf{U}_{0,2} \exp -2ik_c x + C_{0,-2} \mathbf{U}_{0,-2} \exp -2ik_c x, \end{aligned}$$

where

$$\begin{aligned}
C_{2,2} &= -2A_L^2 k_c^2 ((k_c^2 - 1)v_d + \delta(\zeta k_c^2 - 1)v_{de}) K'_c (\alpha v_d + \beta v_{de}) \\
C_{2,-2} &= -2A_R^2 k_c^2 ((k_c^2 - 1)v_d + \delta(\zeta k_c^2 - 1)v_{de}) K'_c (\alpha v_d + \beta v_{de}) \\
C_{-2,2} &= C_{2,-2}^*, \quad C_{-2,-2} = C_{2,2}^* \\
C_{0,2} &= -2A_R k_c^2 K'_c A_L^* ((k_c^2 - 1)(\beta(v_{de}v_d^* + v_d v_{de}^*) + 2\alpha v_d v_d^*) \\
&\quad + \delta(\zeta k_c^2 - 1)(\beta 2v_{de}v_{de}^* + \alpha(v_{de}v_d^* + v_d v_{de}^*))) \\
C_{0,-2} &= -2A_L k_c^2 K'_c A_R^* ((k_c^2 - 1)(\beta(v_{de}v_d^* + v_d v_{de}^*) + 2\alpha v_d v_d^*) \\
&\quad + \delta(\zeta k_c^2 - 1)(\beta 2v_{de}v_{de}^* + \alpha(v_{de}v_d^* + v_d v_{de}^*))).
\end{aligned}$$

Note, that the first order Fourier contributions to \mathbf{X}_2 do not affect the value of the coefficients of the nonlinear terms in the amplitude equation. Lets consider the third order equation: Since we are only interested in the nonlinear terms of the amplitude equation, we need to take into account only terms cubic in the \mathbf{X}_i .

$$\begin{aligned}
(\partial_{t_0} - \mathcal{L})X_3 &= \text{linear and quadratic expressions in } \mathbf{X}_i \\
&\quad - K'_c \begin{pmatrix} 1 \\ 0 \end{pmatrix} \partial_{x_0} \mathcal{F}_1 (\partial_{x_0} X_{d,2} + \partial_{x_0}^3 X_{d,2}) \\
&\quad - K'_c \begin{pmatrix} 1 \\ 0 \end{pmatrix} \partial_{x_0} \mathcal{F}_2 (\partial_{x_0} X_{d,1} + \partial_{x_0}^3 X_{d,1}).
\end{aligned}$$

Similar to the above section, we define the coefficients $a_{LL}, a_{RL}, b_{LL}, b_{RL}, c_{LL}, c_{RL}$ by

$$\begin{aligned}
&-K'_c \partial_{x_0} (\alpha X_{d,1} + \beta X_{de,1}) (\partial_{x_0} X_{d,2} + \partial_{x_0}^3 X_{d,2} + \delta(\partial_{x_0} X_{de,2} + \zeta \partial_{x_0}^3 X_{de,2})) \\
&\quad =: (a_{LL} A_L |A_L|^2 + a_{RL} A_L |A_R|^2) \exp i(\omega_c t_0 + k_c x_0) + \dots \\
&-K'_c \partial_{x_0} (\alpha X_{d,2} + \beta X_{de,2}) (\partial_{x_0} X_{d,1} + \partial_{x_0}^3 X_{d,1} + \delta(\partial_{x_0} X_{de,2} + \zeta \partial_{x_0}^3 X_{de,2})) \\
&\quad =: (b_{LL} A_L |A_L|^2 + b_{RL} A_L |A_R|^2) \exp i(\omega_c t_0 + k_c x_0) + \dots \\
&-K'_c \partial_{x_0} (-\gamma X_{d,1} (X_{d,1} + X_{de,1})) (\partial_{x_0} X_{d,1} + \partial_{x_0}^3 X_{d,1} + \delta(\partial_{x_0} X_{de,2} + \zeta \partial_{x_0}^3 X_{de,2})) \\
&\quad =: (c_{LL} A_L |A_L|^2 + c_{RL} A_L |A_R|^2) \exp i(\omega_c t_0 + k_c x_0) + \dots,
\end{aligned}$$

where dots \dots are a placeholder for linear terms in A_L, A_R or terms with different Fourier components. An easy but lengthy calculation yields then

$$\begin{aligned}
a_{LL} &= 4k_c^4 K_c'^2 ((k_c^2 - 1)v_d + \delta(\zeta k_c^2 - 1)v_{de}) \\
&\quad (U_{2,2,d}(4k_c^2 - 1) + U_{2,2,de}\delta(4\zeta k_c^2 - 1)) |\alpha v_d + \beta v_{de}|^2, \\
a_{RL} &= 4k_c^4 K_c'^2 (\alpha v_d + \beta v_{de}) (U_{0,2,d}(4k_c^2 - 1) + U_{0,2,de}\delta(4\zeta k_c^2 - 1)) \\
&\quad ((k_c^2 - 1)(\beta(v_{de}v_d^* + v_d v_{de}^*) + 2\alpha v_d v_d^*) + \delta(\zeta k_c^2 - 1)(\beta 2v_{de}v_{de}^* + \alpha(v_{de}v_d^* + v_d v_{de}^*))), \\
b_{LL} &= -2k_c^4 K_c'^2 (\alpha v_d + \beta v_{de}) (v_d(k_c^2 - 1) + v_{de}\delta(\zeta k_c^2 - 1)) (\alpha U_{2,2,d} + \beta U_{2,2,de}) \\
&\quad (v_d^*(k_c^2 - 1) + v_{de}^*\delta(\zeta k_c^2 - 1)), \\
b_{RL} &= -2k_c^4 K_c'^2 (v_d(k_c^2 - 1) + v_{de}\delta(\zeta k_c^2 - 1)) (\alpha U_{0,2,d} + \beta U_{0,2,de}) \\
&\quad ((k_c^2 - 1)(\beta(v_{de}v_d^* + v_d v_{de}^*) + 2\alpha v_d v_d^*) + \delta(\zeta k_c^2 - 1)(\beta 2v_{de}v_{de}^* + \alpha(v_{de}v_d^* + v_d v_{de}^*))), \\
c_{LL} &= \gamma k_c^2 K_c' (v_d^*(v_d^* + v_{de}^*)(k_c^2 - 1) + (2v_d v_{de} v_d^* + v_{de}^2 v_d^* - v_d^2 v_{de}^*) \delta(\zeta k_c^2 - 1)), \\
c_{RL} &= 2\gamma k_c^2 K_c' v_d (v_d + v_{de}) (v_d^*(k_c^2 - 1) + v_{de}^* \delta(\zeta k_c^2 - 1)).
\end{aligned} \tag{C.9}$$

For the value of g_1 again equation (C.5) holds. This follows in an analogous way as in the preceding section.

Appendix D

Particle-based version of the aggregation current model

For the computational analysis of the stochastic switching of short “newborn” *E. coli* cells (see Section 6.1), we used a particle-based version of the aggregation current model introduced in Section 2.3.2. This stochastic particle-based description has been derived as part of the PhD thesis of G. Meacci [75] and a short summary will be given here for completeness. The model incorporates mutual interactions of membrane-bound MinD proteins thereby inducing aggregation of MinD on the membrane. Furthermore, it takes into account the exchange of MinD and MinE between the membrane and the cytoplasm, where MinE only binds to membrane-bound MinD and where MinD detaches from the membrane only in the presence of MinE. We consider the limit of large cytoplasmic diffusion which effectively leads to homogeneous cytoplasmic concentrations. Measurements of the cytoplasmic diffusion constants of MinD and MinE yielded values larger than $10\mu\text{m}^2/\text{s}$ [46] and support this assumption.

The description considers a one-dimensional lattice with N sites. The lattice spacing l_b is chosen such that it is much larger than the protein size and much smaller than the characteristic length of the Min pattern. Each site can contain at most n_{max} proteins. We assume diffusional mixing such that proteins are indistinguishable on a site. For site j , the probability of attachment of cytoplasmic MinD and MinE during a sufficiently small time step Δt is given by

$$P_{D \rightarrow d} = \Delta t \omega_D \left(\frac{N_D}{N} \right) \left(1 - \frac{n_{d,j} + n_{de,j}}{n_{\text{max}}} \right) \quad (\text{D.1})$$

$$P_{E \rightarrow de} = \Delta t \omega_E \left(\frac{N_E}{N} \right) \frac{n_{d,j}}{n_{\text{max}}} \quad , \quad (\text{D.2})$$

respectively. Here, ω_D, ω_E are the corresponding attachment rates and N_D and N_E are, respectively, the numbers of cytoplasmic MinD and MinE. The numbers of membrane-bound MinD and MinDE complexes on site j are $n_{d,j}$ and $n_{de,j}$. The detachment probability is

$$P_{de \rightarrow E+D} = \Delta t \omega_{de} n_{de,j} \quad , \quad (\text{D.3})$$

where ω_{de} is the detachment rate. The exchange of particles between sites is governed by

$$P_{j \rightarrow j\pm 1} = \frac{D_d \Delta t}{l_b^2} n_{d,j} \left(1 - \frac{n_{d,j\pm 1} - n_{de,j\pm 1}}{n_{\text{max}}} \right) I_{j \rightarrow j\pm 1} \quad , \quad (\text{D.4})$$

where

$$I_{j \rightarrow j\pm 1} = \begin{cases} 1 & \text{if } \Delta E_j < 0 \\ \exp\left(-\frac{\Delta E_j}{k_B T}\right) & \text{if } \Delta E_j > 0 \end{cases} \quad (\text{D.5})$$

with $\Delta E_j = V_{j\pm 1} - V_j$. The potential V describes the interaction strength between Min-proteins on the membrane. We assume a square hole potential

$$V_j = - \left[\frac{g_d}{(2R_d + 1)n_{\max}} \sum_{j=-R_d}^{R_d} n_{d,j} - \frac{g_{de}}{(2R_{de} + 1)n_{\max}} \sum_{j=-R_{de}}^{R_{de}} n_{de,j} \right]. \quad (\text{D.6})$$

Here, the integers R_d and R_{de} relate to the ranges r_d of the MinD-MinD interaction and r_{de} of the MinD-MinDE interaction through $R_d \simeq r_d/l_b$ and $R_{de} \simeq r_{de}/l_b$. The parameters g_d and g_{de} tune the interaction strength. The diffusion constant of membrane-bound MinD is D_d .

Appendix E

Glossary

Mitotic spindle	A cytoskeletal structure formed by microtubules prior to division in eukaryotic cells. The mitotic spindle separates the sister chromatids of the chromosomes and pulls them to opposite sides of the cell. For further reading see [78].
Contractile ring	A cytoskeletal structure which forms during the process of cell division in eukaryotic as well as in prokaryotic cells. This ring forms typically in the equatorial plane of the cell beneath the cytoplasmic membrane and is constituted from polymerized proteins. To accomplish cell division, the ring constricts and shrinks in radius.
DIC	Differential interference contrast microscopy (DIC) is an optical microscopy illumination technique using transmitted light. It enhances the contrast in unstained, transparent samples.
Micrograph	An image taken with a microscope.
Kymograph	An image that shows the time evolution of light intensity along a fixed line in the image of a sample. It can be obtained from a time series of micrographs.
Yeast two hybrid system	A technique from molecular biology which can be used to discover protein-protein interactions. The two proteins under study are expressed in yeast cells fused to either of two parts of a transcription factor. These parts are called the binding and the activating domain. The protein fused to the binding domain of the transcription factor is called the bait protein, while the protein fused to the activating domain is called the prey protein. If now the binding domain locates to the transcription site of the respective gene, interactions of bait and prey proteins enhance the probability that the activating domain is in close proximity and thus that transcription can start. The transcription level of the gene gives then information about the interaction level of bait and prey protein.

ATP	Adenosine triphosphate (ATP) is an energy-rich organic compound that serves as chemical fuel in cells. Hydrolysis of ATP releases energy.
Hydrolysis of ATP	Decomposition of ATP into Adenosine diphosphate and a hydrated inorganic phosphate.
ATPγS	A non-hydrolyzable ATP analog.
ATPase	An enzyme that catalyzes ATP hydrolysis.
Mini cells	Small cells void of DNA which can form in <i>E. coli</i> by division at the cell poles if the Min system is defective.
TIRF	Total internal reflection fluorescence microscopy. Microscopy technique used to observe structures in thin layers of a sample adjacent to the glass-water interface between cover slip and specimen.

Bibliography

- [1] W. B. Whitman, D. C. Coleman, and W. J. Wiebe. Prokaryotes: the unseen majority. *Proc Natl Acad Sci*, 95(12):6578–83, June 1998.
- [2] C. L. Sears. A dynamic partnership: Celebrating our gut flora. *Anaerobe*, 11(5):247–251, October 2005.
- [3] M. T. Madigan, J. Martinko, and J. Parker. *Brock Biology of Microorganisms*. Benjamin-Cummings Publishing Company, Subs of Addison Wesley Longman, Inc, 10th edition, May 2002.
- [4] J. Pogliano. The bacterial cytoskeleton. *Curr Opin Cell Bio*, 20(1):19–27, February 2008.
- [5] A. M. Zhabotinsky and A. N. Zaikin. Autowave processes in a distributed chemical system. *J Theor Biol*, 40(1):45–61, July 1973.
- [6] D. Dormann and C. J. Weijer. Imaging of cell migration. *EMBO J*, 25(15):3480–3493, August 2006.
- [7] F. J. Nédélec, T. Surrey, A. C. Maggs, and S. Leibler. Self-organization of microtubules and motors. *Nature*, 389:305, 1997.
- [8] G. Nicolis and I. Prigogine. *Self-organization in Nonequilibrium Systems: From Dissipative Structures to Order through Fluctuations*. John Wiley and Sons, 1977.
- [9] A. M. Turing. The chemical basis of morphogenesis. *Phil Trans Roy Soc (Lond.)*, 237:37, 1952.
- [10] M. C. Cross and P. C. Hohenberg. Pattern formation outside of equilibrium. *Rev Mod Phys*, 65:851–1112, 1993.
- [11] F. Nédélec, T. Surrey, and A. C. Maggs. Dynamic concentration of motors in microtubule arrays. *Phys Rev Lett*, 86:3192, 2001.
- [12] M. Loose, E. Fischer-Friedrich, J. Ries, K. Kruse, and P. Schwill. Spatial regulators for bacterial cell division self-organize into surface waves in vitro. *Science*, 320:789–92, 2008.
- [13] G. Meacci and K. Kruse. Min-oscillations in *Escherichia coli* induced by interactions of membrane-bound proteins. *Phys Biol*, 2:89–97, 2005.
- [14] H. C. Berg. *E. coli in Motion*. Springer, 1st edition, 2003.

- [15] X. C. Yu and W. Margolin. FtsZ ring clusters in min and partition mutants: role of both the Min system and the nucleoid in regulating FtsZ ring localization. *Mol Microbiol*, 32(2):315–26, 1999.
- [16] L. J. Wu and J. Errington. Coordination of cell division and chromosome segregation by a nucleoid occlusion protein in *Bacillus subtilis*. *Cell*, 117:915–25, 2004.
- [17] J. Lutkenhaus. Assembly dynamics of the bacterial MinCDE system and spatial regulation of the Z ring. *Annu Rev Biochem*, 76:539–62, 2007.
- [18] Lutkenhaus J. Dynamic proteins in bacteria. *Curr Opin Microbiol*, 5:548–52, 2002.
- [19] Z. Hu and J. Lutkenhaus. Topological regulation of cell division in *Escherichia coli* involves rapid pole to pole oscillation of the division inhibitor MinC under the control of MinD and MinE. *Mol Microbiol*, 34:82–90, 1999.
- [20] D. M. Raskin and P. A. de Boer. Rapid pole-to-pole oscillation of a protein required for directing division to the middle of *Escherichia coli*. *Proc Natl Acad Sci USA*, 96:4971–6, 1999.
- [21] D. M. Raskin and P. A. de Boer. The MinE ring: an FtsZ-independent cell structure required for selection of the correct division site in *E. coli*. *Cell*, 91:685–94, 1997.
- [22] C. A. Hale, H. Meinhardt, and P. A. de Boer. Dynamic localization cycle of the cell division regulator MinE in *Escherichia coli*. *EMBO J*, 20:1563–72, 2001.
- [23] D. M. Raskin and P. A. de Boer. MinDE-dependent pole-to-pole oscillation of division inhibitor minC in *Escherichia coli*. *J. Bacteriol.*, 181:6419–24, 1999.
- [24] Z. L. Hu, E. P. Gogol, and J. Lutkenhaus. Dynamic assembly of MinD on phospholipid vesicles regulated by ATP and MinE. *Proc Natl Acad Sci USA*, 99:6761–6, 2002.
- [25] K. Suefuji, R. Valluzzi, and D. RayChaudhuri. Dynamic assembly of Mind into filament bundles modulated by Atp, phospholipids, and Mine. *Proc Natl Acad Sci USA*, 99(26):16776–81, 2002.
- [26] A. Taghbalout, L. Ma, and L. Rothfield. Role of MinD-membrane association in Min protein interactions. *J Bacteriol.*, 188:735–799, 2006.
- [27] L. L. Lackner, D.M. Raskin, and P.A. de Boer. ATP-dependent interactions between *Escherichia coli* Min proteins and the phospholipid membrane in vitro. *J Bacteriol*, 185(3):735–49, 2003.
- [28] E. Mileykovskaya, I. Fishov, X. Fu, B.D. Corbin, W. Margolin, and W. Dowhan. Effects of phospholipid composition on MinD-membrane interactions in vitro and in vivo. *J Biol Chem*, 278(25):22193–8, 2003.

-
- [29] Y. L. Shih, X. Fu, G. F. King, T. Le, and L. Rothfield. Division site placement in *E. coli*: mutations that prevent formation of the MinE ring lead to loss of the normal midcell arrest of growth of polar MinD membrane domains. *EMBO J*, 21(13):3347–57, 2002.
- [30] Y. L. Shih, T. Le, and L. Rothfield. Division site selection in *Escherichia coli* involves dynamic redistribution of Min proteins within coiled structures that extend between the two cell poles. *Proc Natl Acad Sci USA*, 100:7865–70, 2003.
- [31] K. Kruse, M. Howard, and W. Margolin. An experimentalist’s guide to computational modelling of the min system. *Mol Microbiol*, 63:1279–84, 2007.
- [32] H. Meinhardt and P. A. de Boer. Pattern formation in *Escherichia coli*: a model for the pole-to-pole oscillations of Min proteins and the localization of the division site. *Proc Natl Acad Sci USA*, 98:14202–7, 2001.
- [33] J. Howard. *Mechanics of motor proteins and the cytoskeleton*. Sinauer Associates, Sunderland, 2001.
- [34] K. Kruse. A dynamic model for determining the middle of *Escherichia coli*. *Biophys J*, 82(2):618–27, February 2002.
- [35] K. C. Huang, Y. Meir, and N. S. Wingreen. Dynamic structures in *Escherichia coli*: spontaneous formation of MinE rings and MinD polar zones. *Proc Natl Acad Sci USA*, 100:12724–8, 2003.
- [36] D. A. Drew, M. J. Osborn, and L. I. Rothfield. A polymerization-depolymerization model that accurately generates the self-sustained oscillatory system involved in bacterial division site placement. *Proc Natl Acad Sci U S A*, 102(17):6114–8, 2005.
- [37] E. Fischer-Friedrich, R. Nguyen, and K. Kruse. Surface waves of min-proteins. *Phys Biol*, 4:38–47, 2007.
- [38] R. A. Kerr, H. Levine, T. J. Sejnowski, and W. J. Rappel. Division accuracy in a stochastic model of Min oscillations in *Escherichia coli*. *Proc Natl Acad Sci U S A*, 103(2):347–52, 2006.
- [39] F. Tostevin and M. Howard. A stochastic model of Min oscillations in *Escherichia coli* and Min protein segregation during cell division. *Phys Biol*, 3(1):1–12, 2006.
- [40] N. Pavin, H. C. Paljetak, and V. Krstic. Min-protein oscillations in *Escherichia coli* with spontaneous formation of two-stranded filaments in a three-dimensional stochastic reaction-diffusion model. *Phys Rev E Stat Nonlin Soft Matter Phys*, 73(2 Pt 1):021904, 2006.
- [41] D. Fange and J. Elf. Noise-induced Min phenotypes in *E. coli*. *PLoS Comput Biol*, 2(6):e80, 2006.

- [42] M. Howard, A. D. Rutenberg, and S. de Vet. Dynamic compartmentalization of bacteria: accurate division in *E. coli*. *Phys Rev Lett*, 87:278102, 2001.
- [43] M. Howard and A. D. Rutenberg. Pattern formation inside bacteria: fluctuations due to the low copy number of proteins. *Phys Rev Lett*, 90:128102, 2003.
- [44] J. E. Hilliard and J. W. Cahn. Free energy of a nonuniform system.1.interfacial energy. *J Chem Phys*, 28(2):258–67, 1958.
- [45] H. J. Zhou, R. Schulze, S. Cox, C. Saez, Z. Hu, and J. Lutkenhaus. Analysis of MinD mutations reveals residues required for MinE stimulation of the MinD ATPase and residues required for MinC interaction. *J Bacteriol*, 187:629–38, 2005.
- [46] G. Meacci, J. Ries, E. Fischer-Friedrich, N. Kahya, P. Schwille, and K. Kruse. Mobility of Min-proteins in *Escherichia coli* measured by fluorescence correlation spectroscopy. *Phys Biol*, 3:255–63, 2006.
- [47] A. Mikhailov and G. Ertl. Pattern formation by adsorbates with attractive lateral interactions. *Chem Phys Lett*, 238(1-3):104–9, 1995.
- [48] M. Hildebrand and A. S. Mikhailov. Mesoscopic modeling in the kinetic theory of adsorbates. *J Phys Chem*, 100(49):19089–101, 1996.
- [49] K. C. Huang and N. S. Wingreen. Min-protein oscillations in round bacteria. *Phys Biol*, 1:229–35, 2004.
- [50] M. Hildebrand and A. S. Mikhailov. Traveling nanoscale structures in reactive adsorbates with attractive lateral interactions. *Phys Rev Lett*, 81:2602–2605, 1998.
- [51] C. Sachs, M. Hildebrand, S. Volkening, J. Wintterlin, and G. Ertl. Spatiotemporal self-organization in a surface reaction: from the atomic to the mesoscopic scale. *Science*, 293(5535):1635–8, 2001.
- [52] Z. Gitai, N. A. Dye, A. Reisenauer, M. Wachi, and L. Shapiro. MreB actin-mediated segregation of a specific region of a bacterial chromosome. *Cell*, 120(3):329–341, February 2005.
- [53] N. Iwai, K. Nagai, and M. Wachi. Novel s-benzylisothiurea compound that induces spherical cells in *Escherichia coli* probably by acting on a rod-shape-determining protein(s) other than penicillin-binding protein 2. *Bioscience, Biotechnology, and Biochemistry*, 66(12):2658–62, December 2002.
- [54] D. Scheffers, L. J. F. Jones, and J. Errington. Several distinct localization patterns for penicillin-binding proteins in *Bacillus subtilis*. *Molecular Microbiology*, 51(3):749–64, February 2004.
- [55] R. M. Figge, A. V. Divakaruni, and J. W. Gober. MreB, the cell shape-determining bacterial actin homologue, co-ordinates cell wall morphogenesis in *Caulobacter crescentus*. *Molecular Microbiology*, 51(5):1321–32, March 2004.

-
- [56] Z. Hu and J. Lutkenhaus. A conserved sequence at the C-terminus of MinD is required for binding to the membrane and targeting MinC to the septum. *Mol Microbiol*, 47(2):345–55, 2003.
- [57] W. van Saarloos. Front propagation into unstable states. *Phys Rep*, 386(2-6):29,222, 2003.
- [58] D. Walgraef. *Spatio-temporal pattern formation*. Springer, New York, 1997.
- [59] R. Hoyle. *Pattern formation*. Cambridge University Press, Cambridge, 2006.
- [60] E. Nicola. *Interfaces between Competing Patterns in Reaction-diffusion Systems with Nonlocal Coupling*. PhD thesis, Max-Planck-Institut für Physik komplexer Systeme Dresden, Dresden, 2001. <http://hsss.slub-dresden.de>.
- [61] M. Howard and K. Kruse. Cellular organization by self-organization: mechanisms and models for Min protein dynamics. *J. Cell Biol.*, 168:533–6, 2005.
- [62] J. Deich, E. M. Judd, H. H. McAdams, and W. E. Moerner. Visualization of the movement of single histidine kinase molecules in live *Caulobacter* cells. *Proc Natl Acad Sci U S A*, 101(45):15921–6, 2004.
- [63] M. B. Elowitz, M. G. Surette, P. E. Wolf, J. B. Stock, and S. Leibler. Protein mobility in the cytoplasm of *Escherichia coli*. *J. Bacteriol.*, 181(1):197–203, 1999.
- [64] O. Krichevsky and G. Bonnet. Fluorescence correlation spectroscopy: the technique and its applications. *Rep Prog Phys*, 65:251–297, 2002.
- [65] P. Cluzel, M. Surette, and S. Leibler. An ultrasensitive bacterial motor revealed by monitoring signaling proteins in single cells. *Science*, 287(5458):1652–5, 2000.
- [66] T.T. Le, S. Harlepp, C.C. Guet, K. Dittmar, T. Emonet, T. Pan, and P. Cluzel. Real-time RNA profiling within a single bacterium. *Proc Natl Acad Sci U S A*, 102(26):9160–4, 2005.
- [67] T. T. Le, T. Emonet, S. Harlepp, C. C. Guet, and P. Cluzel. Dynamical determinants of drug-inducible gene expression in a single bacterium. *Biophys J*, 90(9):3315–21, 2006.
- [68] B. D. Corbin, X. C. Yu, and W. Margolin. Exploring intracellular space: function of the Min system in round-shaped *Escherichia coli*. *EMBO J*, 21:1998, 2002.
- [69] A. Gennerich and D. Schild. Fluorescence correlation spectroscopy in small cytosolic compartments depends critically on the diffusion model used. *Biophys J*, 79(6):3294–306, 2000.
- [70] D. Magde, E. L. Elson, and W. W. Webb. Fluorescence correlation spectroscopy. II. An experimental realization. *Biopolymers*, 13(1):29–61, 1974.

- [71] P. Schwille, J. Korlach, and W. W. Webb. Fluorescence correlation spectroscopy with single-molecule sensitivity on cell and model membranes. *Cytometry*, 36(3):176–82, 1999.
- [72] A. Clauset, C. R. Shalizi, and M. E. J. Newman. Power-law distributions in empirical data. 2007. <http://arxiv.org/abs/0706.1062>.
- [73] M. Fritzsche. Dynamics of the Min system in modified geometries. Master's thesis, Saarland University, Saarbrücken, 2008.
- [74] L. Lackner. *Investigating the Mechanism of Escherichia coli Min Protein Dynamics*. PhD thesis, Case Western Reserve University, 2005. [http://www.ohiolink.edu/etd/view.cgi?acc_num\\$=case1124832205](http://www.ohiolink.edu/etd/view.cgi?acc_num$=case1124832205).
- [75] G. Meacci. *Physical aspects of Min oscillations in Escherichia coli*. PhD thesis, Max Planck Institute for the Physics of Complex Systems, Dresden, 2006. <http://nbn-resolving.de/urn:nbn:de:swb:14-1169728830839-77682>.
- [76] Y. Tu and G. Grinstein. How white noise generates power-law switching in bacterial flagellar motors. *Phys Rev Lett*, 94(20):208101, May 2005.
- [77] C. M. Bender and S. A. Orszag. *Advanced mathematical methods for scientists and engineers*. McGraw-Hill, 1978.
- [78] B. Alberts, A. Johnson, J. Lewis, M. Raff, K. Roberts, and P. Walter. *Molecular Biology of the Cell*. Garland, New York, 4 edition, 2002.

Eidesstattliche Versicherung

Hiermit versichere ich an Eides statt, dass ich die vorliegende Arbeit selbstständig und ohne Benutzung anderer als der angegebenen Hilfsmittel angefertigt habe. Die aus anderen Quellen oder indirekt übernommenen Daten und Konzepte sind unter Angabe der Quelle gekennzeichnet. Die Arbeit wurde bisher weder im In- noch im Ausland in gleicher oder ähnlicher Form in einem Verfahren zur Erlangung eines akademischen Grades vorgelegt.

Dresden, Dezember 2008

Elisabeth Fischer-Friedrich